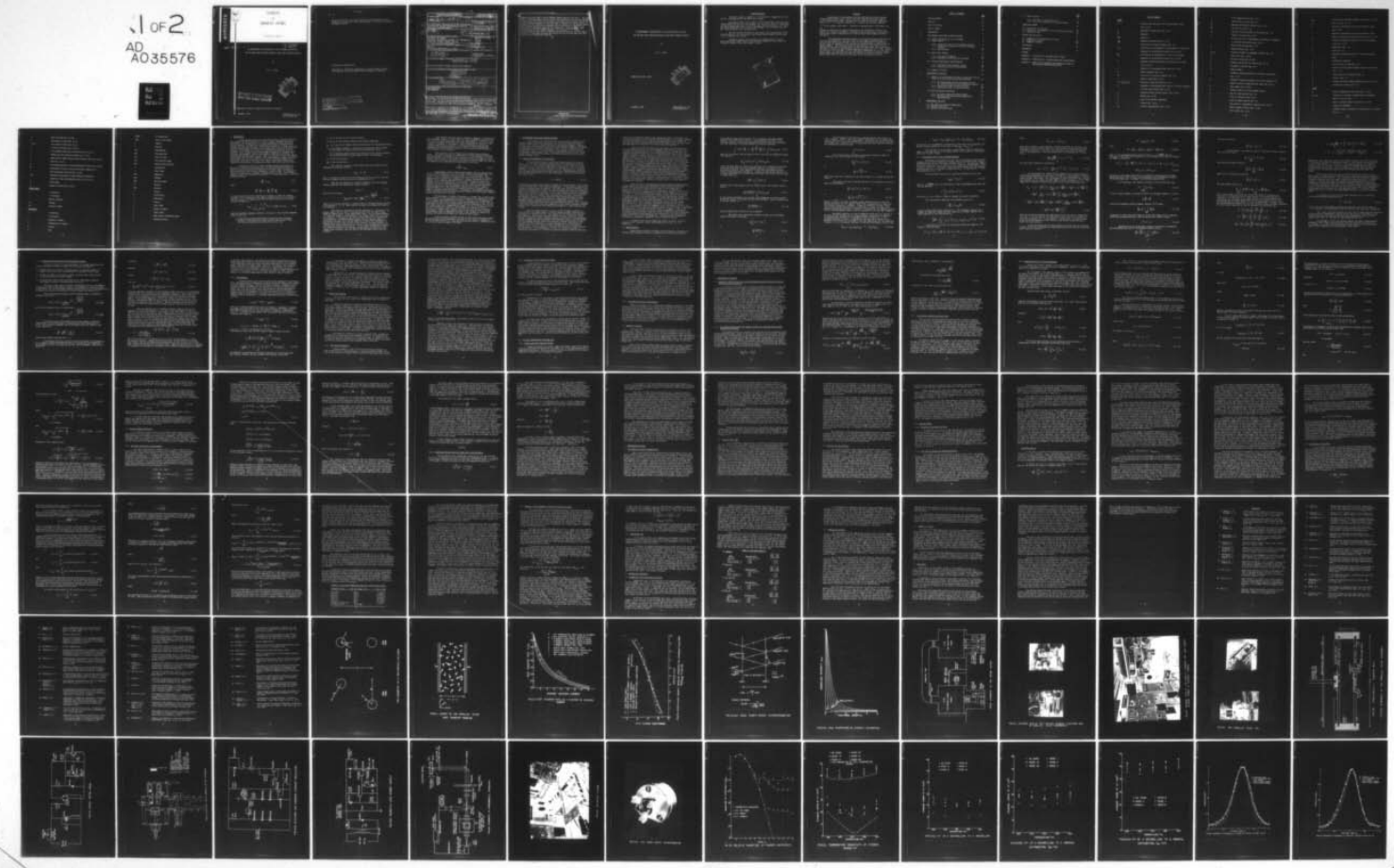
AD-A035 576 TORONTO UNIV (ONTARIO) INST FOR AEROSPACE STUDIES F/G 20/13
AN EXPERIMENTAL INVESTIGATION OF THE DISTRIBUTION FUNCTION FOR --ETC(U)
DEC 76 D T TONG AF-AFOSR-2091-71
UNCLASSIFIED UTIAS-210 AFOSR-TR-77-0060 NL

1 OF 2
AD
A035576



AD A035576

INSTITUTE
FOR
AEROSPACE STUDIES

UNIVERSITY OF TORONTO

AFOSR - TR - 77 - 0060

AN EXPERIMENTAL INVESTIGATION OF THE DISTRIBUTION FUNCTION FOR THE NEAR FREE MOLECULAR PARALLEL PLATE HEAT TRANSFER PROBLEM

by

D. T. L. Tong

DDC
FEB 14 1977
B

COPY AVAILABLE TO DDC DOES NOT
PERMIT FULLY LEGIBLE PRODUCTION

"Approved for public release; distribution unlimited."

December, 1976

UTIAS Report No. 210
CN ISSN 0082-5255

Qualified requestors may obtain additional copies from the Defense Documentation Center, all others should apply to the National Technical Information Service.

Conditions of Reproduction:

Reproduction, translation, publication, use and disposal in whole or in part by or for the United States Government is permitted.

AIR FORCE OFFICE OF SCIENTIFIC RESEARCH (AFSC)
NOTICE OF TRANSMITTAL TO DDC
This technical report has been reviewed and is approved for public release IAW AFR 190-12 (7b).
Distribution is unlimited.
A. D. BLOSE
Technical Information Officer

SECURITY CLASSIFICATION OF THIS PAGE (When Data Entered)

REPORT DOCUMENTATION PAGE

READ INSTRUCTIONS BEFORE COMPLETING FORM

1. REPORT NUMBER: AFOSR - TR - 77 - 0060
2. GOVT ACCESSION NO.
3. RECIPIENT'S CATALOG NUMBER

4. TITLE (and Subtitle): AN EXPERIMENTAL INVESTIGATION OF THE DISTRIBUTION FUNCTION FOR THE NEAR FREE MOLECULAR PARALLEL PLATE HEAT TRANSFER PROBLEM

5. TYPE OF REPORT & PERIOD COVERED: INTERIM report

6. PERFORMING ORG. REPORT NUMBER: UTIAS Report No 210

7. AUTHOR(s): D. T. L. TONG

8. CONTRACT OR GRANT NUMBER(s): AF-AFOSR-2091-71

9. PERFORMING ORGANIZATION NAME AND ADDRESS
UNIVERSITY OF TORONTO
INSTITUTE FOR AEROSPACE STUDIES, 4925 DUFFERIN ST
DOWNSVIEW, ONTARIO, CANADA, M3H 5T6

10. PROGRAM ELEMENT, PROJECT, TASK AREA & WORK UNIT NUMBERS
681307
9783-06
61102F

11. CONTROLLING OFFICE NAME AND ADDRESS
AIR FORCE OFFICE OF SCIENTIFIC RESEARCH /NA
BLDG 410
BOLLING AIR FORCE BASE, D C 20332

12. REPORT DATE: Dec 76

13. NUMBER OF PAGES: 116

14. MONITORING AGENCY NAME & ADDRESS (if different from Controlling Office): 118p.

15. SECURITY CLASS. (of this report): UNCLASSIFIED

15a. DECLASSIFICATION/DOWNGRADING SCHEDULE

16. DISTRIBUTION STATEMENT (of this Report): UTIAS-210

Approved for public release; distribution unlimited.

17. DISTRIBUTION STATEMENT (of the abstract entered in Block 20, if different from Report)

9783
06

18. SUPPLEMENTARY NOTES

AFOSR TR-77-0060

19. KEY WORDS (Continue on reverse side if necessary and identify by block number)
TRANSITION FLOW
HEAT TRANSFER

20. ABSTRACT (Continue on reverse side if necessary and identify by block number)

Measurements of the molecular velocity distribution function between differentially heated parallel plates have been obtained for Knudsen numbers in the transition flow range. The gas used was argon and the plate temperature ratio was 1.7. The specific distribution in terms of one velocity component, $\iint f(u,v,w,\underline{x})dvdw$, where the 'u' direction is perpendicular to the plates, was obtained by measuring the Doppler broadening of the 4609.6Å AII spectral line emitted as a result of excitation of the gas by an electron beam. Various plate spacing and pressure

DD FORM 1 JAN 73 1473 EDITION OF 1 NOV 65 IS OBSOLETE

UNCLASSIFIED 178920
SECURITY CLASSIFICATION OF THIS PAGE (When Data Entered)

LB

combinations were used to obtain Knudsen numbers between 0.07 and 3. The eight moment linearized model of Gross and Ziering provided the best overall representation of the data, with the four-moment linearized model of Gross and Ziering and the bimodal solution of Lees predicting a substantially greater degree of asymmetry in the distribution function than was observed at low Knudsen numbers. The constraint placed on the problem by Gross and Ziering to simplify its solution by linearization was that the temperature, $T_{(plates)}/T_{\infty} < 1$. This criterion was not met in our experiment, and the good match between the data and the eight-moment method indicates that the range of validity of linearized solutions may be greater than would be expected based solely on the linearizing condition.

AN EXPERIMENTAL INVESTIGATION OF THE DISTRIBUTION FUNCTION FOR THE NEAR FREE MOLECULAR PARALLEL PLATE HEAT TRANSFER PROBLEM

by

D. T. L. Tong



Submitted October, 1976

December, 1976

UTIAS Report No. 210
CN ISSN 0082-5255

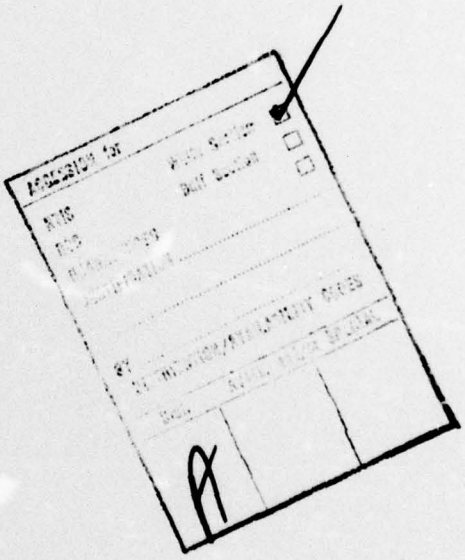
Acknowledgements

The author wishes to thank Dr. J. H. deLeeuw for suggesting the topic and his continuing support throughout the program.

Discussions with W. E. R. Davies of the UTIAS Rocket Group and fellow student Hubert Mercure were very helpful. The electronic skills of Jacob Unger and the technical assistance of the UTIAS shop, particularly Messrs. Ted Mills and Arthur Bragg-Smith are gratefully acknowledged. Mrs. Dorothy Finlay and Mrs. Winifred Dillon typed the manuscript.

My wife Virginia provided not only support and understanding during the entire period, but also helped clarify many ideas through discussion, and to her I dedicate this thesis.

Financial support was provided by the Canadian Defense Research Board under grant number 9510-111 and the United States Air Force Office of Scientific Research under grant number 71-2091 .



Abstract

Measurements of the molecular velocity distribution function between differentially heated parallel plates have been obtained for Knudsen numbers in the transition flow range. The gas used was argon and the plate temperature ratio was 1.7. The specific distribution in terms of one velocity component, $\int_v \int_w f(u,v,w,\underline{x})dvdw$, where the 'u' direction is perpendicular to the plates, was obtained by measuring the Doppler broadening of the 4609.6Å AII spectral line emitted as a result of excitation of the gas by an electron beam. Various plate spacing and pressure combinations were used to obtain Knudsen numbers between 0.07 and 3.

The eight-moment linearized model of Gross and Ziering provided the best over-all representation of the data, with the four-moment linearized model of Gross and Ziering and the bimodal solution of Lees predicting a substantially greater degree of asymmetry in the distribution function than was observed at low Knudsen numbers. The constraint placed on the problem by Gross and Ziering to simplify its solution by linearization was that the temperature difference between the plates be much less than the mean temperature, $\Delta T_{plates}/T_o \ll 1$. This criterion was not met in our experiment, and the good match between the data and the eight-moment method indicates that the range of validity of linearized solutions may be greater than would be expected based solely on the linearizing condition.

TABLE OF CONTENTS

		Page
	Acknowledgements	ii
	Abstract	iii
	Table of Contents	iv
	List of Symbols	vi
1.	INTRODUCTION	1
2.	THE PARALLEL PLATE HEAT TRANSFER PROBLEM	4
	2.1 Layout and Background of the Problem	4
	2.2 Moment Methods	5
	2.2.1 Linearized Forms of the Boltzmann Equation	8
	2.2.2 Bimodal Representations of the Distribution Function	13
	2.2.3 BGK Solutions	15
	2.3 Monte Carlo Methods	16
	2.3.1 Test Particle Methods	16
	2.3.2 Evaluation of the Collision Integral	18
	2.4 Previous Experimental Investigations	18
	2.4.1 Density and Heat Transfer Results	18
	2.4.2 Distribution Function Measurements	19
	2.5 Summary of Results	19
3.	EXPERIMENTAL TECHNIQUE	20
	3.1 Analysis of the Molecular Velocity Distribution Function Using the Electron Beam Fluorescence Technique	20
	3.1.1 The Relationship Between the Doppler Profile of a Spectral Line and the Distribution Function	20
	3.1.2 The Electron Beam Fluorescence Probe	22
	3.1.3 Additional Sources of Line Broadening	23
	3.2 Spectral Analysis Technique	28
	3.2.1 The Ideal Fabry-Perot Interferometer	28
	3.2.2 Additional Effects With Real Fabry-Perot Interferometers	31
4.	EXPERIMENTAL FACILITY	33
	4.1 The UTIAS Low Density Plasma Tunnel	33
	4.2 Parallel Plate Rig	34
	4.3 Electron Gun and Controls	35

		Page
4.4	Optical System	36
4.4.1	Selection of the Spectral Line	36
4.4.2	The Optical System and Counting Circuitry	36
5.	ANALYTICAL METHOD	37
5.1	Sensitivity of Data Fits	40
5.2	Analysis of the Asymmetry of the Distribution Function	46
5.3	Temperature Fits	47
6.	RESULTS AND DISCUSSION	47
6.1	Asymmetry in the Distribution Function	47
6.2	Temperature Profiles	49
6.3	Summary of Results	50
7.	CONCLUSIONS	50
	REFERENCES	53
	FIGURES	
	APPENDIX A - CALIBRATION OF THE FABRY-PEROT SYSTEM	
	APPENDIX B - APPLICATION OF A HIGHER RESOLUTION INTERFEROMETER	
	APPENDIX C - EFFECT OF THE ELECTRON BEAM GENERATED PLASMA ON THE OBSERVED DISTRIBUTION FUNCTION	

List of Symbols

Latin

A	Intensity absorptivity of one interferometer plate (Eq. 3.2.7)
A	Amplitude of light wave (Eq. 3.2.2)
Å	Angstrom
AII	Argon ion
A_{mn}	Einstein coefficient (Eq. 3.1.12)
a	Gain term of collision integral (Eq. 1.2)
a_{rl}	Coefficients of polynomials in Wang Chang and Uhlenbeck's expansion of distribution function (Eq. 2.2.13)
$a_i^{\pm}$	Coefficients of polynomials in Gross' and Ziering's expansion of distribution function (Eq. 2.2.22)
B	Parameter representing density perturbation at a wall (Eq. 2.2.16)
B	Amplitude of transmitted light wave (Eq. 3.2.2)
b	Impact parameter (Eq. 1.1)
bf	Loss term of collision integral (Eq. 1.2)
c	Speed of light (Eq. 3.1.1)
$\underline{c} = (c_x, c_y, c_z)$	Molecular random velocity (Eq. 1.4)
D	Parameter incorporating plate defects in Fourier expansion of instrument function (Eq. 5.1.6)
d	Distance between parallel plates (Eq. 2.2.16)
E	Energy (Eq. 3.1.8)
e	Base of the natural logarithms
F	Finesse (Eq. 3.2.9)
F_o	Fourier representation (Eq. 5.1.2)

f	Focal length of lens (Eq. 3.2.4)
f	Distribution function (Eq. 1.1)
$\mathcal{F}$	Measured distribution function (Eq. 3.1.2)
$\mathcal{F}$	Net body force (Eq. 1.1)
$\underline{g}$	Relative velocity between two molecules (Eq. 1.1)
h	Planck's constant (Eq. 3.1.8)
h	Perturbation term in Wang Chang and Uhlenbeck's expansion of distribution function (Eq. 2.2.12)
h	Etalon plate spacing (Eq. 3.2.1)
I	Light intensity (Eq. 3.1.7)
I_{coll}	Collision integral in Boltzmann equation (Eq. 1.1)
$\underline{i}$	Unit vector (Eq. 3.1.1)
j	Particle current (Eq. 2.2.26)
κ	Thermal conductivity of a medium (Eq. 2.1.1)
k	Boltzmann's constant (Eq. 1.4)
Kn	Knudsen number
L	Parameter relating natural and instrument line widths (Eq. 5.1.5)
M	Parameter relating coefficient of Fourier expansion of Doppler profile to mean molecular speed (Eq. 5.1.9)
M	Mach number (Eq. 2.2.39)
m	Flatness figure for interferometer plates
m	Mass of a gas particle (Eq. 1.1)
n	Index of refraction (Eq. 3.2.1)
n	Particle number density (Eq. 1.4)
n	Term index in trigonometric expansion (Eq. 5.1.2)
P	Etalon chamber pressure (Eq. 5.1.12)
p	Order number (Eq. 3.2.2)

p_{xx}	Stress tensor component normal to plates (Eq. 2.2.30)
q	Heat flux (Eq. 2.1.1)
R	Intensity reflectivity of one interferometer plate (Eq. 3.2.2)
r	Amplitude reflectivity of one interferometer plate
r	Radial coordinate in interference pattern (Eq. 3.2.4)
T	Intensity transmission factor for one interferometer plate (Eq. 3.2.2)
T	Temperature (Eq. 1.4)
t	Time (Eq. 1.1)
t	Amplitude transmission factor of one interferometer plate
t	Statistical parameter
$\underline{U}$	Bulk velocity of a gas (Eq. 1.4)
$\underline{u}$	Relative velocity between photon emitter and observer (Eq. 3.1.1)
$\underline{v}$	Total velocity of a molecule (Eq. 1.1)
$\underline{x}$	Position (Eq. 1.1)
x	Running coordinate between parallel plates (Eq. 2.1.1)
y	Generalized ordinate (Eq. 5.1)

Greek

α	Energy accommodation coefficient (Eq. 2.2.11)
α_2, α_3	Integration constants in bimodal model development (Eqs. 2.2.41, 2.2.42)
γ	Ratio of specific heats of a gas (Eq. 2.2.39)
Δ	Change in a parameter
ϵ	Azimuthal angle coordinate for intermolecular collisions (Eq. 1.1)

λ	Mean free path (Eq. 2.2.20)
λ	Wavelength of light (Eq. 3.1.1)
$< \Delta\lambda >$	Free spectral range (Eq. 3.2.5)
ν	Collision frequency (Eq. 2.2.45)
σ	Differential scattering cross-section (Eq. 3.1.24)
θ	Primary electron deflection angle (Eq. 3.1.22)
θ	Angle between light beam and interferometer axis (Eq. 3.2.1)
τ	Time (Eq. 3.2.2)
φ	Generalized molecular velocity dependent function (Eq. 2.2.1)
$\phi^{\pm}$	Perturbation terms in Gross and Ziering's expansion of the distribution function (Eq. 2.2.21)
ψ_{rl}	Orthogonal polynomials in Wang Chang and Uhlenbeck's expansion of the distribution function (Eq. 2.2.13)
Ω	Solid angle
ω	Angular frequency (Eq. 3.2.2)

Superscripts

+	+x direction
-	-x direction
'	Before collision
$\overline{\quad}$	Average
(r)	Iteration number

Subscripts

+	+x direction
-	-x direction
$\parallel$	Parallel to plates
$\perp$	Perpendicular to plates
*	On axis
A	Atom

centre	At fringe peak
cold	Value at cold plate
D	Doppler
e	Electron
exp	Experimental
FM	Free-molecular
fit	Best fit value
fsr	Free spectral range
hot	Value at the hot plate
I	Imperfection
l	Lower state
Max	Maxwellian
max	Maximum
mfp	Mean free path
N	Natural
OBS	Observed
P	Pinhole
R	Reflectivity
T	Temperature
U	Unknown
u	Upper state
x	Normal to plates
o	Centre value
o	Mean value in linearized model
1	Collision partner

1. INTRODUCTION

During the past twenty years there has been an increased interest in the behaviour of rarefied gases as a result of upper atmosphere and space exploration, and the application of vacuum techniques to manufacturing and research systems. The empirical continuum fluid mechanics equations lose validity when the mean free path of the fluid particles is no longer much less than the characteristic dimension of the system under study, and a detailed knowledge of the behaviour of the gas or plasma at the molecular level is required. Over a hundred years ago Boltzmann formulated the equation which describes this behaviour, but no exact analytic technique is available for treating problems where the mean free path is of the same order as the significant length (the transition regime). Many approximate and numerical solution methods have been used to provide answers in the transition regime, and the experiments presented in this paper are compared with various theoretical results for the problem of one-dimensional heat flow between parallel plates.

The basic property of a fluid from which can be derived all its macroscopic properties is the molecular velocity distribution function, f, which is a six-fold density distribution in the phase space consisting of three spatial and three velocity components. Thus the number of molecules in any cell in phase space is $dN(\underline{v},\underline{x}) = f(\underline{v},\underline{x})dv_x dv_y dv_z\, dxdydz$. The Boltzmann equation relates the substantive derivative of f to the change due to collisions between molecules:

$$\frac{Df}{Dt} = I_{coll} \tag{1.1}$$

where

$$\frac{Df}{Dt} = \frac{\partial f}{\partial t} + \underline{v} \cdot \frac{\partial f}{\partial \underline{x}} + \frac{\underline{\mathcal{F}}}{m} \cdot \frac{\partial f}{\partial \underline{v}} \tag{1.1a}$$

is a generalized form of the substantive derivative in which the temporal variation of f is dependent on the spatial variation not only with respect to the three position coordinates, but also the three velocity ones, and the collision integral is:

$$I_{coll} = \int_{all\ \underline{v}_1} \int_{b=0}^{\infty} \int_{\epsilon=0}^{2\pi} (f'f'_1 - ff_1)\underline{g}b\, db\, d\epsilon\, d\underline{v}_1 \tag{1.1b}$$

with its individual components defined as follows, for the collision geometry shown in Fig. 1.1:

f_1 is the after-collision distribution function for the "collision partners" - the particles in each collision which neither enter nor leave the velocity cell bounded by $\underline{v}$ and $\underline{v} + d\underline{v}$,

$\underline{v}_1$ is the velocity of the collision partner,

f' and f'_1 are the "before-collision" distribution functions,

$\underline{g} = (\underline{v} - \underline{v}_1)$ is the relative velocity between the two colliding particles,

b is the "impact parameter", the distance by which the centres of the two particles would miss if there were no interactive force,

ϵ is the azimuthal angle between the projection of the relative velocity on a reference plane and some reference vector in that plane,

m is the particle mass,

$\mathcal{F}$ is the net body force.

The collision integral is often broken down into its gain and loss components by using the notation:

$$I_{coll} = a - bf \tag{1.2}$$

where a represents the gain term from collisions and bf is used for the loss term as a reminder that the loss-rate is proportional to f.

When the gas behaviour is collision-dominated, the full Boltzmann equation approaches the homogeneous integral equation:

$$I_{coll} = 0 \tag{1.3}$$

which has the solution:

$$f_{Max}(\underline{c},\underline{x}) = n(\underline{x}) \left(\frac{m}{2\pi kT} \right)^{3/2} e^{-\frac{m(\underline{v}-\underline{U})^2}{2kT}} \tag{1.4}$$

where $\underline{v}$ is the total velocity of a particle and $\underline{U}$ is the bulk average velocity of the gas, and $\underline{c} = \underline{v} - \underline{U}$. This solution is known as the Maxwellian distribution function.

The parameter defining the relative importance of collisions is the Knudsen number, Kn, the ratio of the gas particle mean free path to some dimension characteristic of the system under study. The collision dominated, or "continuum" regime is characterized by low Knudsen numbers ($\lesssim 0.1$), and its behaviour is described by the Navier-Stokes equations of "conventional" fluid mechanics. At Knudsen numbers greater than 10 the gas itself is essentially collision free, and the behaviour of macroscopic parameters of engineering interest, such as drag or heat transfer to a space vehicle in free-molecular flow, is governed by the nature of the interaction between the individual gas particles and the body. In the regime intermediate to these two, known as transition flow, gas-gas and gas-body collisions occur with roughly equal frequency, and both sides of the Boltzmann equation must be retained.

Many attempts have been made to linearize, simplify, or simulate the full Boltzmann equation to obtain solutions under transition conditions, but the results of different methods often vary significantly. Therefore, before it can be determined which approach to take in applying the equation to the solution of problems of scientific or engineering interest, the various solution methods must be applied to cases which are both mathematically tractable and experimentally verifiable so that a greater understanding of their behaviour can be achieved.

One such case is that of heat transfer between plane parallel plates. The equation becomes one-dimensional, and hence greatly simplified, and in principle experimental results should be readily obtainable. Various methods have been used to obtain the heat transfer rate and temperature and density profiles between the plates as functions of Knudsen number by "solving" the equation in its simplified form applicable to this case:

$$c_x \frac{\partial f}{\partial x} = I_{coll} \qquad (1.5)$$

Experimental results to which these methods could be compared have so far not been definitive. One set of heat transfer measurements (Ref. 1) and two sets of density profile traces (Refs. 1,2) have been made. The results of these experiments closely matched those predicted by one method of simplifying the problem - the assumption of a bimodal distribution function composed of two "half-Maxwellians" for the groups of molecules moving in opposite directions perpendicular to the plates. Computer solutions using a modified form of the collision integral, and which were derived subsequent to the presentation of the experimental results, have tended to favour a different model, one in which the distribution function is assumed to be simply a perturbed single Maxwellian. Consequently, experimental measurements of the distribution function itself would be valuable in resolving the disparity between these two sets of results.

The measurement of Doppler broadening of a single line in the fluorescence spectrum of a gas excited by an electron beam has been employed for some time to measure near-equilibrium distribution functions, and its application to the parallel plate heat transfer problem was attempted once before (Ref. 3), using helium as the test gas between plates having a temperature ratio of two. The results could not be quantitatively compared to any of the model solutions, and only qualitatively compared to the bimodal one, because of the poor efficiency of energy transfer between the plates and the helium, which made the boundary conditions the dominant factor in the solution of the problem. Unlike helium, argon accommodates very well to the surfaces on which it is adsorbed, and hence is preferable for a study of this problem.

In the experiment reported here the electron beam fluorescence method was used to measure both temperature profiles and the degree of asymmetry in the distribution function for argon gas between plates having a temperature ratio of 1.7, and at Knudsen numbers near unity.

2. THE PARALLEL PLATE HEAT TRANSFER PROBLEM

The problem of the conductive heat transfer between infinite plane parallel plates at different temperatures is one of the most extensively studied in the fields of kinetic theory and rarefied gas dynamics. Most of the work done so far has been theoretical, with numerous attempts at modelling or simplifying the Boltzmann equation in order to solve it directly for the distribution function, or obtain moments of experimental interest, such as the density or heat transfer rate. This problem has also been studied using various forms of Monte Carlo methods, but there has been very little experimental treatment so far.

2.1 Layout and Background of the Problem

The generalized parallel plate heat transfer problem is shown in Fig. 2.1.1. Two plane, parallel infinite plates are separated by a distance d. One plate is at an elevated temperature, T_{hot}, and the other at a lower temperature, T_{cold}, with heat being conducted from the hot to the cold plate by means of the gas particles in between. In the limiting case of continuum flow, the gas at any point between the plates has a near-Maxwellian distribution function characterized by a single temperature, with the heat flux given by Fourier's Law:

$$q = - k dT/dx \qquad (2.1.1)$$

where k is the thermal conductivity of the gas and is independent of the density, so that the heat flux is also density-independent. If the distance between the plates is decreased, then the number of collisions each molecule undergoes during a traverse from one plate to the other also decreases, until the free molecular limit of no collisions is reached. In this case the heat conduction is independent of plate spacing, varying only with the wall temperatures and accommodation coefficients and, in contrast to the continuum case, in direct proportion to the density of the gas. In the transition range of Knudsen numbers neither the continuum nor free-molecular solution is applicable, and hence the full Boltzmann equation including realistic wall accommodation models must be solved for the distribution function and resultant heat transfer rate. Although in principle this can be done, the complexity of the equation prohibits analytic solution, and consequently some simplifying assumptions or approximations must be made.

The most common method of solution of the Boltzmann equation for this problem is the moment method, in which suitable boundary conditions and constraints are imposed and lower order moments of the distribution function are evaluated. Some form for the distribution function, defined by n parameters, is assumed and then n moment equations are solved for these parameters. In order to make the problem tractable, the Boltzmann equation is often linearized by assuming that the temperature difference between the plates is much less than the mean temperature, so that expansions about a Maxwellian are possible (Refs. 4,5), and the perturbation parameters can be calculated. Another form of solution similar to this, but not restricted to small temperature differences, is the BGK method, in which the collision integral is replaced by the product of a collision frequency parameter times the difference

between the distribution function and a Maxwellian (Refs. 6,7,8,9,10). The nonlinear problem has also been treated by the assumption of a bimodal distribution function composed of two distinct half-Maxwellians for the groups of molecules moving in each direction normal to the plates (Refs. 11,12,13) with the temperatures and densities of each half being the parameters.

Monte Carlo techniques have also been applied to the solution of the heat transfer problem. One form originally put forth by Nordsieck uses a statistical sampling procedure to determine points in velocity space at which the collision integral is to be numerically integrated, and hence the complete Boltzmann equation solved for f (Refs. 8,9,14). The second, and most common, technique is the test particle method (Refs. 15,16,17,18,19), which utilizes the property of the distribution function that, if any individual gas particle is followed for a sufficiently long time, then the fraction of the total time it spends in any given cell in phase space is directly proportional to the value of the distribution function for that cell. A form of the function is initially assumed and then a single test particle is followed through a series of collisions with the rest of the gas molecules, and the length of time it spends in each cell in velocity space is recorded. After a predetermined number of collisions the time history of the test particle is used to produce a new distribution function for the target gas, and the process is repeated until there is no appreciable change between iterations. A third form of Monte Carlo solution is Bird's (Ref. 20) direct simulation method, in which all of the particles in the model gas are allowed to collide and the actual distribution function is measured after a certain number of collisions per particle.

Only two sets of experimental measurements have been made previous to this study. The first was a measurement of the density distribution between the plates and the heat transfer rate for both small (Ref. 1) ($\Delta T_{plates}/T_o \leq 0.28$) and large (Ref. 2) ($T_{hot}/T_{cold} = 4$) temperature differences between the plates, and the second was an attempt to measure the distribution function in helium between plates with a temperature ratio of two (Ref. 3). In the first study the results strongly favoured the bimodal four-moment model. Since the publication of these experimental results, accurate BGK solutions have been obtained, and they more closely matched the eight-moment linearized model than the bimodal one, so that there is a discrepancy between these original experimental results and more recent theoretical ones. One of the major differences between the two sets of models is the predicted degree of asymmetry in the distribution function, so that direct measurement of the distribution itself would be a means of resolving the difference. It was this measurement which was attempted in the second experimental study, but the low ($\lesssim 0.4$) energy accommodation coefficients encountered made quantitative comparison with the different models impossible, because the measured distribution was not indicative of the actual process being modelled (near total accommodation). Consequently only qualitative, and hence not definitive, comparisons could be made with theory.

A summary of the various analytical methods and their results is presented below, with the results shown graphically in Fig. 2.1.2 for comparison.

2.2 Moment Methods

Moment method solutions of kinetic theory problems are obtained by defining the distribution function in parametric form and then solving for

the parameter values which satisfy a set of equations involving integral moments of the distribution function. By multiplying both sides of the Boltzmann equation by some velocity dependent function $\varphi(\underline{v})$ and integrating over all velocities, one obtains Maxwell's equation of transfer:

$$\int_{\underline{v}} \varphi(\underline{v}) \left[\frac{\partial f}{\partial t} + \underline{v} \cdot \frac{\partial f}{\partial \underline{x}} + \frac{\underline{\mathcal{F}}}{m} \cdot \frac{\partial f}{\partial \underline{v}} \right] d\underline{v} = \int_{\underline{v}} \varphi(\underline{v}) I_{coll} d\underline{v} \quad (2.2.1)$$

which for the present problem having no body forces and one dimensional steady flow reduces to

$$\frac{d}{dx} \int_{\underline{v}} \varphi(\underline{v}) v_x f \, dv = \int_{\underline{v}} \varphi(\underline{v}) I_{coll} d\underline{v} \quad (2.2.1a)$$

If the functions $\varphi(\underline{v})$ are chosen such that they can be related to known macroscopic gas properties, then the averaging property of the moments of the distribution function can be employed to relate the distribution function itself to these measurable parameters. Because the distribution function is a density distribution in velocity space, the mean value of any function, $\varphi(\underline{v})$, is simply given by:

$$\overline{\varphi(\underline{v})} = \frac{1}{n} \int_{\underline{v}} \varphi(\underline{v}) f \, d\underline{v} \quad (2.2.2)$$

Substitution of this property into the reduced form of the transfer equation yields:

$$\frac{1}{n} \frac{d}{dx} \overline{(\varphi(\underline{v}) v_x)} = \int_{\underline{v}} \varphi(\underline{v}) I_{coll} d\underline{v} \quad (2.2.3)$$

If collisional invariants, such as mass, linear momentum, or particle kinetic energy (for elastic collisions) are chosen as the $\varphi(\underline{v})$'s, then the equation can be further reduced to:

$$\frac{d}{dx} \overline{(\varphi(\underline{v}) v_x)} = 0 \quad (2.2.3a)$$

specific applications of which are now presented.

The lowest order collisional invariant is mass, and the transfer equation with $\varphi(\underline{v}) = m$ becomes:

$$\frac{d}{dx} \int_{\underline{v}} m \, v_x \, f \, d\underline{v} = 0 \quad (2.2.4)$$

or

$$\frac{d}{dx} \overline{(nm \, v_x)} = 0 \quad (2.2.5)$$

Since the mass of the particle is obviously fixed, this reduces to $m\,\overline{v_x}$ = constant. However, there is an imposed requirement for the steady-state solution that there be no net accommodation or ablation at any surface, and hence no net mass flux. Therefore $m\,\overline{v_x} = 0$, which gives the first equation involving the distribution function itself:

$$\int_{\underline{v}} v_x\, f\, d\underline{v} = 0 \qquad (2.2.6)$$

The second equation involving a collisional invariant is that for x-momentum, $m\,v_x$, which results in the equation

$$\frac{d}{dx}\int_{\underline{v}} m\, v_x\, v_x f\, d\underline{v} = 0 \qquad (2.2.7)$$

or

$$\frac{d}{dx}\left(n\,\overline{m\,v_x^2}\right) = 0 \qquad (2.2.8)$$

which states that the x-component of the stress tensor is a constant between the plates.

The elastic collision constraint with $\varphi(v) = 1/2\, m\, \underline{v}^2$ gives the actual heat flow relationship:

$$\frac{d}{dx}\left(\frac{1}{2}\, m \int \underline{v}^2\, v_x\, f\, d\underline{v}\right) = 0 \qquad (2.2.9)$$

or

$$\frac{d}{dx}\left[\frac{1}{2}\, n\, m\, \overline{\underline{v}^2\, v_x}\right] = 0 \qquad (2.2.10)$$

But $1/2\, n\, m\, \overline{\underline{v}^2 v_x}$ is the rate of thermal energy transport across a unit area between the plates, so this equation states that, as expected, the normal heat flux between the plates is constant. Because in transition flow the effects of collisions between gas particles are important, at least one higher order moment not involving collisional invariants is necessary for the complete solution, and the resulting moment equation requires evaluation of the collision integral.

The moment equations are not in themselves sufficient for solution of the heat transfer problem, and a suitable boundary condition must be imposed. A frequently used condition is the assumption that a fraction, α, of the incoming molecules is totally accommodated at the wall and re-emitted with a Maxwellian distribution corresponding to the wall temperature, and the remaining fraction, $1 - \alpha$, is specularly reflected, so that the distribution functions are:

$$f^{+}_{(x=0)} = \alpha_{hot}\, f_{Max}(T_{hot}) + (1 - \alpha_{hot}) f^{-}_{(x=0)} \qquad (2.2.11a)$$

$$f^-_{(x=d)} = \alpha_{cold}\, f_{Max}(T_{cold}) + (1 - \alpha_{cold}) f^+_{(x=d)} \qquad (2.2.11b)$$

In principle, the accommodation coefficients at each wall can be different, but they are usually assumed to be the same, so that $\alpha_{hot} = \alpha_{cold} = \alpha$.

The following sections present a representative, but not exhaustive, sample of some applications of the moment method to the solution of the parallel plate heat transfer problem.

2.2.1 Linearized Forms of the Boltzmann Equation

Wang Chang and Uhlenbeck were the first to intensively study transport phenomena in the near-free-molecular regime, with the linearized heat transfer problem presented as one of a series of reports (Ref. 4). The two plate temperatures were defined as $T_o \pm \Delta T$, with $\Delta T \ll T_o$. Fractional accommodation, α, was allowed at each plate. The origin of the coordinate system was at the midplane, with the plate at $x = d/2$ having a temperature of $T_o - \Delta T$ and that at $x = -d/2$ being maintained at $T_o + \Delta T$.

The distribution function was a perturbed Maxwellian of the form

$$f = f_{Max}[1 + h(\underline{c},x)] \qquad (2.2.12)$$

where $\underline{c} = \underline{v}\sqrt{m/2kT_o}$, and h was expressed as a sum of polynomials both space and velocity dependent

$$h = \sum_{r,l} a_{rl}(x)\psi_{r,l}(c^2,c_x) \qquad (2.2.13)$$

where the $\psi_{r,l}$ were defined in terms of Legendre and Sonine polynomials.

The linearization simplified the Boltzmann equation to:

$$c_x \frac{\partial h}{\partial x} = n\, I_{coll}(h) \qquad (2.2.14)$$

a linear integro-differential equation in h. The polynomial expansion of h changed the simplified single Boltzmann equation to a doubly infinite set of linear equations in the coefficients a_{rl}:

$$\frac{d\, a_{rl}}{dx} = n \sum_{r',l'} a_{r'l} \int \frac{1}{c_x}\, \psi_{r,l}\, I_{coll}(\psi_{r',l'}) e^{-\underline{c}^2}\, d\underline{c} \qquad (2.2.15$$

Utilizing the fact that the linearized problem was symmetric, the boundary condition became

$$h^+\left(c_x, -\frac{d}{2}\right) = \alpha \frac{\Delta T}{T}(c^2 + B) + (1 - \alpha)h^-\left(-c_x, -\frac{d}{2}\right),\ c_x > 0 \qquad (2.2.16)$$

where

$$h^{\pm}(c_x,x) = - h^{\mp}(-c_x,-x) \tag{2.2.17}$$

and B was a parameter representing the density perturbation at the wall, to be determined from the boundary conditions. The collision integral was evaluated using Maxwell molecules. Successive approximations, each one using one more term in the expansion of h than the previous one, were evaluated for the heat flux:

$$q = \frac{nkT}{\pi^{3/2}} \sqrt{\frac{2kT}{m}} \int_{\underline{c}} c^2 \, c_x \, e^{-c^2} \, h \, d\underline{c} \tag{2.2.18}$$

and inter-plate temperature distribution

$$T_{(x)} = T_o \left[1 - \frac{2}{3\pi^{3/2}} \int_{\underline{c}} e^{-c^2} \left(\frac{3}{2} - c^2 \right) h \, d\underline{c} \right] \tag{2.2.19}$$

The expansions were computationally complex, and were only carried out to the third approximation in the report. Because it is the easiest to compute, only involving eight terms in the derivation, the second approximation is the one usually quoted. Each higher order approximation drops the value of the normalized heat transfer rate for a given Knudsen number, but the convergence is slow. The temperature distribution between the plates for the second approximation is:

$$T_{(x)} = T_o \left\{ 1 - \frac{2\Delta T}{T_o} \left[\frac{x}{d} \left(\frac{15}{4\sqrt{15\pi}} \sinh\left(\frac{\sqrt{15}\, d}{8\lambda} \right) + \frac{2-\alpha}{2\alpha} \cosh\left(\frac{\sqrt{15}\, d}{8\lambda} \right) \right) \right.\right.$$

$$\left. + \frac{2-\alpha}{2\alpha} \cdot \frac{\lambda}{\sqrt{15}\, d} \cdot \sinh\left(\frac{\sqrt{15}\, x}{4\lambda} \right) \right] \cdot \left[\frac{15}{4\sqrt{15\pi}} \sinh\left(\frac{\sqrt{15}\, d}{8\lambda} \right) \right.$$

$$+ \frac{2-\alpha}{2\alpha} \cdot \cosh\left(\frac{\sqrt{15}\, d}{8\lambda} \right) + \frac{2-\alpha}{2\alpha} \cdot \frac{5\sqrt{\pi}\,\lambda}{d} \left(\frac{39}{10\sqrt{15\pi}} \cdot \sinh\left(\frac{\sqrt{15}\, d}{8\lambda} \right) \right.$$

$$\left.\left. \left. + \frac{2-\alpha}{2\alpha} \cosh\left(\frac{\sqrt{15}\, d}{8\lambda} \right) \right]^{-1} \right\} \tag{2.2.20}$$

which can be used to determine the temperature slip at the wall by substituting $x = \pm\, d/2$. As in the case for the heat transfer rate, there is a decrease in slip with increasing level of approximation. Consequently, the standard usage of the second approximation in the literature may produce deceptively high values for both properties.

Gross and Ziering (Ref. 5) also produced a solution for the linearized problem, in this case expanding the distribution function in terms of a low order power series in velocity:

$$f^{\pm} = f_{Max}(T_o)(1 + \phi^{\pm}) \tag{2.2.21}$$

where

$$\phi^{\pm} = a_o^{\pm}(x) + a_1^{\pm}(x)c_x + a_2^{\pm}(x)c^2 + a_3^{\pm}(x)c^2 c_x \tag{2.2.22}$$

Their c's are nondimensionalized velocities with $c_i = v_i \sqrt{m/2kT_o}$ and ϕ is analogous to Wang Chang and Uhlenbeck's h, which becomes obvious from the boundary and symmetry conditions:

$$\phi^{+}\left(x = -\frac{d}{2}\right) = \frac{\alpha\Delta T}{T}(c^2 + B) + (1 - \alpha)\,\phi^{-}\left(x = -\frac{d}{2},\, -c_x\right) \quad c_x > 0 \tag{2.2.24}$$

$$\phi^{\pm}(c_x, x) = -\phi^{\mp}(-c_x, -x) \tag{2.2.25}$$

The values of the eight coefficients are obtained by solving eight half-range moment equations in which each of the integrations is performed over one-half of velocity space only. A summary of the solution method follows.

If $j^{\pm}$ represent the "particle currents" in the $\pm x$ direction, then

$$j^{\pm} = \int_{v_x \gtrless 0} v_x f^{\pm}\, d\underline{v} \tag{2.2.26}$$

If the collision integral is denoted by $\delta f/\delta t$, the Boltzmann equation is written

$$v_x \frac{\partial f}{\partial x} = \frac{\delta f}{\delta t} \tag{2.2.27}$$

with the corresponding transfer (moment) equation for $j^{\pm}$ being

$$\frac{\partial}{\partial x}(j^{\pm}) = \int_{v_x \gtrless 0} \frac{\delta f}{\delta t}\, d\underline{v} \tag{2.2.28}$$

Integration of both sides with respect to $\underline{v}$ over half ranges in the x-component yields the two-moment equations, with the no-net-flow condition being

$$j^{+} + j^{-} = 0 \tag{2.2.29}$$

Applying the second collisional invariant (conservation of momentum) and integrating both sides of the Boltzmann equation yields:

$$\frac{\partial}{\partial x}\left(\frac{p_{xx}^{\pm}}{m}\right) = \int_{v_x \gtrless 0} v_x \frac{\delta f}{\delta t}\, d\underline{v} \tag{2.2.30}$$

with the restriction

$$\frac{\partial}{\partial x}\left(p_{xx}^{+} + p_{xx}^{-}\right) = 0 \tag{2.2.31}$$

The next highest order moment is that for the kinetic energy transport rate across unit area:

$$q_x^{\pm} = \frac{1}{2} m \int_{v_x \gtrless 0} v_x v^2 f^{\pm} \, d\underline{v} \tag{2.2.32}$$

which yields the moment equation:

$$\frac{\partial}{\partial x} q_x^{\pm} = \frac{m}{2} \int_{v_x \gtrless 0} v^2 \frac{\delta f}{\delta t} \, d\underline{v} \tag{2.2.33}$$

again with a conservation restriction

$$\frac{\partial}{\partial x}\left(q_x^{+} + q_x^{-}\right) = 0 \tag{2.2.34}$$

The final moment equation was

$$\frac{\partial}{\partial x} \int_{v_x \gtrless 0} v_x^2 \frac{mv^2}{2} f^{\pm} \, d\underline{v} = \int_{v_x \gtrless 0} v_x \frac{mv^2}{2} \frac{\delta f}{\delta t} \, d\underline{v} \tag{2.2.35}$$

This is the equation which took into account the effect of intermolecular collisions by relating the flow of "heat current" to its alteration by the collisions. The left sides of all eight equations were formed immediately by substituting the polynomial expansions for $\phi^{\pm}$ into the moment equations and integrating with the weight factor e^{-c^2} from the Maxwellian $[f = f_{Max}(1 + \phi^{\pm})]$. The resulting physical quantities, which are presented below, were then substituted into the transfer equations in order to determine the coefficients $a_i^{\pm}$.

$$n^{\pm} = \frac{n_o}{2}\left\{ a_o^{\pm} \pm \frac{a_1^{\pm}}{\sqrt{\pi}} + \frac{3a_2^{\pm}}{2} \pm \frac{2a_3^{\pm}}{\sqrt{\pi}} + 1 \right\} \tag{2.2.36a}$$

$$j^{\pm} = \frac{2kT_o}{m}\left\{ \pm \frac{a_o^{\pm}}{\sqrt{\pi}} + \frac{a_1^{\pm}}{2} \pm \frac{2a_2^{\pm}}{\sqrt{\pi}} + \frac{5}{4} a_3^{\pm} \right\} \tag{2.2.36b}$$

$$p_{xx}^{\pm} = nkT_o\left\{ a_o^{\pm} \pm \frac{2a_1^{\pm}}{\sqrt{\pi}} + \frac{5}{2} a_2^{\pm} \pm \frac{6}{\sqrt{\pi}} a_3^{\pm} + 1 \right\} \tag{2.2.36c}$$

$$q_x^{\pm} = nkT\sqrt{\frac{2kT}{m}}\left\{\pm\frac{a_o^{\pm}}{\sqrt{\pi}} + \frac{5}{8}a_1^{\pm} \pm \frac{3}{\sqrt{\pi}}a_2^{\pm} + \frac{35}{16}a_3^{\pm}\right\} \qquad (2.2.36d)$$

$$T = T_o\left\{1 + \frac{(a_1^+ - a_1^-)}{6\sqrt{\pi}} + \frac{(a_2^+ + a_2^-)}{2} + \frac{(a_3^+ - a_3^-)}{\sqrt{\pi}}\right\} \qquad (2.2.36e)$$

Evaluation of the right hand sides of the transfer equations was unwieldly because of the interaction with the collision integral, so the solutions were presented in a reduced form suitable for computation. Hard sphere solutions were presented initially (Ref. 5), and later results were given for Maxwell molecules (Ref. 53). The hard sphere heat transfer rate was slightly greater than that for Maxwell molecules, but the difference between the two different molecular models was slight.

These results showed an even lower heat transfer rate than the third approximation of Wang Chang and Uhlenbeck, and the inter-plate density and temperature profiles were both steeper. This solution was also the first which explicitly evidenced a Knudsen layer, the region within about a mean free path of the plate surface in which the transition from a purely collision-dominated flow to one containing a significant number of particles desorbed from the wall takes place. It is in this "kinetic boundary layer" that the greatest departure from equilibrium occurs in the distribution function, and also where the slopes of the temperature and density profiles increase over their mid-plate values. It was these slope changes which were produced by the eight-moment solution, but not the four-moment ones.

A four-moment solution for hard sphere molecules was also presented, with the perturbations being defined by

$$\phi^{\pm} = a_o^{\pm} + a_2^{\pm}c^2 \qquad (2.2.37)$$

In this case each of the moment equations was integrated over the full range of v_x, in contrast to the eight-moment solution which used only half-range integrations.

The results from this procedure were very close to Wang Chang and Uhlenbeck's in the density and temperature profiles between the plates but the predicted heat transfer rate was about 5% lower than the second approximation value but still significantly higher (~ 10%) than the eight-moment method value.

An advantage of Gross' and Ziering's method over that of Wang Chang and Uhlenbeck is the relative ease with which the actual distribution function can be computed, as a result of the simple power series expansion of the perturbation term, so that comparison with the experiment is much easier.

2.2.2 Bimodal Representations of the Distribution Function

Lester Lees (Ref. 11) first proposed the 'two-stream' Maxwellian form of the distribution function to satisfy the following requirements:

(1) It must have the 'two-sided' character that is an essential feature of highly rarefied gas flows, and especially of nonlinear rarefied flows.

(2) It must be capable of providing a smooth transition from rarefied flows to the classical Navier-Stokes regime.

(3) It should lead to the simplest possible set of differential equations and boundary conditions consistent with (1) and (2).

There is a large class of functions satisfying (1) and (2), two members of which were shown in the previous section. Lees proposed to satisfy the third requirement as well by introducing a bimodal function made up of two half-Maxwellians, as shown below, with his form modified in order to match our specific case.

All of the molecules moving in the +x direction have a distribution function of the form

$$f^{+}(x) = n^{+}(x)\left(\frac{m}{2\pi kT^{+}(x)}\right)^{3/2} e^{-\frac{m\underline{c}^{+2}(x)}{2kT^{+}(x)}} \qquad (2.2.38a)$$

and all those moving in the -x direction have

$$f^{-}(x) = n^{-}(x)\left(\frac{m}{2\pi kT^{-}(x)}\right)^{3/2} e^{-\frac{m\underline{c}^{-2}(x)}{2kT^{-}(x)}} \qquad (2.2.38b)$$

Since the study was for Couette flow with the plates at different temperatures, the pure heat transfer problem was just the limiting case of $M \to 0$. The rarefaction parameter used in the study, Re/M, was related to the inverse Knudsen by

$$\frac{Re}{M} = \sqrt{\frac{\pi\gamma}{2}}\left(\frac{d}{\lambda_{cold}}\right) \qquad (2.2.39)$$

and the wall boundary condition was $\alpha = 1$.

Using Maxwell molecules, the four lowest order moments (the minimum set for a complete solution including the effect of collisions), and normalizing all parameters by their cold plate values, the required parameter equations were derived as:

Continuity

$$\underline{n}^{+}\sqrt{\underline{T}^{+}} = n^{-}\sqrt{\underline{T}^{-}} \tag{2.2.40}$$

Momentum

$$\underline{n}^{+}\underline{T}^{+} + \underline{n}^{-}\underline{T}^{-} = \alpha_2 \tag{2.2.41}$$

Energy

$$\underline{n}^{-}\sqrt{\underline{T}^{-}}\,(\underline{T}^{+} - \underline{T}^{-}) = \alpha_2\alpha_3 \tag{2.2.42}$$

Heat Flux

$$\frac{d}{dx}\left(\underline{n}^{+}\underline{T}^{+2} + \underline{n}^{-}\underline{T}^{-2}\right) + \frac{4}{15}\cdot\frac{d}{\lambda_{cold}}\alpha_2\alpha_3(\underline{n}^{+} + \underline{n}^{-}) = 0 \tag{2.2.43}$$

where the underlined variables are the normalized forms, and the α's are integration constants which were determined from the boundary conditions. These equations were solved for the inter-plate density and temperature profiles as well as the heat transfer rate (normalized by its free-molecular value) as a function of Knudsen number. The resultant temperature profile was flatter than that for Gross' and Ziering's eight-moment method and had no change of slope near the plates, so that the level of temperature slip was greater. The heat transfer rate was within a few percent of the four-moment values of Wang Chang and Uhlenbeck and Gross and Ziering.

Lavin and Haviland (Ref. 13) adopted a similar scheme and solved the equations for hard sphere molecules. The results were very similar to Lees', but with the hard sphere heat transfer rate slightly greater than the equivalent Maxwell molecule value at the same Knudsen number. This increase of a few percent in heat flux in going from one molecular model to the other is consistent with the eight-moment results of Gross and Ziering, which also exhibited a higher value for hard sphere collisions. A second solution was obtained by Lavin and Haviland using six moments instead of four. It was observed that only the eight-moment model had successfully produced evidence of the Knudsen layer, and it was hoped that the addition of two more equations to the bimodal solution would have the same result. Consequently the distribution function was modified to

$$f^{\pm} = \frac{2n^{\pm}(x)m^{3/2}}{(2\pi k)^{3/2}\sqrt{T_{\perp}^{\pm}}\,T_{\parallel}^{\pm}}\; e^{-\frac{m}{2k}\left(c_x^{\pm 2}/T_{\perp}^{\pm} + (c_y^{\pm 2} + c_z^{\pm 2})/T_{\parallel}^{\pm}\right)} \tag{2.2.44}$$

with $T_{\parallel}^{\pm}$ being the two new parameters and the next two lowest moments in c_x being the required equations. Maxwell molecules were used, and the results for both the heat transfer rate and the temperature distribution were very close to Lees' results. This, coupled with the absence of a Knudsen layer, suggested that there was no advantage to be gained by increasing the complexity of the solution by going beyond four moments

in the full range solution. The authors also observed that the heat flux and temperature slip values predicted by any given model increased only slightly as the temperature ratio was raised from values applicable to the linearized models (near unity) to higher levels (say 4:1). In contrast, the difference between the four- and eight-moment solutions was significant, and it was concluded that the most immediate problem was to obtain an understanding of the behaviour of the solutions of the linearized equations, and that nonlinear effects were relatively unimportant in most practical cases of interest.

2.2.3 BGK Solutions

It was observed in the previous section that changing the interaction model from hard sphere to Maxwellian collisions had little effect on the results of a given moment solution. Since the collision integral's complexity arises from the detailed description of the collision, if it could be replaced by a simpler operator, which retained only the qualitative and average properties of the full collision operator, the solution would be greatly simplified. Welander (Ref.21) and Bhatnagar, Gross and Krook (BGK) (Ref. 22) independently suggested that since the effect of collisions was to force the distribution function towards a Maxwellian, a reasonable approximation to the collision term would be:

$$I_{coll}(\underline{v}) = \nu[f(\underline{v}) - f_{Max}(\underline{v})] \tag{2.2.45}$$

where ν is a velocity-independent collision frequency. Bassanini, Cercignani and Pagani used this model to solve the linearized heat flux moment equation with unity accommodation (Ref. 6), and later for incomplete accommodation (Ref. 7). As in the previous studies, the distribution function and boundary conditions were taken as:

$$f = f_{Max}(1 + h) \tag{2.2.46}$$

$$h\left(c_x,\ x = -\frac{d}{2}\ \mathrm{sgn}\ c_x \right) = \frac{\Delta T}{T}\,(c^2 + B)\,\mathrm{sgn}\ c_x \tag{2.2.47}$$

with the c's being the nondimensional velocities.
Substitution of this form into the required transfer equation yielded:

$$c_x\ \frac{\partial h}{\partial x} + \frac{h}{\nu} = \frac{1}{\nu}\left\{ \frac{1}{\pi^{3/2}} \int_{\underline{c}_1} e^{-\underline{c}_1^2}\, h(x,\underline{c}_1)\, d\underline{c}_1 \right.$$

$$\left. + \frac{2}{3\pi^{3/2}}\left(\underline{c}^2 - \frac{3}{2} \right) \cdot \int_{\underline{c}_1} \left(\underline{c}_1^2 - \frac{3}{2} \right) e^{-\underline{c}_1^2}\, h(x,\underline{c}_1)\, d\underline{c}_1 \right\} \tag{2.2.48}$$

Two equations incorporating the boundary conditions were solved along with this transfer equation, and the resultant heat transfer rates given.

Two methods of solution were employed; a numerical method and a variational one, and the differences in heat transfer rate between the two were less than 0.5%. This rate curve virtually coincided with that for Gross' and Ziering's eight-moment method. Saraf (Refs. 23,24) and Huang and Hwang (Ref. 25) have also used the BGK model to solve the linear case with nearly identical results.

Willis (Ref. 10) used the BGK model to evaluate the heat transfer at high temperature ratios ($10^{4\pm2}$) and presented some results for 'moderate' ratios (4 and 16). He solved the problem iteratively, using the four lowest moments, for the temperatures and densities between the plates, with an a priori assumption of a bimodal form. The first iteration used the free-molecular values to start, and subsequent iterations began with the result of the previous one. The large temperature ratio results had a peak in the transition regime for the heat transfer rate ($q > q_{FM}$) and the 'moderate' results were similar to the linearized eight-moment results of Gross and Ziering.

2.3 Monte Carlo Methods

The term Monte Carlo applies to methods which utilize statistical sampling procedures in the solution, and consequently covers a variety of approaches.

Perhaps the easiest to visualize is the system devised by Bird (Ref. 20) in which a sample gas containing a few thousand particles is used to directly simulate the behaviour of a real gas. An initial distribution in phase space is set up by randomly choosing each particle's velocity from a Maxwellian. The particles move for a given time (Δt) less than the mean free time, and then the system is stopped and sampling used to choose collision partners from within suitably chosen cells in physical space. When the partners and collision parameters have been selected the post-collision velocities for each particle are stored for use in the next step. A formalism is used to determine how many collisions to study for each step and when this number is reached all collisions cease and the molecules again move with their new velocities for another interval Δt, after which a new set of collisions take place. After a sufficient number of steps, the procedure is stopped and the gas properties are determined. Properties at the boundary, such as pressure, can be inferred from the number of molecules striking that boundary, and their corresponding momenta, during a given time interval.

This method is expensive in terms of computer time, although the reliability and flexibility of minicomputers which can run unattended for extended periods have resulted in its continued usage. No detailed results for the heat transfer problem have been published, but the method was tested using this problem and gave results similar to Lees (Ref. 26).

2.3.1 Test Particle Methods

A method similar to that of Bird, but following the motion of only one particle in a detailed manner, is the test particle method, first used in the solution of the heat transfer problem by Havilland (Refs. 15,16)

and later by Perlmutter (Refs. 18,19) and Tuer (Ref. 17). The solution scheme is based on the property of the distribution function that if the total time of study is long enough, then the portion of that time spent in any given cell of phase space by one gas particle is proportional to the density distribution for the total gas (ergodicity). Thus, if the motion of a single representative molecule can be followed, including an allowance for the effect of collisions, then the distribution function of the total gas can be determined. In order to accurately model collisions, however, the distribution function of the target molecules must be known, and consequently the procedure becomes an iterative one in which the target distribution function is initially chosen by the numerical experimenter, and the time history of the test particle is followed as it moves through this gas. The experimental region is divided into cells in physical space and the initial estimate of the number density distribution is used to fill these cells with the target particles. An initial velocity and position are chosen for the test particle and the mean time to collision is evaluated and compared to the time for the particle to cross the cell. If the collision time is less than the crossing time, a collision partner is randomly chosen from among the molecules in the cell and the after-collision velocity of the test particle is calculated. If the crossing time is less than the collision time, the test particle is either moved into the next cell, or, if the cell boundary is a wall, the particle is reflected with a velocity determined by the surface interaction-model being used. This process is allowed to proceed until a statistically valid sample of test particle positions and velocities has been built up. This distribution function for the test particle then becomes the new target particle distribution and the process is repeated through successive iterations until there is no appreciable change in the distribution function between iterations. This procedure is equivalent to a solution of the modified Boltzmann equation:

$$c_x \frac{\partial f^{(r)}}{\partial x} = \iiint \left(f'^{(r)} f_1'^{(r-1)} - f^{(r)} f_1^{(r-1)} \right) \underline{g}\, b\,db\,d\epsilon\, d\underline{v}_1 \qquad (2.3.1)$$

where r is the iteration number. The equation reduces to the true Boltzmann equation when $f^{(r)} = f^{(r-1)} = f$.

Haviland's results were obtained for both hard sphere and Maxwell molecules with a plate temperature ratio of 4. The hard sphere results were very close to Gross and Ziering's eight-moment method but not Lees' bimodal results. For the Maxwell molecules at a Knudsen number of two, Wang Chang and Uhlenbeck's results were best matched. It was also observed that the nonlinear effects of the large temperature difference were not serious, even when comparing the results to linearized models. Tuer modified the method to make it more efficient, partially by retaining only the moments of the distribution function, and not the distribution function itself. His density distributions best matched Gross and Ziering's eight-moment results, but the normalized heat flux ratio was closest to Haviland's six-moment value. Perlmutter's results for hard sphere molecules were closest to the eight-moment solution in the heat flux and density distribution cases, but there was a large mismatch for the temperature plot at a Knudsen number of two, which resulted from the use of the algebraic mean of the plate temperatures instead of the more physically meaningful geometric mean for T_o, the temperature about which the linearized expansion was performed.

2.3.2 Evaluation of the Collision Integral

A sampling method was devised by Nordsieck (Ref. 27) for direct solution of the Boltzmann equation by numerical integration of the collision integral. Because of the large computer times required to directly numerically evaluate the complete five-fold integral, the velocity space was discretized into 226 cells corresponding to a semi-circular region in the $(v_x, v_\perp)$ plane. Integration over the azimuthal angle ϵ was accomplished by dividing the range $(0, 2\pi)$ into 64 segments. The effect of this $(v_x, v_\perp, \epsilon)$ formulation was to restrict solutions to cases having an axis of symmetry, and the angle ϵ was thus needed only for evaluation of the collision integral, not the presentation of the results.

An initial estimate was made of the distribution function and then the collision integral was evaluated at each of the 226 cells. These values were then used to solve the individual Boltzmann equations for each cell

$$c_x \frac{\partial f(\underline{c},x)}{\partial x} = I_{coll}(\underline{c},x) \qquad (2.3.2)$$

for the new value of $f(\underline{c},x)$.

Integration of the two halves of the distribution function was carried out separately in order to utilize the boundary condition of total accommodation at the walls. The physical space between the plates was divided into stations, and the initial estimate of f at each wall was bimodal. Integration of the collision integrals for positive c_x was carried out at each station moving from the cold to the hot plate, and the opposite direction was used for negative c_x. Once the 226 differential equations at each station had been solved, the two halves of the distribution corresponding to $c_x \gtrless 0$ were scaled to match the no-mass-flow constraint. These new values were then used to re-evaluate the collision integrals as the start of the next iteration. As in the test particle method, iteration ceased when the difference between successive results was sufficiently small.

Yen (Refs. 8,9) used this method to study the heat transfer problem, and compared the results with a numerical solution of the BGK equation and a four-moment bimodal solution. The Monte Carlo results lay between the four-moment and BGK results, exhibiting greater variation in density and temperature between the plates than predicted by the bimodal solution, but not as great as the BGK values. Similarly, the heat transfer rate lay between the two predicted values. Cheremisin has also studied the heat transfer problem using this technique and presented preliminary results (Ref. 14). No detailed comparisons with theory have yet been published, but the problem is currently being investigated in greater depth (Ref. 28).

2.4 Previous Experimental Investigations

2.4.1 Density and Heat Transfer Results

Teagan and Springer and Alofs, Flagan and Springer measured the density distributions between the plates for both small (Ref. 1) and appreciable (Ref. 2) temperature differences. The heat transfer rate was also measured for the small temperature difference case by Teagan and Springer.

The heat transfer rates were measured in argon over an inverse Knudsen number range of 1.3 to 15.2 with a temperature difference of 0.013, and an accommodation coefficient deduced from the measured free-molecular heat transfer rate of 0.829. Density profiles were measured with a $\Delta T/T_o$ value of 0.14 by means of an electron beam fluorescence probe. The results for both parameters were in good agreement with those of Lees' bimodal method and Gross and Ziering's linearized four-moment method but were significantly different from the eight-moment results.

Alofs, Flagan and Springer extended the density measurements to the case of a temperature ratio of four. Their results in helium matched Lees fairly well in the near-continuum regime ($Kn \lesssim 0.12$) but showed a markedly steeper slope in the inter-plate temperature profile at higher Knudsen numbers. The measured free-molecular accommodation coefficient at the 'hot' plate was 0.58, and the 'cold' plate value was estimated to be in the range 0.4 to 0.58. For comparison with theory it was assumed that $\alpha_c = \alpha_h = 0.58$. No comparison of the experimental data with the linearized results of Gross and Ziering was made by the authors, but it is worth noting that the eight-moment solution predicts temperature profiles shaped similarly to the experimental ones and this solution was well matched by Haviland's hard sphere Monte Carlo results for the same temperature ratio as used in the experiments. Cheremisin (Ref. 14) compared his Monte Carlo results for density to theirs and found good agreement.

2.4.2 Distribution Function Measurements

Möller and Adomeit (Ref. 3) measured the Doppler broadening of the 5016Å helium line in order to obtain the shape of the distribution function in the direction perpendicular to plates having a temperature ratio of two, and then computed the lowest order moments to find the density, mean velocity and temperature profiles between the plates. The measured accommodation coefficients were between 0.35 and 0.4, with the result that a strongly bimodal distribution was never obtained, even at high Knudsen numbers near the plates. The only theoretical solutions to which the experimental results were compared were those of Lees, and although the inter-plate profiles were qualitatively similar in form, the actual temperature and density values differed by up to 50%.

2.5 Summary of Results

The moment method solutions break down into two groups, as can be seen in Figs. 2.1.2 and 2.5.1. The heat transfer rates are similar for all the four-moment methods, whether linearized or not, with the eight-moment linearized solution lower by about 10%. The BGK solutions of Willis, Huang and Hwang, and Bassanini, Cercignani and Pagani are all similar to the eight-moment result. The test particle Monte Carlo results of Haviland, Tuer and Perlmutter also favoured the eight-moment method, but Yen's integral evaluation method produced values closer to the four-moment ones.

Most of the previous studies explicitly gave density instead of temperature profiles between the plates, with both the maximum slope and the greatest increase in slope near the plates predicted by the linearized eight-moment method. Again the test-particle Monte Carlo results favoured this solution and Yen's results were between those of Gross and Ziering and the four-moment values.

The only experimental data so far strongly favoured Lees' model in the linearized regime, but was less conclusive in the nonlinear case. Authors who have subsequently developed rigorous BGK solutions which favoured the eight-moment results over Lees' have attributed the discrepancy to the experimental results. Both Huang and Hwang (Ref. 25) and Cercignani (Ref. 55) quote private communications from G. S. Springer stating that the data were reduced assuming that the pressure between the plates was the same as that in the enclosing vacuum chamber, and that this assumption may have been erroneous.

3. EXPERIMENTAL TECHNIQUE

3.1 Analysis of the Molecular Velocity Distribution Function Using the Electron Beam Fluorescence Technique

The nature of the molecular velocity distribution function for a gas can be obtained by analysis of the Doppler broadening of spectral lines in the light emitted by any excited atoms or molecules within that gas, provided that the distribution function for the excited particles is the same as that for the bulk of the gas. In an equilibrium high temperature plasma which is self-luminous this condition is automatically met, but in cooler regimes a method must be found to excite a fraction of the gas particles without appreciably disturbing their translational momentum. It has been known for some time that inelastic collisions between high speed [O(keV)] electrons and gas atoms or molecules result in excitation with either negligible or known modification of translational or internal energy states, and consequently the coupling of an electron beam, to cause fluorescence, with suitable diagnostic optics has been employed in many rarefied gas dynamic studies. Relative composition (Ref. 29), number density (Refs. 30,1,31), translational temperature (Refs. 31,32,33,34,3), and rotational temperature (Ref. 35) are all parameters which have been determined by means of the electron beam fluorescence technique, but all but two (Refs. 3,59) previous studies have been confined to near-equilibrium conditions, where the distribution function was assumed to be either a pure Maxwellian or an ellipsoidal Maxwellian, or to have only minor deviations from this form. In this study the method was extended to the determination of the degree of asymmetry in a high Knudsen number (and consequently nonequilibrium) case.

3.1.1 The Relationship Between the Doppler Profile of a Spectral Line and the Distribution Function

The Doppler profile of a spectral line results from the integrated effect of the individual Doppler shifts of the photons emitted by each particle, and hence directly models the distribution of velocities (along the line of sight) of these particles. When an excited atom decays from an upper energy state to a lower one it emits a photon of wavelength λ_o, the characteristic wavelength for the energy level change. In general, however, an observer receiving this photon perceives it at a different wavelength, λ_1, because of the relative motion between the emitter and observer. Provided that this relative velocity, $\underline{u}$, is much less than the speed of light, the shift $(\lambda_1 - \lambda_o)$ is given by the formula:

$$\frac{\lambda_1 - \lambda_o}{\lambda_o} = - \frac{\underline{u} \cdot \underline{i}}{c} \qquad (3.1.1)$$

where $\underline{i}$ is the unit vector pointing towards the observer. If one now considers a group of emitting atoms, each having its own velocity relative to the observer, then the relationship between the velocity distribution function and line shape becomes apparent. It is simply a one-to-one correlation between the number of photons received at a given shifted wavelength and the number of emitters having the corresponding line-of-sight velocity component, provided that there is no wavelength-selective absorption between the emitter and receiver. Because it is the line-of-sight component of velocity that is being measured, the method yields the distribution function of 'x' components of the molecular velocities, not the actual v_x component of the distribution function. This can be formally represented by the integration over all 'y' and 'z' velocities to yield the measured distribution function,

$$\mathcal{F}(c_x) = \int_{c_y} \int_{c_z} f(c_x, c_y, c_z, \underline{x}) dc_y dc_z \qquad (3.1.2)$$

where the measurement is taking place at position $\underline{x}$. In the case of an ellipsoidal Maxwellian (and its simplest form, the isotropic Maxwellian) distribution function this integration results in a change of scale only, with no alteration of form, and since measurements are actually made of relative intensities, the measured distribution function, $\mathcal{F}(c_x)$, has the same shape as the c_x component of f, as is shown by the following explanation.

The generalized ellipsoidal Maxwellian distribution function is usually represented by two temperatures, one parallel to an axis of symmetry, which in this example is the 'x' axis, and the other perpendicular to it:

$$f = n(\underline{x}) \left(\frac{m}{2\pi k} \right)^{3/2} \frac{1}{T_{\parallel}^{1/2}} e^{\frac{-m(v_x - U_x)^2}{2kT_{\parallel}}} \frac{1}{T_{\perp}} e^{\frac{-m[(v_y - U_y)^2 + (v_z - U_z)^2]}{2kT_{\perp}}} \qquad (3.1.3)$$

where (U_x, U_y, U_z) is the bulk velocity of the gas. Since it is manifested in a shift of the distribution function without alteration of its shape, we replace the actual velocity $(v_x - U_x,\ v_y - U_y,\ v_z - U_z)$ by a new vector (c_x, c_y, c_z) representing only the random (thermal) motion about the bulk velocity and let the effect of this in the wavelength domain be the shift of perceived wavelength from λ_o to λ_o', where $\lambda_o' - \lambda_o = - \underline{U} \cdot \underline{i} / c \times \lambda_o$. Consequently, we rewrite the distribution function as

$$f = n(\underline{x}) \left(\frac{m}{2\pi k} \right)^{3/2} \frac{1}{T_{\parallel}^{1/2}} e^{\frac{-mc_x^2}{2kT_{\parallel}}} \frac{1}{T_{\perp}} e^{\frac{-m(c_y^2 + c_z^2)}{2kT_{\perp}}} \qquad (3.1.4)$$

with the corresponding observed distribution function becoming

$$\mathcal{F}(c_x) = n(\underline{x}) \left(\frac{m}{2\pi k} \right)^{3/2} e^{\frac{-mc_x^2}{2kT_{\parallel}}} \cdot \frac{1}{T_{\parallel}^{1/2}} \frac{1}{T_{\perp}} \int_{c_y=-\infty}^{\infty} \int_{c_z=-\infty}^{\infty} e^{\frac{-mc_y^2}{2kT_{\perp}}} e^{\frac{-mc_z^2}{2kT_{\perp}}} dc_y dc_z \qquad (3.1.5)$$

which becomes, after evaluation of the integrals,

$$n(\underline{x})\sqrt{\frac{m}{2\pi kT_{\parallel}}}\; e^{\frac{-mc_x^2}{2kT_{\parallel}}}$$

Converting to wavelength space with

$$I_o \triangleq n(\underline{x})\sqrt{\frac{m}{2\pi kT_{\parallel}}} \tag{3.1.6}$$

one obtains for the shape of the spectral line:

$$\frac{I(\lambda_1)}{I_o} = e^{\frac{-mc^2}{2kT_{\parallel}}\left(\frac{\lambda_1 - \lambda_o'}{\lambda_o'}\right)^2} \tag{3.1.7}$$

which is Gaussian in form and dependent only on the parallel temperature, with typical half-widths of the order of 0.001 to 0.01Å for spectral lines near 5000Å in room temperature helium and argon. A similar result is obtained for the perpendicular component. If the model solutions for the distribution function being measured in any experiment cannot be expressed in some simple factorable form having the 'shape retention' property described above, then they must be converted to their equivalent integrated form before comparison with the data in the '$\mathcal{F}$' space.

3.1.2 The Electron Beam Fluorescence Probe

The use of an electron beam fluorescence probe to measure localized rarefied gas properties is approximately twenty years old, and well documented. The initial studies were qualitative flow visualizations (Ref. 36) using pictures of flows being scanned by a beam. Calibrations were subsequently performed allowing absolute density and composition measurements from total intensities of individual lines (Ref. 37). Muntz (Ref. 35) extended the method to the measurement of rotational temperatures in nitrogen, and subsequently (Ref. 38) to translational temperatures in helium. Numerous experiments have since been performed not only in helium (Ref. 32,39,40), but also argon (Refs. 31,34) and nitrogen (Refs. 41,42), so that the method is well developed, although some difficulties have arisen with its application to nitrogen (Ref. 42).

The method consists of the passage of a well focused beam of electrons through the region of experimental interest to excite the gas particles by means of inelastic collisions. In order to maintain good spatial resolution, since volumes of interest are usually about 1 mm^3, a high voltage (5 to 20 kV) is required so that wide angle scattering of the electrons before they reach the observation region is minimized. Magnetic lenses are often employed to further focus the beam. In order to maximize the signal level, as high a current as obtainable is used, with typical values ranging between 100 μA and 10 mA.

3.1.3 Additional Sources of Line Broadening

Because the electron density in the primary beam is so low ($< 5 \times 10^{11}$ cm^{-3}) Stark broadening of the spectral line is negligible. However, two additional sources of broadening are present.

The development of the Doppler profile of the spectral line assumed that all photons were emitted at the same wavelength, λ_o. In reality, however, this is not the case, because of the nature of photon emission: transition of an electron within the atom from a higher energy level to a lower one. The Heisenberg uncertainty principle states that there is an a priori uncertainty in the upper and lower energy levels corresponding to the transition, as well as an uncertainty in the occupancy time of each level. This uncertainty is quantified as $\Delta E_{u,l}\ \Delta t_{u,l} \approx \hbar$. Since the wavelength of the emitted photon is given by: $\lambda_o = hc/(E_u - E_l)$, then the uncertainty in E_u and E_l results in a corresponding uncertainty in λ_o, and hence a broadening of the line, as shown below.

Using the wavelength-energy relationship, we have

$$\frac{1}{\lambda_o} = \frac{(E_u - E_l)}{hc} \tag{3.1.8}$$

with the corresponding energy uncertainty being $\Delta(E_u - E_l) = \Delta E_u + \Delta E_l$, which is given by the uncertainty principle as:

$$\Delta(E_u - E_l) = \hbar \left(\frac{1}{\Delta t_u} + \frac{1}{\Delta t_l} \right) \tag{3.1.9}$$

Therefore

$$\Delta \left(\frac{1}{\lambda_o} \right) = \frac{1}{2\pi c} \left(\frac{1}{\Delta t_u} + \frac{1}{\Delta t_l} \right)$$

But

$$\left| \Delta \left(\frac{1}{\lambda_o} \right) \right| = \frac{\Delta \lambda_o}{\lambda_o^2} \qquad \text{for } \Delta\lambda_o \ll \lambda_o \tag{3.1.10}$$

$$\rightarrow |\Delta\lambda_o| = \frac{\lambda_o^2}{2\pi c} \left(\frac{1}{\Delta t_u} + \frac{1}{\Delta t_l} \right) \tag{3.1.11}$$

The inverse time uncertainties are determined by the Einstein A coefficients, so that the wavelength uncertainty is given by:

$$|\Delta\lambda_o| = \frac{\lambda_o^2}{2\pi c} \left(\sum_m A_{mu} + \sum_n A_{nl} \right) \tag{3.1.12}$$

This value is a total-width-at-half-height from which is determined the actual normalized natural shape of the line (Ref. 54):

$$I(\lambda) = (\Delta\lambda_o)^2/4\{(\lambda - \lambda_o)^2 + (\Delta\lambda_o)^2/4\} \qquad (3.1.13)$$

If we represent this 'natural' intensity distribution by I_N and the normalized Doppler distribution by I_D, then the observed line shape becomes $I_D * I_N$, the convolution of the two. The convolution integration arises because the Doppler intensity function behaves like a window of finite width with respect to the natural function. Any given photon observed at wavelength λ_1 may have come from one of many different states which satisfy the condition that a photon having the initial wavelength λ' be emitted by an atom moving at a velocity v' corresponding to a Doppler shift of $\lambda_1 - \lambda'$. It is the convolution integral which sums over all these possible states,

$$I_{OBS}(\lambda_1 - \lambda_o) = \int_{\lambda'=-\infty}^{\infty} I_N(\lambda' - \lambda_o) I_D(\lambda_1 - \lambda')d\lambda' \qquad (3.1.14)$$

The second possible broadening effect is due to momentum transfer both from the excitation process and from scattering of the primary beam electrons which cause the excitation.

We look first at the excitation process itself, without considering the effect of secondary electrons or scattering of the beam electrons. The excitation energy for the 4609Å line is 34.23 eV (5.48×10^{-18} joules) (Ref. 60), a small fraction of the 6 keV in the beam. The initial velocity of the electron is given by:

$$\frac{1}{2} m_e v_e^2 = 6000 \times 1.6 \times 10^{-19} \text{(joules)} \qquad (3.1.15)$$

which yields

$$v_e = 4.59 \times 10^7 \text{ m/s} \qquad (3.1.16)$$

The change in velocity is

$$\Delta v_e = v_e - v_e' \qquad (3.1.17)$$

where

$$\frac{1}{2} m_e(v_e^2 - v_e'^2) = 34.23 \times 1.6 \times 10^{-19} \text{ joules.} \qquad (3.1.18)$$

Since

$$\frac{\Delta v_e}{v_e} \ll 1 \tag{3.1.19}$$

we write

$$\frac{1}{2} m_e (\Delta v_e) 2 v_e = 34.23 \times 1.6 \times 10^{-19} \tag{3.1.19a}$$

which gives

$$\Delta v_e = 1.31 \times 10^5 \text{ m/s}.$$

Using

$$m_A \Delta v_A = m_e \Delta v_e \tag{3.1.20}$$

and

$$\frac{m_e}{m_A} = 1.4 \times 10^{-5} \tag{3.1.21}$$

gives an incremental velocity of the atom of 1.8 m/s, only about 0.4% of its thermal speed, and hence negligible.

We now consider the effect of angular scattering of the primary beam. A 6 keV electron deflected through an angle θ by an inelastic collision picks up a transverse velocity of:

$$v_{transverse} = 4.59 \times 10^7 \sin \theta \text{ m/s}$$

or, if θ is small,

$$v_{transverse} \approx 4.59 \times 10^7 \theta \text{ m/s} \tag{3.1.22}$$

and the resultant recoil velocity of the argon atom is:

$$v_{A_{recoil}} = 4.59 \times 10^7 \times 1.4 \times 10^{-5} \theta \text{ m/s}$$

$$= 643\theta \text{ m/s} \tag{3.1.22a}$$

The distribution of recoil velocities can now be calculated from the angular distributions of the scattered electrons. If the differential scattering cross-section is $\sigma(\theta)$ then the number of electrons scattered into a solid angle $d\Omega$ at azimuthal angle φ is $\sigma(\theta)d\Omega$, where

$$d\Omega = v_e \sin\theta d\theta d\varphi . \tag{3.1.23}$$

Therefore

$$dn(\theta,\varphi) = v_e \sin\theta\sigma(\theta)d\theta d\varphi \tag{3.1.24}$$

or, for $\theta \ll 1$

$$dn(\theta,\varphi) = v_e \theta\sigma(\theta)d\theta d\varphi \tag{3.1.25}$$

The observed distribution function for recoil velocities is $\int dn(v_x,v_y)dv_y$ so we convert from (θ,φ) coordinates to (v_x,v_y) coordinates by:

$$d\frac{v_x}{v_e}\, d\frac{v_y}{v_e} = \theta d\theta d\varphi \tag{3.1.26}$$

and

$$\theta = \sqrt{\frac{v_x^2}{v_e^2} + \frac{v_y^2}{v_e^2}} \tag{3.1.27}$$

We now obtain for the observed recoil velocity distribution

$$dn\left(\frac{v_x}{v_e}\right) = \int_{\text{all } v_y} \sigma\left[\theta\left(\frac{v_x}{v_e}, \frac{v_y}{v_e}\right)\right] d\frac{v_x}{v_e}\, d\frac{v_y}{v_e} \tag{3.1.28}$$

For purposes of estimation of the velocity distribution a reasonable value of the differential cross-section, given by (Ref. 61):

$$\sigma(\theta) = \text{constant}/\theta \qquad \text{for } \theta_2 < \theta < \theta_3 \tag{3.1.29}$$

$$\approx 0 \text{ elsewhere}$$

was used, where

$$\theta_2 = \frac{\Delta E_{\text{excitation}}}{2E_{\text{electron}}} \tag{3.1.30}$$

$$= 2.83 \times 10^{-3} \qquad \text{for our case,}$$

and

$$\theta_3 = \sqrt{\frac{|E_{\text{ground state}}|}{E_{\text{electron}}}} \qquad (3.1.31)$$

$$= .0847 \qquad \text{for our case.}$$

The distribution is thus:

$$dn\left(\frac{v_x}{v_e}\right) = \text{const} \int_{v_{y_{\text{cut-off}}}^{\text{min}}}^{v_{y_{\text{cut-off}}}^{\text{max}}} \frac{d\,\frac{v_y}{v_e}}{\sqrt{\frac{v_x^2}{v_e^2} + \frac{v_y^2}{v_e^2}}} \qquad (3.1.32)$$

where

$$v_{y_{\text{cut-off}}^{\text{min}}} = v_e \sqrt{(2.83 \times 10^{-3})^2 - \frac{v_x^2}{v_e^2}} \qquad \text{for } \left|\frac{v_x}{v_e}\right| \leq 2.83 \times 10^{-3} \qquad (3.1.33)$$

$$= 0 \text{ elsewhere}$$

and

$$v_{y_{\text{cut-off}}^{\text{max}}} = v_e \sqrt{(.0847)^2 - \frac{v_x^2}{v_e^2}} \qquad \text{for } \left|\frac{v_x}{v_e}\right| \leq 0.0847 \qquad (3.1.34)$$

$$= 0 \text{ elsewhere.}$$

Evaluation of the integral yields

$$dn\left(\frac{v_x}{v_e}\right) = \ln\left[\frac{v_{y_{\text{cut-off}}^{\text{max}}}}{v_e} + .0847\right]$$

$$- \ln\left[\frac{v_{y_{\text{cut-off}}^{\text{min}}}}{v_e} + \sqrt{\left(\frac{v_{y_{\text{cut-off}}^{\text{min}}}}{v_e}\right)^2 + \left(\frac{v_x}{v_e}\right)^2}\right] \qquad (3.1.35)$$

which has a peak near 0.17 degrees and a half-width of 1.3°, corresponding to a transverse velocity of the electron of 1.04×10^6 m/s. The approximation used in the calculation, $\sigma(\theta) = 0$ for $\theta < \theta_2$, was a conservative one. In reality the differential cross-sections increase above their values at θ_2 as the scattering angle approaches zero, although the form of the function can no longer be approximated by $\sigma(\theta) \propto \theta^{-1}$. Consequently, the true peak in the observed distribution of recoil velocities would be at 0°, not 0.17°, and thus the half-width would be even lower. Using the conservative estimate of the electron scattering distribution, we obtain a half-width of the atom velocity distribution of 15 m/s, corresponding to a wavelength shift of 2×10^{-4} Å. This width is of the same order of the natural

width, and only 3% of the thermal width. Because it is a small fraction of the thermal width its broadening effect is proportional to the square of the width, and is thus only of the order of 10^{-3} of the thermal width, which is a negligible increase.

The third perturbation effect is the ejection of a secondary electron during the excitation collision. The spectral line used in this experiment was an ionic one, and hence a secondary electron was produced for every photon observed. The secondaries are emitted isotropically, and with an energy distribution peaking near 1 eV and dropping off rapidly, with a half-width of less than 2 eV, corresponding to an atomic recoil velocity of:

$$v_{A_{recoil}} = 1.4 \times 10^{-5} \times \sqrt{\frac{2 \times 2 \times 1.6 \times 10^{-19}}{9.1 \times 10^{-31}}} \qquad (3.1.36)$$

$$= 12 \text{ m/s}$$

This also represents a perturbation of only 3% of the thermal speed, which is reflected in a negligible increase in the observed line width.

It is thus seen that collisions with primary and secondary electrons do perturb the momenta of the gas atoms, but, because the perturbations are much smaller than the thermal speed, they have a negligible broadening effect on the observed convoluted distribution, and can be ignored, as has been done in all previous studies in argon (Refs. 31,34,59).

3.2 Spectral Analysis Technique

The narrowness of the spectral lines being studied places a resolution requirement on the spectrometer of at least 10^6, two orders of magnitude greater than obtainable with conventional grating type instruments. The Fabry-Perot interferometer, however, is capable of a resolution of 10^7 or better with high transmission efficiency, and consequently is an ideal instrument for this type of study. Its operation has been well documented (Refs. 43,44,45) and only a summary is presented.

3.2.1 The Ideal Fabry-Perot Interferometer

The ideal interferometer, as shown in Fig. 3.2.1(a) consists of two perfectly flat, thin parallel plates separated by a distance h, and having reflective coatings on their facing surfaces. The index of refraction of the medium surrounding the plates is n. A plane parallel wave of monochromatic light of amplitude A and wavelength λ, corresponding to angular frequency $\omega(=2\pi c/\lambda)$ is projected towards the plates at an angle θ. Each surface transmits a fraction t of the wave and reflects r, so that a series of beams emerge at θ, separated by a distance of $2nh\sin\theta$. The phase difference (ignoring phase changes at reflecting surfaces) between any two beams at the same wave-front is 2π times the path length difference divided by the wavelength, i.e.,

$$2\pi(PR + RS - PQ)/\lambda \qquad (3.2.1a)$$

$$= 2\pi\left(\frac{2nh}{\cos\theta} - 2nh\tan\theta\sin\theta\right)\Big/\lambda \qquad (3.2.1b)$$

$$= 2\pi\left(\frac{2nh}{\lambda}\cos\theta\right) \qquad (3.2.1c)$$

The factor in brackets represents the difference in the number of waves between adjacent beams at the same wavefront, and is the order number of the instrument (p), typically about 10^5. The effect of a phase change of amount ψ at each reflection is to change the effective path length by an amount $2\psi/2\pi < 1$, and hence negligible with respect to 10^5, but still significant in that integral order numbers correspond to constructive interference (same phase of all waves in the front). Consequently, the criterion for constructive interference is that $(2nh/\lambda)\cos\theta + \psi/\pi$ be integral. Since the intensity of the wave is of more experimental interest than the amplitude, we replace t and r by their more useful counterparts T(=tt) and R(=rr), the intensity transmission and reflection coefficients, respectively. It is seen from the figure that the bundle of rays leaving at angle θ consists of the sum of the individual contributions:

$$\begin{aligned} & AT\, e^{i(\omega\tau-\pi p)}[1 + R\, e^{-i2\pi p} + R^2\, e^{-i4\pi p} + \ldots] \\ &= AT\, e^{i(\omega\tau-\pi p)}/(1 - R\, e^{-i2\pi p}) \\ &= B\, e^{i\omega\tau} \end{aligned} \qquad (3.2.2)$$

where B is the amplitude of the wave. The intensity of the beam is therefore $B \cdot B^*$

$$\begin{aligned} &= A^2T^2/(1 - R[e^{i2\pi p} + e^{-i2\pi p}] + R^2) \\ &= A^2T^2/[1 + R^2 - 2R\cos(2\pi p)] \\ &= A^2T^2/[(1 - R)^2 + 4R\sin^2(\pi p)] \\ &= \frac{A^2T^2}{(1-R)^2} \cdot \frac{1}{1 + \frac{4R}{(1-R)^2}\sin^2(\pi p)} \end{aligned} \qquad (3.2.3)$$

But the intensity of the incoming beam was A^2, so the intensity transmission function of the instrument becomes:

$$\frac{T^2}{(1-R)^2} \cdot \frac{1}{1 + \frac{4R}{(1-R)^2}\sin^2(\pi p)} \qquad (3.2.3a)$$

which is usually expressed in normalized form by removing the first term. The repetitive nature of this Airy function is evident in the $\sin^2(\pi p)$ term, with the function having a maximum at integral values of p and a minimum of $[1 + 4R/(1-R)^2]^{-1}$ at the mid-points. Since $p = (2nh/\lambda)\cos\theta$, the intensity of a given wavelength goes through successive maxima and minima as θ increases from zero to the limiting angle of the instrument. Because of the symmetry of the instrument about the axis perpendicular to the plates, this intensity distribution is manifested by a circular ring

pattern at infinity. In actual usage this pattern is focused onto a screen. Near the axis the expansion of $\cos\theta$ in terms of the radial distance from the centre, r, and the focal length of the focusing lens, f, yields an order distribution of:

$$p(r,\lambda) = \frac{2nh}{\lambda}\left(1 - \frac{r^2}{2f^2}\right) \qquad (3.2.4)$$

The sharpness of the peaks and the contrast ratio (I_{max}/I_{min}) are both increased by an increase in reflectivity, as is shown in Fig. 3.2.1(b). The measure of this sharpness is the reflectivity finesse (F_R), the ratio of the free spectral range to the total-width-at-half-height of the profile, and it has a value of $\pi\sqrt{R}/(1-R)$.

If the incoming light is not purely monochromatic, but consists instead of a distribution of wavelengths over some finite interval, then for any angle θ at which there is an integral order p_1 for a specific wavelength λ_1, then there is also a wavelength λ_2 at which the order number, p_2, is also integral and differs from p_1 by unity. This wavelength difference between successive maxima is a parameter of prime importance known as the free spectral range of the instrument, $< \Delta\lambda >$. Its value is determined from:

$$p = \frac{2nh}{\lambda}\cos\theta$$

Therefore

$$|\Delta p| = 1 \rightarrow 2nh\cos\theta\left(\Delta\frac{1}{\lambda}\right) = 1$$

$$\rightarrow 2nh\cos\theta\frac{< \Delta\lambda >}{\lambda^2} = 1 \quad (< \Delta\lambda > \ll \lambda)$$

or

$$< \Delta\lambda > = \frac{\lambda^2}{2nh\cos\theta} \qquad (3.2.5)$$

which for paraxial rays reduces to

$$< \Delta\lambda > = \frac{\lambda^2}{2nh} \qquad (3.2.5a)$$

Its significance becomes apparent from the realization that the peak sharpness is a function only of fractional order, and hence the instrument function becomes narrower in the wavelength domain as the free spectral range decreases. This implies that lowering the free spectral range would improve the interferometer's ability to monitor the Doppler shape of a spectral line by reducing the smearing effect of the finite bandpass of the instrument. This is valid, but only to the point at which the free spectral range becomes a few Doppler widths. Below that value ambiguity results from adjacent peaks transmitting light from both wings of the line simultaneously.

The actual usage of the instrument requires the scanning of a transmission peak across the spectral line, and monitoring the intensity versus wavelength profile. In practice this is accomplished by setting up the instrument so that light in one wing of the desired line constructively interferes on-axis with order number p_*. A pinhole is placed in the screen at the centre of the ring pattern, so that this light passes through to some form of intensity monitor. The wavelength of the light passing through the hole is then changed, by varying the optical path between the plates in one of two ways.

Rearranging the order number equation yields:

$$\lambda(r = 0,\ p_*) = \frac{2nh}{p_*} \qquad (3.2.6)$$

so that changing either n, the index of refraction of the medium between the plates, or h, the plate spacing, will alter the transmitted wavelength. Since the index of refraction of a gas is, to first order, a linear function of density, one can accomplish the scan by placing the interferometer in a sealed vessel, rigidly mounting the plates at a fixed spacing, and varying the gas density. By monitoring the intensity of the collected light as the density varies one can build up a profile of the line. Because the most common method of density variation is a pressure change at constant temperature, instruments operating in this mode are known as pressure-scanned interferometers. A second type is the piezo-electric scanned interferometer, in which the density is strictly controlled, and one plate is mounted on three piezo-electric stacks. By varying the voltage applied to the stacks this plate can be accurately moved, and hence the spacing changed, so that a profile is built up in a similar fashion as with the pressure scanned instrument. Once the pressure or spacing is changed by an amount equivalent to a scan of one free spectral range the entire profile repeats at order $p_* \pm 1$, so that by knowing the value of the free spectral range one can readily calibrate the scan wavelength versus gas density or piezo-stack voltage.

If the normalized interferometer function is represented by I_R, then the signal seen by the light collector is the 'observed' intensity profile previously described convoluted with this intensity profile:

$$I_N * I_D * I_R$$

3.2.2 Additional Effects With Real Fabry-Perot Interferometers

The derivation of the transmission function, I_R, used the fact that $R + T = 1$, so that the first term $T^2/(1-R)^2$ was automatically unity. In reality the reflective coatings and plates on which they are mounted absorb a fraction A of the light, so that 1-R becomes A+T and the transmitted intensity is

$$\frac{T^2}{(A + T)^2} = \frac{1}{\left(1 + \frac{A}{T}\right)^2} \qquad (3.2.7)$$

Since the absorption is typically about .2 to .5%, then a transmission of 5% would result in a loss of 8 to 17% of the incoming intensity, and lower transmissions would result in even greater losses. Consequently, an upper limit is placed on usable reflectivities at 90 to 94%, which results in reflectivity finesse limits of 30 to 50. The free spectral range of the instrument is usually chosen large enough to allow the intensity in the wings of the distribution function to fall to a few percent of its peak value, but not so large that the instrument half-width becomes a significant fraction of the Doppler half-width. A suitable compromise is to make the free spectral range three to five Doppler widths, so that the instrument width is only about 10% of the Doppler width.

The pinhole is also a broadening factor, since it passes light having a finite wavelength spread. Its transmission function is square, transmitting over a range Δp determined by the radius of the aperture in the following way:

$$p(r) = \frac{2nh}{\lambda}\left(1 - \frac{r^2}{2f^2}\right)$$

$$p(o) = \frac{2nh}{\lambda}$$

Therefore

$$\Delta p = \frac{2nh}{\lambda}\,\frac{r^2}{2f^2} \qquad (3.2.8)$$

which corresponds to a finesse of $1/\Delta p$

$$F_P = \frac{f^2\lambda}{r^2 nh} \qquad (3.2.9)$$

In order to collect as much light as possible, r must be large, and consequently a trade-off is required between signal level and finesse. A reasonable compromise is a value comparable to the reflectivity finesse, so that $F_P \approx 40$. There is now another broadening function to be considered in the signal, so that the received intensity distribution becomes the convolution: $I_N * I_D * I_R * I_P$.

The final broadening effect of the real instrument results from imperfections in the reflecting surfaces. These imperfections take two basic forms: curvature and microscopic surface imperfections. The curvature defect is treated as if the plates were spherically concave with a common radius of curvature, with the result that the spacing between the edges is less than that on axis (Ref. 45). Consequently, the wavelength of order $p*$ at the edges is less than that for the corresponding order at the centre, with a smooth transition between the two as a function of plate position. The broadening function for this defect is thus square with a width corresponding to the wavelength difference between the centre and edge, which in most real systems is negligible. The microscopic imperfections are usually represented as being random with a Gaussian distribution having a characteristic height of λ/m, where m is typically 100 or 200. This variation of spacing from point-to-point on the plates also has a broadening effect on the line with intensity distribution I_I and a corresponding finesse of m/2. Its value is in the same range as the reflectivity finesse so that the defects must also be included in the overall instrument function, yielding a net observed intensity distribution of $I_N * I_D * I_R * I_P * I_I$.

In principle all of the intensity functions except the Doppler one are known or specified, so that the distribution function component of the signal can be separated out with great accuracy. In reality two other effects lower the retrievable accuracy.

Both forms of Fabry-Perot interferometer are susceptible to plate mounting distortions. In the pressure scanned instrument, springs are used to force the plates against the spacers, and localized distortions, resulting in lower finesse, may occur if the design is not carefully considered. The instrument used in the experiment described in this report was found to have a lower finesse than would be expected from its quoted specifications, and was consequently assumed to suffer from this form of distortion. The correctness of the assumption was confirmed by measuring the finesse using only the central portion of the interferometer plates, as described in Appendix A, and its broadening effect was represented by lowering the effective reflectivity of the plates in the calculation of the Airy function. Different forms of distortion were assumed and their effects on the measured profiles evaluated, and it was found that this model was the most conservative in its differentiation between theories (see Section A.3). The piezo-electric scanner has the moveable plate mounted on cantilevered piezo-electric stacks, so that while the plates are not distorted, they are susceptible to vibration, especially immediately after the spacing is stepped during a scan.

The limiting accuracy for the system results from the total intensity of the light being observed. Photon emission follows Poisson statistics, so that there is an uncertainty built into every measurement. If a series of observations were to be made of the total intensity of the light emitted from a specific region of the electron beam by counting the number of photons received in a given time interval, it would be found that for an average photon count of N, the individual counts would vary about N with a standard deviation of $\sqrt{N}$. Consequently, if the experimental intensities are such that the count levels are in the range ~ 3,000 to 10,000, the uncertainties in the signals are 1 to 2%. This 'scatter' in the data causes a resultant uncertainty of a few percent in the measurement of the Doppler widths of the lines, which can only be reduced by increasing experimental count times considerably.

4. EXPERIMENTAL FACILITY

4.1 The UTIAS Low Density Plasma Tunnel

The vacuum facility has been previously described (Refs. 30,46), and only a summary of its layout and the specifics of its usage for this experiment are given. A schematic of the facility is shown in Fig. 4.1.1. The Low Density Plasma Tunnel has a test section in the form of a mild steel horizontal cylinder approximately 2.5m in diameter and 3m long joined to a vertical settling tank 2.5m high and 2m in diameter. Mounted in the test section are two traversing rigs, a 'lower' one having a platform 50 cm square which has motions of ± 75 cm on either side of the tunnel centre line and 1m in the axial direction, and an 'upper' one which has both horizontal motions as well as a third in the vertical direction. All motion drives are 110 VAC synchronous motors mounted outside the tunnel so they can be operated with a plasma in the test section. The blank-off pressure of 1×10^{-5} torr is obtained by means of a liquid nitrogen cold-trapped 4200 l/s diffusion pump backed by a 23 l/s mechanical pump. As well as this 'holding' pump combination, there is provision for using the high mass-flow

capability of the oil vapour booster pumps attached to the Low Density Wind Tunnel. The two tunnels are joined by a 6m long 60 cm diameter tube and can be isolated by a butterfly valve at the Wind Tunnel end of the tube. The throughput mismatch of the two holding pumps prevented operation in the 10^{-2} torr range, so that experimental runs were performed using the 60 cm connecting tube and two of the nine oil vapour booster pumps on the UTIAS Low Density Wind Tunnel, with a net pumping speed at the test section of 1000 l/s. Backstreaming of pump oil and any other condensable contaminants originating in the LDWT was minimized by the installation of an optically-tight water cooled baffle in the connecting line. Stable pressures were maintained by matching the bleed rate of the test gas into the tunnel to the pumping rate. A bottle regulator and choked needle valve were used and the pressure was monitored with a nude Bayert-Alpert ionization gauge. The gauge was calibrated against a cold trapped McLeod gauge at various times and found to have good repeatability.

The electron gun, its pumping system, and the collecting lens for the emitted light were mounted on the lower x-y traversing platform as shown in Fig. 4.1.2, with all components except the lens mount being rigidly attached. The lens mount was rigidly attached to the tunnel itself and mounted on guide rails on the traversing table, so that motion of the table moved the electron beam, but not the lens, to allow for realignment of the beam after a filament change. Two mirrors deflected the collected light to a window in the tunnel wall, outside of which was mounted the main optical system which is described in Section 4.4. The upper x-y-z traversing system held the parallel plate rig, which itself had motion capability.

Standard mounting ports were used for electrical, water cooling, and gas feedthroughs for all systems. The controls interlocked each subsystem for fail-safe operation in the event of a power or water failure to the building or breakdown of any component. An exterior view of the tunnel and its controls is shown in Fig. 4.1.3.

4.2 Parallel Plate Rig

Two 15 cm diameter copper plates, one heated by a 550W ring heater, and the other water cooled, were mounted on their own x-θ traversing rig as shown in Fig. 4.2.1. The lower plate had a sapphire window to allow passage of the fluorescence to the collecting lens. Three lava spacers separated the plates with minimum conductive heat transfer, and allowed variation of spacing from 0.5 to 3 cm. The Knudsen number was determined by the plate spacing and gas pressure. In order to test whether plate end effects were significant, different combinations of plate spacing and tunnel pressure were used to achieve any given Knudsen number, and the results for different plate aspect ratios (diameter/spacing) were compared. Thermocouples were mounted at various positions in each plate to monitor the temperature. In order to check the uniformity of the hot plate temperature a second set of thermocouples was temporarily mounted on the surface facing the cold plate and a series of temperature distribution measurements was made at different gas pressures in the range used in the experiment, and it was found that the temperature was uniform to within 2°K between the centre of the plate and the edge. The cold plate was rigidly attached to the hot plate by the lava spacers, and the hot plate itself was mounted on a rod which was motor driven so that the position of the electron beam between the plates could be varied by moving the plates as a unit while keeping the electron beam fixed in space. The plate position

was monitored by means of a potentiometer encoder, and a water-cooled shield protected the drive from over-heating. A second drive system rotated the plates about an axis parallel to the electron beam. This motion was used to align the 'plate-fixed' coordinates with the optical axis of the measuring system to ensure that the measured intensity profile was representative of the c_x component of the distribution function. Both plates were grounded to prevent charge buildup from scattered beam electrons.

The window was made of sapphire to minimize the temperature difference between it and the rest of the cold plate. Calculations showed that near infra-red black body radiation from the hot plate could create a heat load comparable to that by conduction, so that an efficient infra-red transmitter would tend to heat up less. Sapphire is not only one of the easiest infra-red optical materials to handle but also has one of the highest thermal conductivities, so that it would best conduct away the heat at a low temperature difference. Measurements using thermocouples mounted on both sides of the window were made to check the magnitude of the temperature rise, and it was found that even under secondary electron bombardment from the beam, as well as pure heat transfer, the temperature was within two degrees of the plate. Because the window was an insulator, scattered beam electrons which struck it would not be conducted away and a negative charge would build up, which would then deflect the electron beam towards the hot plate. Consequently a 90% clear, 12.7μ tungsten mesh was mounted on the beam side of the window to provide a conducting surface to ground. The only difficulty with the sapphire was its broad-band fluorescence as a result of secondary electron impact, which caused an increase of about 30% in the background light level above that already existing from the argon. A schematic of the plate mounting is shown in Fig. 4.2.2.

The temperature of the hot plate was regulated by means of the proportional controller shown in Fig. 4.2.3, with the sensing element being a Fenwal GA62J1 thermistor bead mounted in a hole in the centre of the hot plate, where it was both near the front surface and far enough away from the heater to be monitoring the equilibrium front-surface temperature of the plate. Repeatability and stability were within 1°, the accuracy of the monitoring system.

4.3 Electron Gun and Controls

The electron gun used in this study was a modified version of one used previously for upper atmospheric rocket flights (Ref. 47). It had a nominal perveance of $.1 \times 10^{-6}$ $AV^{-3/2}$ and was operated at 6 to 8 kV, with 9 mA emission at a beam half-angle of 6.5°. It was housed in a separate chamber within the Low Density Plasma Tunnel and was pumped by a 25 l/s diffusion pump backed by a 0.8 l/s mechanical pump. A magnetic lens focused the beam onto the 2 mm diameter exit aperture of the gun chamber, and after emerging a second lens focused it on the axis between the plates. A pneumatically actuated door isolated the gun from the tunnel when not in use so that cleanliness was maintained, even with the tunnel vented. The blank-off pressure was 5×10^{-6} torr, and the maximum operating pressure inside the gun chamber was 6×10^{-4} torr at a tunnel pressure of 20μ Hg. The beam was collected by a trap made of a stack of razor blades mounted with the sharp edges facing the beam, as shown in Fig. 4.3.1. The current collected by the beam trap was monitored and compared with the current emitted from the filament as a measure of the efficiency of the gun system. Electrons can be lost from the initial emitted beam either by being poorly focused by the magnetic lenses, or by being scattered out of the beam by collisions with gas particles. The efficiency

varied from over 90% at low tunnel pressures (< 1μ Hg) to 55% at 20μ Hg tunnel pressure, indicating that scattering losses were the dominant factor.

Button filaments made from .010" tungsten were run at a temperature of 2200 to 2400°C with lifetimes between 50 and 150 hours. The leads to the filament were passed to the gun through atmospheric pressure lines to prevent arcing. A cross-section schematic of the gun and pumping system is shown in Fig. 4.3.1, and the assembly is visible in Fig. 4.1.2.

Because of the long count times employed, and the low signal levels, stability of the electron beam was critical. This was primarily because the dark current in the photomultiplier tubes was approximately half the signal current. If the electron beam current were to drop 10%, the count rates in the photomultiplier tubes would drop by only about 6 or 7%, because the dark current was constant. Consequently, the ratio of signal to noise in the tube output would also drop. If the gun current variations were systematic, such as constant increases or decreases, then their effects could be subtracted out in the data analysis, but if they were random there would be no way of separating them from the signal, and hence the emission current was regulated to better than 1% by the circuit shown in Fig. 4.3.2. The magnetic lens control circuits are shown in Fig. 4.3.3.

4.4 Optical System

4.4.1 Selection of the Spectral Line

The emission line chosen was the 4609.6Å line corresponding to the AII transition ($4s'\ ^2D - 4p'\ ^2F^\circ$). It is the conventionally used argon line because it is one of the brighter ones and exhibits no apparent hyper-fine structure. The upper energy level is directly excited and decays rapidly. The Einstein A coefficient for the 4609Å transition is $9.06 \times 10^7\ s^{-1}$ (Ref. 48), and since it is the only strong optical transition originating from either of the two levels, the half-width of the line, $\Delta\lambda_D$, is 1.025×10^{-4}Å and the natural shape function is $I_N = 2.63 \times 10^{-9}/[(\lambda - \lambda_o)^2 + 2.63 \times 10^{-9}]$. At 300°K the Doppler width of the line is 9×10^{-3}Å, so that the natural width, while not negligible, is only a small fraction of the total.

4.4.2 The Optical System and Counting Circuitry

A schematic of the entire system is shown in Fig. 4.4.1, and a photograph of the portion outside the tunnel is presented in Fig. 4.4.2. Light from the emission region was collected and collimated by a 40 mm diameter f/4 lens, and the collimated beam was then deflected by two mirrors through a window in the tunnel wall. An interference filter having a peak transmission of 61% at 4609Å and a total width-at-half-height of 12.3Å then selected the line of interest. The filter width was a compromise between efficient transmission of the desired line and screening of background radiation. A narrower filter would pass less continuum radiation, if that existed, but would have a lower peak transmission, and would consequently necessitate longer experimental runs to collect data with the same statistical accuracy. The spatial resolution was achieved by focusing the light onto a 0.3 mm diameter pinhole by a 250 mm focal length lens. The rediverging beam passed through a beamsplitter which diverted a portion of the light through a lens which refocused it onto the photocathode of a photomultiplier tube. The output from this 'monitor' tube was used to normalize the signal from the photomultiplier which received the light after it was processed by the interferometer.

The main portion of the beam was recollimated and passed through the pressure vessel containing the Fabry-Perot etalon. A final lens focused the ring pattern onto a screen having a hole matching that in the first mask and behind which was a second photomultiplier tube. The net finesse of the system was 10.7, and a detailed calculation is given in Appendix A.

The light levels were measured by a pulse counter operating in the ratio mode. The 'denominator' or gating signal was the amplified output of the monitor photomultiplier tube, and the 'numerator' signal was that from the tube behind the screen. Both tubes were EMI9502S/A, selected for low dark current at high gain. They were water cooled and had dark pulse counts 1 and 6 s^{-1} for the 'count' and 'monitor' tubes respectively. The pulse amplifiers were identical to those used by Payne (Ref. 30).

The etalon holder was made to accept 1.5" diameter plates by Industrial Optics. It has a series of quartz spacers of thicknesses ranging from 0.5 to 3 cm, the latter being used for most experiments. The plates were made by Perkin-Elmer and the quoted reflectivity was 91% at 4609Å. Flatness over the clear aperture (80% of total) was $\lambda/100$, the anti-ghosting wedge angle was 30' and absorption losses were $< 0.2\%$. As mentioned in Section 3.2.2, the mounting springs distorted the plates, so that the net instrument finesse was lower than would be expected from these specifications. A picture of the etalon is shown in Fig. 4.4.3. The pressure vessel windows were tilted to prevent ghosting, and the outer wall was of double construction with circulating constant temperature water within. After alignment of the etalon the chamber was sealed and then evacuated before filling to 2250 torr with helium. The pressure scanning was accomplished by setting a pressure in the etalon vessel and measuring the 'signal' count for a given total 'monitor' count, typically 10^4. The pressure was then stepped by a small amount, 1 to 5 torr, and another count determined. This process was repeated through two free-spectral ranges to build up the line profile. Both before and after the traces were made the signal tube was blanked off and the dark current measured. As mentioned in Section 3.1.3, even when this value was subtracted out, the wing intensity never dropped to its theoretical minimum, so that some other source of background light must have been present.

5. ANALYTICAL METHOD

It was shown in Section 3 that the observed intensity profile was the convolution of five functions: $I_{OBS} = I_N * I_D * I_R * I_I * I_P$, with only the Doppler function containing parameters of experimental interest, the others being composed of known or calculable parameters. These instrumental parameters are chosen in such a way as to make the net instrument profile ($I_N * I_R * I_I * I_P$) as narrow as possible in order to minimize its broadening effect on the Doppler profile.

In general, one fits an n-parameter model $M(P_1,\ldots P_n,x)$ to experimental data $y(x)$ by solving the system of n equations given by

$$\frac{\partial}{\partial P_i} \left\{ \sum_{j=1}^{N} [y(x_j) - M(P_1,\ldots,P_n,x_j)]^2 \right\} = 0 \qquad (5.1)$$

In cases where the model contains convolution integrals, the partial derivatives also contain convolutions, which in general may not have analytic solutions. Consequently, some other method of determining the 'best fit' values of the n parameters must be found. One such method is an iterative search procedure, in which reasonable values of the parameters are chosen, and the convolution integrations performed numerically at points corresponding to the experimental data observations $y(x_j)$ to yield the set of fit points $M(P_1,\ldots P_n,x_j)$. These two sets are then compared, and the 'quality of the fit' evaluated. Some or all of the parameters are then altered and the process repeated until the fit is judged to be the 'best'.

One form of this method that has been used to fit Maxwellian profiles to experimental data obtained in helium was the plotting of the experimental points $y(x_j)$, and the 'fit' points, $M(x_j)$ on the same set of axes for visual comparison (Refs. 32,40). A second plot of the difference between the two $[y(x_j) - M(x_j)]$, and the expected standard deviations $[\pm 3\sigma(x_j)]$ was also presented. The initial steps in the data reduction performed three operations on the raw signal. They subtracted out the dark current in the measuring photomultiplier tube with the result that the ratio of minimum intensity (at centre $\pm$ 1/2 order) to the maximum level (at the centre) matched its expected value, and then normalized all signals by the maximum count. The position of the centre, or zero random velocity point, was also found to great accuracy by searching for the axis of symmetry of the curve. Once these operations had been performed on the experimental points, only one adjustable parameter remained in the fitting function: temperature, so that the model function was simply $M(T,x_j)$. The 'fit' value of the temperature was obtained by trial and error adjustment until it was judged from observation of the two sets of graphs that the match was best.

In contrast to that simple one-parameter temperature fit, in this experiment there were four parameters relating to the measurement itself, as well as those determined by the model being fitted; two were related to the signal level itself (the ordinate) and two were related to the wavelength scale (the abscissa). It was mentioned earlier that the intensity of the high speed wings of the distribution function was greater than expected. This was manifested by an apparent shift of the baseline (or 'zero intensity') light level. After subtraction of photomultiplier dark current from the signals, the minimum to maximum ratio was still greater than expected, so that the actual observed intensity was:

$$I_{OBS} = I_N * I_D * I_R * I_I * I_P + I_{baseline}$$

Because this baseline was indeterminate, so was the maximum count level (or height of the curve) by which all other signals would be normalized. Consequently, the fitting model had to include these two intensity scaling parameters as fit parameters.

The first of the abscissa parameters was the zero random velocity wavelength. Because this study involved asymmetric distribution functions, no simple method of zero velocity determination, such as that used for Maxwellians, could be applied. Since there is a strong relationship between the best fit values of parameters defining the degree of asymmetry of the distributions and the position of the zero velocity axis of the fit curve relative to that of the experimental data, it was necessary to make the position of the zero velocity wavelength, λ_o, a fit parameter. The second abscissa parameter was the conversion of the etalon chamber pressure to a wavelength scale, $\Delta\lambda/\Delta P_{\text{etalon chamber}}$.

In the case of a piezoelectrically scanned interferometer the plate displacement vs voltage characteristic is both measurable and repeatable, but in the case of a pressure scanned instrument the calibration can vary as a result of two factors, the first of which is variation in the temperature of the etalon chamber. Although the etalon vessel cooling water temperature was constant over short periods (days) it varied on a time scale of months, and consequently so did the temperature within the chamber, causing a slight variation in the gas density change for a given pressure change. The second effect was that of non-uniform gas composition between chamber fillings. After the chamber was resealed following a realignment of the instrument it was evacuated. The line from the helium bottle was purged up to the last connection before the inlet valve, and then the chamber itself was filled with the helium. In principle this should have guaranteed almost pure helium in the vessel, but it was noted that, although constant for all runs on one filling, the wavelength/pressure calibration changed up to 3% between fillings. In order to adjust for this, scans were carried out over two free-spectral-ranges, and the value of $< \Delta\lambda >$ was made the fourth fit parameter. All scans were also performed by lowering the chamber pressure instead of increasing it, in order to ensure uniformity of composition for any given run.

Besides these four measurement parameters, there were up to nine relating to the actual model being compared to the experiment. A Maxwellian fit required only one parameter, temperature, but fits to asymmetric distributions required the same number of parameters as there were variables in the models: for example, the temperatures of each side of the distribution function for Lees' bimodal model, and the central temperature, T_o, plus either eight or four asymmetry coefficients for the two linearized models of Gross and Ziering. Consequently it was decided that purely graphical methods were too imprecise and that some quantitative evaluation of the fit was required in order to find the values of the parameters best matching the models to the data. A computer program was written to select initial values for the parameters, numerically integrate the convolution integrals, and then calculate the sum of squares of the differences between the model and experimental points. The parameter values were then changed one-by-one with the integration and sum-of-squares routines being repeated until a change in any individual parameter increased the sum of squares of the differences, indicating that the best fit had been obtained. It was tested on both experimental and numerically generated data of a bimodal form, i.e. a two-parameter theoretical model, containing all six search parameters, and found to contain two defects which made it very inefficient, and hence unsuitable for reduction of large amounts of data.

The first problem was the evaluation of the convolution integral. The instrument function was defined in a 'net' form, ($I_{INST} = I_N * I_R * I_I * I_P$) so that only one convolution was performed with each set of parameter values. However, this still required of the order of a hundred numerical integrations per iteration, and hence was very time consuming. The second defect was the fact that the standard error for the six-parameter fit had local minima, making the found best fit values of the parameters dependent on the initial values. If for two different computer runs the initial values of the temperature and temperature ratio used in the first iteration were changed by 10%, the program would find two different sets of 'best fit' values for these parameters, with about a 6% difference in the standard error of the fit. The computer times required to find each of these local minima were from 10 to 30 seconds, so that trying different starting values and repeating runs until the absolute minimum was found would require more than one, and up to three or four minutes of high speed computer time per experimental run. Since the bimodal model which was used to test the program was the computationally simplest one, containing only two kinetic theory parameters, an attempt to fit either of the

linearized models to the data by this method would require even longer computer times. Consequently a more efficient way of analyzing the data was sought, and the methods outlined in Sections 5.1 to 5.3 were decided upon, with the increased efficiency resulting from two factors. The first was a conversion of the intensity distribution functions to their Fourier series representations, which allowed the numerical integrations to be replaced by simple coefficient multiplications, and the second was the use of a library routine for fitting nonlinear parametric models to experimental data. This program was very efficient in finding the global minimum for a multi-parameter least-squares fit.

The actual instrument finesse was obtained by measuring the intensity profiles of lines whose Doppler shapes were known. This was done using static room temperature gas as described in Appendix A, and it was found that the instrument finesse was a factor of two lower than expected, so that there was some other unknown broadening factor, which we represent by an intensity distribution I_U, so that we have:

$$I_{OBS} = I_N * I_D * I_R * I_I * I_P * I_U + I_{baseline}$$

It was postulated that the dominant cause of the lower finesse was distortion of the interferometer plates, although there may have also been some broadening from electron-atom momentum transfer. Auxiliary tests on the interferometer, as described in Section A.3, confirmed that the distortions were the major cause of this excess width. Because the exact shape of I_U was unknown, different forms were assumed and calculations performed to determine a suitable model for use in the data analysis. Because it was the most conservative in its differentiation between theories, the assumed form was $I_U * I_R = I_{R_{eff}}$, where $I_{R_{eff}}$ is an Airy function having an effective reflectivity (R_{eff}) of 0.76. Thus all broadening effects other than the known ones, including that due to electron-atom momentum transfer, were included in the reflectivity component of the instrument function.

5.1 Sensitivity of Data Fits

It was observed in Section 2 that the theoretical studies broke down into two groups in their predictions of the heat transfer rate and density profiles between the plates: the four-moment methods, and the eight-moment and BGK solutions, with Monte Carlo results generally favouring the latter. For this reason representative models from each group were chosen for comparison with the experimental results. Methods which explicitly gave both the temperature and shape of the distribution function at each point were the four- and eight-moment hard sphere results of Gross and Ziering and the four-moment Maxwell molecule study of Lees, and hence they were the ones chosen for comparison. Two parameters which differed between the models were the temperature gradient and the degree of asymmetry in the distribution function at various Knudsen numbers and positions between the plates, and consequently these two parameters were chosen for comparison between experiment and theory. The two are not independent, because the kinetic theory representation of 'temperature' is:

$$T = \frac{m}{3kn} \int_{\underline{v}} \underline{v}^2 f(\underline{v}) d\underline{v},$$

which shows that the detailed shape of the distribution function is the prime factor which determines the temperature.

For low Knudsen numbers in the transition regime the gas behaviour is still collision dominated, so the distribution function can be approximated by a Maxwellian, and the temperature thus obtained in the following manner. The intensity distribution of the Doppler profile is represented by:

$$I_D = I_o \, e^{-\frac{mc^2}{2kT\lambda_o^2}(\lambda-\lambda_o)^2} \qquad (5.1.1)$$

where c is the speed of light (3×10^8 m/s). This distribution is then convoluted with the instrument and natural line shape functions and compared to the experimental data in order to find the values of the four measurement parameters and the temperature which best match the experimental intensity distribution.

In order to find the 'best fit' values of the model parameters in a computationally efficient fashion, one must remove the dependence of the models on convolution integrals and translate the representation into an algebraic form. This can be done by representing each of the individual intensity functions by a Fourier cosine series, making use of the property of even Fourier series that the coefficients of the series representing the convoluted function are simply the products of the coefficients of the series representing the individual functions being convoluted (Refs. 49,50,51).

If

$$F_{o_A} = a_o + \sum_{n=1}^{\infty} a_n \cos(nx) \text{ represents } A(t) \qquad (5.1.2a)$$

and

$$F_{o_B} = b_o + \sum_{n=1}^{\infty} b_n \cos(nx) \text{ represents } B(t) \qquad (5.1.2b)$$

then

$$F_{o_{AB}} = a_o b_o + \sum_{n=1}^{\infty} a_n b_n \cos(nx) \text{ represents } A(t)*B(t) \qquad (5.1.2c)$$

Expansion of each of the experimental intensity functions in terms of a cosine series is made possible by the fact that all of the functions are even, and by the repetitive nature of the Airy function. The forms of the coefficients for the cosine series expansions of the intensity functions have been derived previously (Ref. 49), and their evaluation for the specific spectral line and instrument used in this experiment are now given.

The Fourier representation of the Airy function is given by

$$F_{o_R} = 1 + 2\sum_{n=1}^{\infty} R^n \cos(nx) \qquad (5.1.3)$$

where

$$x = 2\pi \frac{\lambda - \lambda_o}{< \Delta\lambda >} \tag{5.1.4}$$

The broadening effect of the Lorentzian form of the natural line shape can be simply represented by replacing the true reflectivity, R, in the above formula, by a lower value, Re^{-L}, provided that the natural width is much less than the widths of the other instrument functions, where

$$L = \frac{2\pi \Delta\lambda_N}{< \Delta\lambda >}$$

$$= \frac{2\pi \times 0.513 \times 10^{-4} h}{0.1062}$$

$$= 3.03 \times 10^{-3} h \tag{5.1.5}$$

which for a 3 cm spacer reduces to 9.1×10^{-3}, giving an effective reflectivity of 0.991R, or 0.753 for our case. The series for the microscopic plate imperfections is Gaussian in form and has coefficients of value

$$e^{-\frac{n^2 D^2}{4}}$$

where

$$D = \frac{\pi}{\sqrt{\ln 2}\, F_I} \tag{5.1.6}$$

which for our case ($F_I = 50$) reduces to

$$F_{o_I} = 1 + \sum_{n=1}^{\infty} e^{-.00142n^2} \cos(nx) \tag{5.1.7}$$

The series representation of the square aperture function has coefficients of the form

$$\text{sinc}\left(\frac{nr^2}{f^2} \cdot \frac{h}{\lambda}\right) \tag{5.1.8}$$

where

$$\text{sinc}(\phi) = \sin(\pi\phi)/(\pi\phi) \tag{5.1.8a}$$

and inserting the values for our system we get coefficients equal to sin(0.076n)/(0.076n). The final term of interest is that for the Maxwellian Doppler profile,

which has the form

$$1 + \sum_{n=1}^{\infty} e^{-n^2M^2/4} \cos(nx)$$

where

$$M = \frac{4\pi h}{c^2\lambda_o}\sqrt{\frac{2kT}{m}} \qquad (5.1.9)$$

Again substituting the appropriate values for argon, we get

$$F_{o_D} = 1 + \sum_{n=1}^{\infty} e^{-7.75\times10^{-4}n^2T} \cos(nx) \qquad (5.1.10)$$

The net Fourier series representation of the observed intensity distribution is therefore

$$F_{o_{OBS}} = 1 + 2\sum_{n=1}^{\infty}\left[(0.753)^n e^{-0.00142n^2} e^{-7.75\times10^{-4}n^2T} \frac{\sin(0.76n)}{(0.076n)} \right] \cos(nx) \qquad (5.1.11)$$

or, in the form in which it was applied to also produce the measurement variables (height, shift, temperature, $P_{\substack{\text{etalon chamber}\\ \text{centre}}}$, $\Delta P_{\substack{\text{etalon chamber}\\ \text{fsr}}}$)

$$\mathcal{F}_{o_{OBS}} = \text{height} \times \left\{ \text{shift} + 2\sum_{n=1}^{\infty}\left[(0.753)^n e^{-0.00142n^2} e^{-7.75\times10^{-4}n^2T} \frac{\sin(0.076n)}{0.076n} \right] \right.$$

$$\left. \times \cos\left[n2\pi \frac{(P_{\substack{\text{etalon chamber}\\ \text{centre}}} - P_{\substack{\text{etalon chamber}}})}{\Delta P_{\substack{\text{etalon chamber}\\ \text{fsr}}}} \right] \right\} \qquad (5.1.12)$$

Since it is the temperature which is the variable of prime interest, an analysis was made of the sensitivity of the temperature fit to the number of terms being used in the expansion. A series of numerically generated profiles corresponding to Maxwellian distribution functions at a known temperature were fitted in a least squares manner by a twelve term cosine series of the form

$$1 + 2\sum_{n=1}^{12} a_n \cos nx$$

where the coefficients, a_n, were the adjustable parameters in the fitting routine. One fit was performed on an ideal distribution function and two others on the same distribution with different sets of random noise superimposed, and all these results were compared to the theoretical coefficient values for $\mathcal{F}_{OBS}$. The imposed noise spectrum was Gaussian with a zero mean and a standard deviation corresponding to

the square root of the signal level at any point, and hence matched the expected experimental noise spectrum. Figure 5.1.1 shows the four sets of coefficients, and it can be seen that the match to the theoretical profile is good up to the fifth term, but that beyond that term the coefficients are much higher than the Fourier ones, because the series was trying to fit the noise. In the 'no noise' case the accuracy of the fit was also limited, in this case by the limited five-place accuracy of the input data. The relative insignificance of the terms beyond the sixth was further tested by fitting six, twelve and eighteen term Fourier series to the same data and recording the best fit temperature and standard error. In all cases the change in the 'found' temperature as a result of increasing the number of terms beyond six was less than one part in 10^5. Consequently, the series used to determine temperatures from the experimental data was truncated at five terms.

Figure 5.1.2 shows the sensitivity of the fit to the temperature and noise values. Six sets of data were produced corresponding to Maxwellians with a temperature of 370°K, and noise was added to five of them. A five term Fourier cosine series of the form of Eq. 5.1.12, but with the temperature fixed at a predetermined value, was then fitted to each of these synthetic 'experimental' runs. The value of the imposed temperature was varied over a range extending 50°K on either side of the known 'true' temperature, and the standard error for the best fit was determined. This gave an indication of the minimum standard deviation that could be expected for any given temperature error, and hence the sensitivity of the fitting routine itself to temperature. Even with no noise added the error never went completely to zero, because of the inexact representation of the Fourier series, but without the noise the minimum, and hence the correct temperature, was sharply defined.

The addition of noise to the data affected the fit in two ways. The first, as would be expected, was an increase in the absolute value of the standard error. The second was a general flattening of the error-curve, indicating a greatly reduced sensitivity to temperature. Not only were the individual curves flattened, but the standard error variations between curves, at any given imposed temperature, were of the same order as the maximum increase in the error for a single curve over a ± 15% temperature range, so that the width of the 'error band' for noisy data was considerable.

In addition to these four-parameter fits, five different sets of noisy data were fitted by the full five-parameter model, and their 'found' temperatures and the corresponding standard errors of the best fits were superimposed on the plot for comparison. It can be seen that the actual 'full-parameter' behaviour of the model approached its optimum behaviour very closely and that the addition of the fifth variable produced no appreciable increase in the error. Table 5.1 shows the results of the analysis of the computer generated runs used to plot the full five parameter points on the graph.

TABLE 5.1 Noisy Data Temperature Fits to a 370°K Known Profile

Computer Run No.	Best Fit Temp. (°K)	S.E. of Fit
'No noise'	366.8	2.7×10^{-4}
Noise 11	366.8	16.6×10^{-3}
Noise 12	357.0	21.2×10^{-3}
Noise 13	347.8	19.2×10^{-3}
Noise 14	363.9	18.7×10^{-3}
Noise 15	400.1	22.6×10^{-3}
Average of Noisy Runs	367.1	19.7×10^{-3}
S_T (Noisy Runs)	19.8 (5%)	

The curves at the top of Fig. 5.1.2 show the standard error distribution for the fit of a Maxwellian to a particular model of a nonequilibrium distribution function - a bimodal Maxwellian with a geometric mean temperature of 370°K, and a temperature ratio of 0.6. It shows that the method is sensitive to lack of equilibrium in two ways: the standard deviation between the model and 'experimental curves' increases by a factor of two, and the best fit temperature drops approximately 5%. Consequently an analysis was made of the sensitivity of a Maxwellian fit to a non-Maxwellian distribution function to see if the magnitude of the standard error of the fit as a function of the 'best fit' temperature could be used to determine the degree of asymmetry in the distribution function.

To test the absolute sensitivity of the method to the degree of asymmetry in the profile, three sets of data were used in total, with each set containing six profiles corresponding to a given distribution function. The three distributions were a Maxwellian at 370°K, and two bimodal Maxwellians with geometric mean temperatures of 370°K and temperature ratios of 0.8 and 0.6. Each set consisted of one profile representing the 'pure' distribution function and five with noise added. The shift, centre, and free-spectral-range were removed as variables, so that only the best fit 'height' parameter was found for the fit to the bimodal distribution of a Maxwellian with a predetermined temperature. Because there was only one search parameter in the fitting routine, and its value was approximately known, in this case it was expedient to use the sum-of-squares search routine instead of the more general library program. The relatively high values of the deviations at 345° and 395°K for the no-noise case in Fig. 5.1.3(a) resulted from the large step size used in the search routine for this case. Comparison of Figs. 5.1.3(a) and (b) shows that for a change in temperature ratio from 1 to 0.8 there is very little increase in the standard error or decrease in the temperature at which the error is a minimum, but Fig. 5.1.3(c) shows that the error increases significantly, and the 'best fit' temperature also drops about 25°, with a further increase of the asymmetry to a value of 0.6, which corresponds to the free-molecular value for our experiment. As a result of this analysis, it was decided to use the Fourier series five-parameter fit to obtain the temperatures for all runs having near-equilibrium distribution functions. On the other hand the standard error increase, and the decrease in the temperature at which this error was a minimum were considered to be indicators that were too insensitive to allow their use for an initial evaluation of the degree of asymmetry, and another method was employed to analyse all the nonequilibrium data.

Because all of the models under consideration had discontinuities at the origin in velocity space, they could not be conveniently expressed in Fourier series form and the method used to determine temperature was not applied in this case. Consequently a parameter related to the degree of asymmetry in the distribution function and also strongly dependent on the model was used. The maximum value of the normalized function resulting from the convolution of each model with the natural and instrument functions was found, and the ratio of the areas under the curve for each side of the distribution was then determined. A ten-term sine and cosine series was fitted to each experimental run with the coefficients as parameters and the corresponding 'area ratio' calculated. An accuracy evaluation using synthetic 'experimental' data yielded an expected standard error of 6.5% in the area ratio, which was less than the maximum variation between the theoretical models of 11%. Since the expected error is less than the difference between models, it is this attribute of the various theories which can be used to test their agreement with experiment with considerably greater confidence than the temperature data.

5.2 Analysis of the Asymmetry of the Distribution Function

The experimental intensity profiles (I_{OBS}) were each plotted along with the fitted sine and cosine series. Superimposed on these plots were the theoretical intensity profiles derived for each model by convoluting the predicted distribution function (at the Knudsen number and inter-plate position corresponding to the experimental values) with the natural and instrument intensity functions, and comparisons of the fits between the experimental and theoretical curves were made. In order to average out the statistical noise, and quantify the comparison between theory and experiment, the area ratios were calculated for all the profiles. The resultant ratios were then compared in order to determine the relative degrees of asymmetry in the distribution functions.

Although the probable experimental error for a single area ratio measurement was less than the difference between models, it was still of the same order, so comparison with the various theories was done in aggregate. The area ratios were determined for all of the experimental runs, as well as calculated for each theoretical model at Knudsen numbers and inter-plate positions matching the experimental values, and then grouped into low, intermediate and high Knudsen number classes. The mean area ratio and its standard deviation were calculated for all runs at each inter-plate position within the three Knudsen number groups and then plotted along with the theoretical values.

It was observed from the plots that the mean values of the experimental area ratios varied less than 10% within each Knudsen number group and, in all but one case, the maximum variation for a given theoretical profile was also less than 10%. Consequently, it was felt that these variations were small enough that Student's t-tests could be applied to offer statistical information as a measure of how well the experimental data supported each theory. The average experimental area ratio, $\overline{ar}_{exp}$, and its standard deviation,

$$S_{ar} \left(= \sqrt{\sum_{i=1}^{n} \frac{(ar_{exp,i} - \overline{ar}_{exp})^2}{(n-1)}} \right)$$

were calculated, as was the mean area ratio for each theory, $\overline{AR}_{theor}$. The statistic

$$t = \frac{\overline{ar}_{exp} - \overline{AR}_{theor.}}{S_{ar}/\sqrt{n}}$$

which is a measure of the deviation of $\overline{ar}_{exp}$ from $\overline{AR}_{theor.}$ in terms of estimated standard units ($S_{ar}/\sqrt{n}$) was then determined to test the hypothesis $\overline{ar}_{exp} = \overline{AR}_{theor.}$ If the hypothesis were true, then t would be small, but because of the statistical variation in the data, it would be unlikely to be zero. Standard statistical tables list the values between which t will lie with a given probability (the confidence limit) if the hypothesis is true. For instance, assume that 30 measurements of ar_{exp} are used to evaluate $\overline{ar}_{exp}$ and S_{ar}. The tabulated t-value for a confidence limit of 95% and 30 degrees of freedom is 2.04, so that if $\overline{AR}_{theor}$ is an unbiased estimate of $\overline{ar}_{exp}$, only 5% of the time will t be outside the range (-2.04, 2.04). Consequently, a large value of $|t|$ allows one to state with a high degree of confidence that $\overline{AR}_{theor}$ is not a reasonable estimate of $\overline{ar}_{exp}$, and a small value of $|t|$ indicates that there is no evidence at the chosen confidence level that $\overline{AR}_{theor}$ is not equal to $\overline{ar}_{exp}$. In our case $\overline{ar}_{exp}$ is not an unbiased estimate of the 'true' experimental area ratio, but only a close approximation. This is because the area ratio is the quotient of two numbers, and division is a nonlinear operation. If the 'true' areas under each side of the curve are a_1 and a_2 (giving

a 'true' area ratio of $a_2/a_1 = ar_{true}$), then, because of symmetry considerations, we assume that the probability that the areas for a 'noisy' run and a_1 and $a_2 + \delta$ is the same as the probability that the areas are $a_1 + \delta$ and a_2. The average area ratio ($\overline{ar}$) for these two 'runs' is thus:

$$\left[\left(\frac{a_2}{a_1 + \delta}\right) + \left(\frac{a_2 + \delta}{a_1}\right)\right]/2$$

$$= ar_{true}[1 + O(\delta^2)]$$

For realistic values of δ [O(5%)], the nonlinearity of the division operator results in a bias in the estimate of the mean area ratio of approximately 0.3%, which is much less than the variation due to random noise, and hence can be neglected in the evaluation of the t-statistic. In the tabulation of the t-statistics for the experimental data the 75%, 90% and 95% confidence limits were presented.

5.3 Temperature Fits

As was seen in Section 5.1, temperature is expected to be a less strong differentiator between theories than the area ratios; however, it is still a useful parameter of comparison between theory and experiment to see if it is compatible with the area ratio result.

An analysis of computer generated data has shown that if the area ratio is less than 1.1, a pure Maxwellian distribution function can be fitted to the data with less than 1% error in the temperature. Consequently, all runs at Knudsen numbers less than 0.43 were fitted by Maxwellians, with the temperatures as variables, using the Fourier series fit described in Section 5.1. Of the theoretical models chosen for comparison with the experiment, only Lees' predicts an absolute temperature profile between the plates, with Gross and Ziering's solution assuming that the mid-point temperature is $T_o = (T_{hot} + T_{cold})/2$. Consequently, the only model with which the experimental temperatures could be compared in an absolute sense was Lees'. However, all three solutions predict temperature gradients (dT/dx), and since it is this parameter which is the dominant factor in determining the heat flux at low Knudsen numbers, it was chosen for comparison between experiment and theory. The experimental gradient was determined by fitting a straight line to the set of points for each Knudsen number below 0.43, and the slopes of these 'best fit' lines were compared to the slopes of the models' profiles.

6. RESULTS AND DISCUSSION

6.1 Asymmetry in the Distribution Function

Comparative plots of the theoretical and experimental distribution functions ($\mathcal{F}_{OBS}$) are shown for two different cases in Figs. 6.1.1(a) and (b). In the low Knudsen number case it can be seen that the eight-moment method is close to the fitted curve over most of the range, with Lees' predictions indicating a significantly greater degree of asymmetry than was observed. For the high Knudsen number case all three models match the 'cold' side well, but only Lees' gives the extended tail on the 'hot' side. This qualitative evaluation of the nature of the fit between each model and the experiment was confirmed quantitatively by the area ratio tests, as shown below.

An analysis of the experimental area ratios revealed that there was little change in value up to Kn $\approx$ 0.85, but that they rapidly increased at higher Knudsen numbers, so Kn = 0.85 was chosen as the boundary between intermediate and high Knudsen numbers for purposes of breaking the total set of runs down into subgroups for comparison with theory. The set of runs at Knudsen numbers below 0.85 was divided into roughly equal groups of low and intermediate value runs at Kn = 0.21. A total of 96 runs were used.

Figures 6.1.2(a), (b) and (c) show the three plots of area ratio versus position between the plates for the chosen Knudsen number ranges. The theoretical profiles were drawn for the extreme values of the actual experimental Knudsen numbers within the range, so that an indication of the spread due to Knudsen number is also given. It can be observed that a similar type of grouping of the theoretical models occurs here as was noted in Section 2 for the heat transfer rate predictions; the two four-moment solutions are within a few percent of each other and approximately 10% higher than the eight-moment curves, except near the hot plate at low Knudsen numbers. The experiment appears to strongly favour the eight-moment solution in the two lower Kn cases, but is between the two sets of results for the high Knudsen number data. It can also be seen from the graphs that the four-moment Gross and Ziering solution broke down near the hot plate at low and intermediate Knudsen numbers, yielding a degree of asymmetry not only significantly greater than observed, but also greater than the free-molecular limit ($AR_{\text{free molecular}} \approx 1.25$).

Statistical tests were performed on each of the three groups of data and the aggregate, and the results are summarized in Table 6.1. For these tests each experimental point was compared with the corresponding theoretical values at the same position and Knudsen number, and the results confirmed that Gross' and Ziering's eight-moment method matched the data well, but that both four-moment solutions were poor representations of the experiment for the two lower Knudsen number classes and the aggregate. In the high Knudsen number case the experimental data were approximately equidistant from both Lees' and the eight-moment models, and both solutions were within the 75% confidence limit.

TABLE 6.1 Area Ratio Statistics

(a) Aggregate

Model	Mean Area Ratio	t (75% - 1.16) (90% - 1.66) (95% - 1.98)
Experiment	1.104 (S_{ar}=.103)	
Lees - 4	1.210	- 10.19
Gross & Ziering - 4	1.229	- 12.08
Gross & Ziering - 8	1.108	- 0.44

(b) $Kn \leq 0.21$

Model	Mean Area Ratio	t (75% - 1.17) (90% - 1.68) (95% - 2.02)
Experiment	1.056 (S_{ar}=.085)	
Lees	1.159	- 7.43
Gross & Ziering - 4	1.215	- 11.49
Gross & Ziering - 8	1.081	- 1.80

(c) $.21 < Kn \leq .85$

Model	Mean Area Ratio	t (75% - 1.16) (90% - 1.68) (95% - 2.02)
Experiment	1.114 (S_{ar}=.095)	
Lees	1.246	- 9.44
Gross & Ziering - 4	1.230	- 8.27
Gross & Ziering - 8	1.111	- 0.21

(d) $Kn > .85$

Model	Mean Area Ratio	t (75% - 1.20) (90% - 1.76) (95% - 2.14)
Experiment	1.197 (S_{ar}=.104)	
Lees	1.227	- 1.07
Gross & Ziering - 4	1.256	- 1.84
Gross & Ziering - 8	1.172	+ 0.92

In determining the asymmetry parameters for the eight-moment solution, a series of calculations were performed with the accommodation coefficient being allowed to vary between 0.83, the value used by Teagan and Springer in the analysis of their data, and unity. It was found that the variation in the area ratio at any given point was less than 1%, indicating that the parameter chosen in our study was relatively insensitive to variations in the accommodation coefficient as long as its value was near unity. Since the temperatures of both plates were low relative to flash points for desorption of most contaminants, and there was noticeable booster pump oil on cooled surfaces in the test section despite the chevron baffle in the connecting tube, it is reasonable to assume that the plate surfaces were 'dirty' and consequently had near unity accommodation coefficients.

6.2 Temperature Profiles

The compatibility of the temperature profile results with the asymmetry results was tested using a total of 65 runs broken down into six Knudsen number classes in the range $0.07 \leq Kn < 0.43$. In this range the experimental area ratios were less than 1.1, so a Maxwellian distribution could be fitted to the data with less than 1% error in the temperature. Within each class a straight line was fitted to the experimental points $[x/D, T(x/D)]$ for comparison with the theoretical temperature profiles. The slopes of the lines were compared to the temperature gradients predicted by all three models, and the mid-point temperatures were compared to those predicted by Lees' solution. Figure 6.2.1 shows a typical fit of a Maxwellian to an experimental run at a low Knudsen number. The transition of the mid-point temperature from continuum to free molecular conditions is shown in Fig. 6.2.2 where a nondimensional representation of the temperature is shown as a function of inverse Knudsen number.

All of the linearized solutions fix the mid-point temperature at the algebraic mean of the plate temperatures, which is the value it would have in the continuum regime. As the flow regime approaches the free-molecular, the mid-point temperature drops, until the limiting case of the geometric mean of the plate temperatures is reached. If the linearizing condition $\Delta T/T_o \ll 1$ is met the two mean temperatures are essentially equal, and no complication arises in applying linearized solution methods to transition and free-molecular flow. However if $\Delta T/T_o \not\ll 1$, the linearized models are unable to predict realistic profiles below the onset of transition. Figure 6.2.2 shows that the Lees model predicts the start of transition at Knudsen numbers near 0.1, which is consistent with the Monte Carlo results of Cheremisin (Ref. 14), even though the latter were derived for plates having a temperature ratio of four. The experimental mid-point temperatures, determined from the mid-point of the best-fit straight lines, were found to be about 1.5% lower than the Lees' values on the average, but since this is well within the 5% error of the temperature measurements, there is no experimental evidence that temperature transition is poorly represented by the bimodal model.

The inter-plate temperature profiles are plotted for all six Knudsen numbers studied in Figs. 6.2.3(a), (b) and (c). Each profile is plotted with the ordinate being expressed as a temperature difference from the mean temperature for that model, so that the slopes may be compared directly. Both the best-fit straight line and the individual points are shown for the experimental data as visual indicators of the amount of scatter. The standard deviation for all points from their respective straight lines was 19°K, within the range expected from the analysis of the computer generated data. The curves for all three models are

well matched by the experiment, and the differences between solutions are so slight that no one solution can be said to be better matched by the experiment than any other.

The experimental temperature profiles are thus seen to be compatible with the area ratio results in that they match the theoretical temperature gradients closely, and the mid-point temperatures are close to Lees' values. However, because only one theory predicts a mid-point temperature, and all three theories predict similar temperature gradients, no differentiation between models is possible.

6.3 Summary of Results

The linearized eight-moment model of Gross and Ziering was found to be a good representation of the experimental distribution functions. Statistical tests on the area ratio measurements confirmed that the degree of asymmetry predicted by this model matched the experimental asymmetries through the Knudsen number range studied. The four-moment result of Gross and Ziering broke down near the hot plate at low Knudsen numbers but over most of the inter-plate region it closely matched Lees' bimodal model in its prediction of the degree of asymmetry. Both four-moment solutions gave asymmetries greater than the experimental values throughout the entire Knudsen number range, with the difference being statistically significant below Kn = 0.85. Near a Knudsen number of unity the experimental results began to approach Lees' solution, which would be expected to exactly model the free molecular case.

All three theories predicted temperature gradients close to the experimental values. Because of the large experimental error relative to the variation between the models, it was not possible to differentiate between them using the temperature data, but only to state that all three theories were compatible with the experimental results.

7. CONCLUSIONS

Measurements of the Doppler profile of the 4609Å AII line in the fluorescence spectrum of argon excited by an electron beam have been used to measure the degree of asymmetry in the distribution function and gas temperatures for the transition flow parallel plate heat transfer problem. The plate temperature ratio was 1.7 and Knudsen numbers in the range 0.07 to 3 were obtained.

The parameter values predicted by approximate solutions of the Boltzmann equation fall into two distinct groups, and representative models from each group were compared to the experimental data. The linearized four- and eight-moment results of Gross and Ziering and the four-moment bimodal method of Lees were chosen, and statistical analyses were performed to find the method which best matched the data.

The inter-plate temperature profiles predicted by all three methods were close to the experimental profiles, but the difference between models was of the same order as the experimental error, so that it can only be stated that the theories were compatible with the experimental data. In the asymmetry studies, however, the eight-moment solution was significantly closer to the experimental results than the other two for Knudsen numbers up to 0.85, above which the

experimental points lay approximately evenly between the two theories. The Gross and Ziering models assumed $\Delta T/T_o \ll 1$ but this ratio in the experiments had a value of 0.26 and consequently the validity of using a linearized model might be doubtful. Monte Carlo studies of the problem at Knudsen numbers up to 0.5 and with temperature ratios of four indicate that the linearized eight-moment model apparently gives good results beyond its nominal range of validity, and the experiments confirmed this to be true. At Knudsen numbers greater than unity Lees bimodal model more closely matched the experiment than at lower Knudsen numbers, but it still predicted too great a degree of asymmetry, resulting from too high a temperature difference in the two halves of the distribution. Consequently it can be concluded that both four-moment solutions were bad representations of the data, because they predicted too great a degree of disequilibrium in the distribution function, especially at lower Knudsen numbers in the transition range. The eight-moment linearized solution of Gross and Ziering matched the data very well over the entire Knudesn number range studied so that the range of validity of the method appears to be less limited than the a priori linearizing condition.

The data in this experiment were reduced using the same constant pressure assumption as the experiments of Teagan and Springer and Alofs, Flagan,and Springer. The maximum difference in pressure would be expected to occur when the 'entrance' to the interplate region became free-molecular, at which case the thermal transpiration effect would lower the mean density by approximately 15%, with an equivalent increase in Knudsen number. In the near-continuum regime where the results were most definitive, this effect would not be expected. The observed asymmetries for each model and the experiment were constant to a few percent over an order of magnitude range of Knudsen numbers, but differed by up to 15% between models within a given study range, so that even if there was a slight difference in pressure, it would not significantly change the results.

Analysis of the data was complicated by the presence of a constant background light level which reduced the temperature and degree of asymmetry sensitivity of the experiment. It has been postulated (Ref. 57) that this background, which has been observed in all argon studies, may be a result of anomalously high intensity tails of the distribution function overlapping through adjacent orders of the interferometer. The suggested mechanism by which the tails were 'over-populated' was momentum transfer from secondary electrons. However, calculations have been performed which showed that the maximum velocity which could be imparted to an argon atom by this mechanism was only 12% of the thermal speed. Collisions with primary beam electrons are capable of producing recoil velocities greater than the thermal speed but almost all of the collisions involve scattering angles less than 10° (Ref. 58), for which the perturbations are still much less than the thermal speed. Consequently it appears highly unlikely that the high background level is caused by electron-atom momentum transfer. It may simply be continuum radiation which wasn't observed in helium because of the stronger signal. No matter what the cause, its principal effect is an uncertainty in the zero-intensity baseline for the spectral line profile with a consequent loss of information about the nature of the high speed portions of the distribution function.

The optical system used had a net finesse of 10.7, the low value most likely resulting from distortion of the etalon plates by the mounting springs. More recently available instruments can raise the finesse to close to 30, along with larger apertures, giving a net gain in optical speed. When incorporated, such advances would increase the accuracy of the optical system by a maximum factor of

three, enough to improve the statistics of comparison, but not sufficient to remove the requirement for statistical analysis. Consequently, because the level of confidence in the results was already high with the low finesse optical system, improvements in the quality of the system would not significantly enhance the differentiation between models.

REFERENCES

1. Teagan, W. P.
   Springer, G. S.
   Heat Transfer and Density Distribution Measurements Between Parallel Plates in the Transition Regime, Phys. Fluids 11, No. 3, March 1968.

2. Alofs, D. J.
   Flagan, R. C.
   Springer, G. S.
   Density Distribution Measurements in Rarefied Gases Contained Between Parallel Plates at High Temperature Differences, Phys. Fluids, 14, No. 3, March 1971.

3. Möller, E.
   Adomeit, G.
   Investigation of the Plane Heat Conduction Problem in the Transition Regime, Proceedings of the Ninth International Symposium on Rarefied Gasdynamics, Becker and Fiebig, Editors, DFVLR Press, 1974.

4. Wang Chang, C. S.
   Uhlenbeck, G. E.
   The Heat Transport Between Two Parallel Plates as Functions of the Knudsen Number, University of Michigan Project M999, 1953.

5. Gross, E. P.
   Ziering, S.
   Heat Flow Between Parallel Plates, Phys. Fluids, 2, No. 6, Nov-Dec. 1959.

6. Bassanini, P.
   Cercignani, C.
   Pagani, C. D.
   Comparison of Kinetic Theory Analyses of Linearized Heat Transfer Between Parallel Plates, Int. J. Heat and Mass Transfer, 10, pp. 447-460, 1967.

7. Bassanini, P.
   Cercignani, C.
   Pagani, C. D.
   Influence of the Accommodation Coefficient on the Heat Transfer in a Rarefied Gas, Int. J. Heat and Mass Transfer, 11, pp. 1359-1369, 1968.

8. Yen, S. M.
   Schmidt, H. J.
   Monte Carlo Solutions of the Boltzmann Equation for Heat Transfer Problems, Proceedings of the Sixth International Symposium on Rarefied Gasdynamics, Trilling and Wachman, Editors, Academic Press, 1969.

9. Yen, S. M.
   Monte Carlo Solutions of Nonlinear Boltzmann Equation for Problems of Heat Transfer in Rarefied Gases, ASME paper 69-WA/HT-23, American Society of Mechanical Engineers, 1969.

10. Willis, D. R.
    Heat Transfer in a Rarefied Gas Between Parallel Plates at Large Temperature Ratios, Proceedings of the Third International Symposium on Rarefied Gas Dynamics, J. A. Laurmann, Editor, Academic Press, 1963.

11. Lees, L.
    A Kinetic Theory Description of Rarefied Gas Flows, Hypersonic Research Project Memorandum No. 51, California Institute of Technology, 1959.

12. Lees, L.
Liu, C-Y.
Kinetic Theory Description of Plane, Compressible Couette Flow, Hypersonic Research Project Memorandum No. 58, California Institute of Technology, 1960.

13. Lavin, M. L.
Haviland, J. K.
Application of a Moment Method to Heat Transfer in Rarefied Gases, Phys. Fluids, 5, No. 3, March 1962.

14. Cheremisin, F. G.
Development of a Direct Method of Solution for the Boltzmann Equation, in 'Numerical Methods in Rarefied Gasdynamics', Edition 1, Computing Centre of the Academy of Sciences of the USSR, 1973 (in Russian).

15. Haviland, J. K.
Monte Carlo Application to Molecular Flows, MIT Fluid Dynamics Research Laboratory Report No. 61-5, Massachusetts Institute of Technology, 1961.

16. Haviland, J. K.
Lavin, M. L.
Application of the Monte Carlo Method to Heat Transfer in a Rarefied Gas, Phys. Fluids, 5, No. 11, November 1962.

17. Tuer, T. W.
A Test Particle Monte Carlo Method With Application to the Free Jet Expansion Problem, Ph.D. Thesis, University of Michigan, Dept. of Mechanical Engineering, 1973.

18. Perlmutter, M.
Rarefied-Gas Heat Transfer Between Parallel Plates by a Monte Carlo Method, Proceedings of the Third International Heat Transfer Conference, American Institute of Chemical Engineers, 1966.

19. Perlmutter, M.
Rarefied-Gas Couette Flow and Heat Transfer Between Parallel Plates by Model Sampling, NASA TN D-4579, U.S. National Aeronautics and Space Administration, 1968.

20. Bird, G. A.
Direct Simulation Monte Carlo Method, Proceedings of the Sixth International Symposium on Rarefied Gas Dynamics, Trilling and Wachman, Editors, Academic Press, 1969.

21. Welander, P.
On the Temperature Jump in a Rarefied Gas, Ark. Fys. 7, pp. 506-553, 1954.

22. Bhatnagar, P. L.
Gross, E. P.
Krook, M.
A Model for Collision Processes in Gases, Phys. Rev., 94, 1954.

23. Saraf, J. R.
Heat Transfer in Rarefied Couette Flow on the Basis of Discrete Ordinate Method, Appl. Sci. Res., 24, Oct. 1971.

24. Srivastava, M. P.
Saraf, J. R.
Non-Linear Couette Flow With Heat Transfer Using the B-G-K Model, Zeit. Ang. Math. Phys. 22, No. 3, April 1971.

25. Huang, A. B.
Hwang, P. F.
Test of Statistical Model for Gases With and Without Internal Energy States, Phys. Fluids, 16, No. 4, April, 1973.

26. Bird, G. A.
Private Communication.

27. Nordsieck, A.
Hicks, B. L.
Monte Carlo Evaluation of the Boltzmann Collision Integral, Proceedings of the Fifth International Symposium on Rarefied Gas Dynamics, C. L. Brundin, Editor, Academic Press, 1967.

28. Cheremisin, F. G.
Private Communication.

29. McMichael, G. E.
Electron Beam Densitometer Investigation of Diffusive Separation in Front of a Blunt Body in Low Density Helium-Argon Flows, UTIAS Report 167, University of Toronto Institute for Aerospace Studies, 1971.

30. Payne, W. F.
Characteristics of an Argon Free Jet Expanded from a High Pressure Inductive Arc Source, UTIAS Report 165, University of Toronto Institute for Aerospace Studies, 1971.

31. Fraser, R. B.
Diagnostic Studies in an Induction Heated Supersonic Argon Plasma, Report No. AS-70-5, College of Engineering, University of California, Berkeley.

32. Cattolica, R. J.
An Experimental Study of Translational Non-Equilibrium in Free Jet Expansions, Report No. FM-72-6, College of Engineering, University of California, Berkeley.

33. Cattolica, R. J.
Robben, F.
Talbot, L.
Willis, D. R.
Translational Nonequilibrium in Free Jet Expansions, Phys. Fluids, 17, No. 10, Oct. 1974.

34. Harnett, L. N.
An Experimental Investigation of Normal Shock Wave Distribution Functions in Mixtures of Argon and Helium, Report No. AS-69-5, College of Engineering, University of California, Berkeley.

35. Muntz, E. P.
Measurement of Rotational Temperature, Vibrational Temperature, and Molecule Concentration, in Non-Radiating Flows of Low Density Nitrogen, UTIA Report 71, University of Toronto Institute of Aerophysics, 1961.

36. Schumacher, B. W.
Gadamer, E. O.
Electron Beam Fluorescence Probe for Measuring the Local Gas Density in a Wide Field of Observation, Can. J. Phys. 36, 1958.

37. Gadamer, E.O.
Measurement of the Density Distribution in a Rarefied Gas Flow Using the Fluorescence Induced by a Thin Electron Beam, UTIA Report 83, University of Toronto Institute of Aerophysics, 1962.

38. Muntz, E. P. — The Direct Measurement of Velocity Distribution Functions, Proceedings of the Fourth International Symposium on Rarefied Gas Dynamics, J. H. deLeeuw, Editor, Academic Press, 1965.

39. Becker, M., Robben, F., Cattolica, R. J. — Velocity Distribution in Hypersonic Helium Flow Near the Leading Edge of a Flat Plate, AIAA Sixth Fluid and Plasma Dynamics Conference, AIAA Paper No. 73-691, American Institute of Aeronautics and Astronautics, 1973.

40. Poon, C. C. — Spectroscopic Study of Electron Energy and Kinetics of States of Principal Quantum Number 2 in Helium Plasma Jets, Report No. FM-75-11, College of Engineering, University of California, Berkeley.

41. Rockett, P., Brundin, C. L. — A Study of Some Thermal States of Nitrogen by the Method of Electron Beam Induced Fluorescence, Presented at the Ninth International Symposium on Rarefied Gas Dynamics, 1974.

42. Robben, F., Cattolica, R., Coe, D., Talbot, L. — Anomalous Line Width of the Electron Beam Fluorescence of Nitrogen, Proceedings of the Tenth International Symposium on Rarefied Gas Dynamics, J. L. Potter, Editor, AIAA, to be published, 1976.

43. Meissner, K. W. — Interference Spectroscopy, Parts 1 and 2, J. Opt. Soc. Am., 31, No. 6, June 1941, and 32, No. 4, April 1942.

44. Chabbal, R. — Recherche des Meilleurs Conditions d'Utilisation d'un Spectromètre Photoélectrique Fabry-Perot, J. des Recherches du CNRS, No. 24, 1953.

45. Chabbal, R. — Recherches Expérimentales et Théoriques sur la Généralisation de l'Emploi du Spectromètre Fabry-Perot aux Divers Domains de la Spectroscopie, Revue d'Optique, 37, No. 2, 1958.

46. Mercure, H. P-E. — Ion Temperature Measurement in a Flowing Collisionless Plasma Using an End Effect of Cylindrical Langmuir Probes, UTIAS Report No. 202, University of Toronto Institute for Aerospace Studies, 1976.

47. deLeeuw, J. H., Davies, W.E.R., Haasz, A. A., Unger, J. I. — Diagnostics With Rocketborne Electron Beam Fluorescence Probes, UTIAS Report No. 197, University of Toronto Institute for Aerospace Studies, 1976.

48. Olsen, H. N. — Measurement of Argon Transition Probabilities Using the Thermal Arc Plasma as a Radiation Source, J. Quant. Spect. Rad. Transf. 3, 1963.

49. Hernandez, G. — Analytic Description of a Fabry-Perot Photoelectric Spectrometer, App. Opt., 5, No. 11, Nov. 1966.

50. Larson, H. P.
Andrew, K. L.
A Least-Squares Deconvolution Technique for the Photoelectric Fabry-Perot Spectrometer, App. Opt. 6, No. 10, Oct. 1967.

51. Hays, P. B.
Roble, R. G.
A Technique for Recovering Doppler Line Profiles from Fabry-Perot Interferometer Fringes of Very Low Intensity, App. Opt., 10, No. 1, Jan. 1971.

52. Brundin, C. L.
Private Communication.

53. Ziering, S.
Shear and Heat Flow for Maxwellian Molecules, Phys. Fluids, 3, No. 4, July-August 1960.

54. Griem, H. R.
Plasma Spectroscopy, McGraw-Hill, 1964.

55. Cercignani, C.
Theory and Applications of the Boltzmann Equation, Elsevier, 1975.

56. Caplan, J.
Temperature and Pressure Effects on Pressure-Scanned Etalons and Gratings, App. Opt., 14, No. 7, July 1975.

57. Robben, F.
Measurement of Velocity Distribution Function from Electron Beam Fluorescence, Proceedings of the Ninth International Symposium on Rarefied Gas Dynamics, Becker and Fiebig, Editors, DFVLR Press, 1974.

58. Muntz, E. P.
The Electron Beam Fluorescence Technique, AGARD-ograph 132, NATO, Advisory Group for Aerospace Research and Development, 1968.

59. Holtz, T.
Measurements of Molecular Velocity Distribution Functions in an Argon Normal Shock Wave at Mach Number 7, Ph.D. Thesis, University of Southern California, 1974.

60. Moore, C. E.
Atomic Energy Levels, United States Department of Commerce, National Bureau of Standards, Circular 467, 1948.

61. Marton, L.
Schiff, L. I.
Determination of Object Thickness in Electron Microscopy, J. App. Phys., 12, No. 10, Oct. 1941.

62. Dunn, D. A.
Self, S. A.
Static Theory of Density and Potential Distribution in a Beam Generated Plasma, J. App. Phys., 35, No. 1, Jan. 1964.

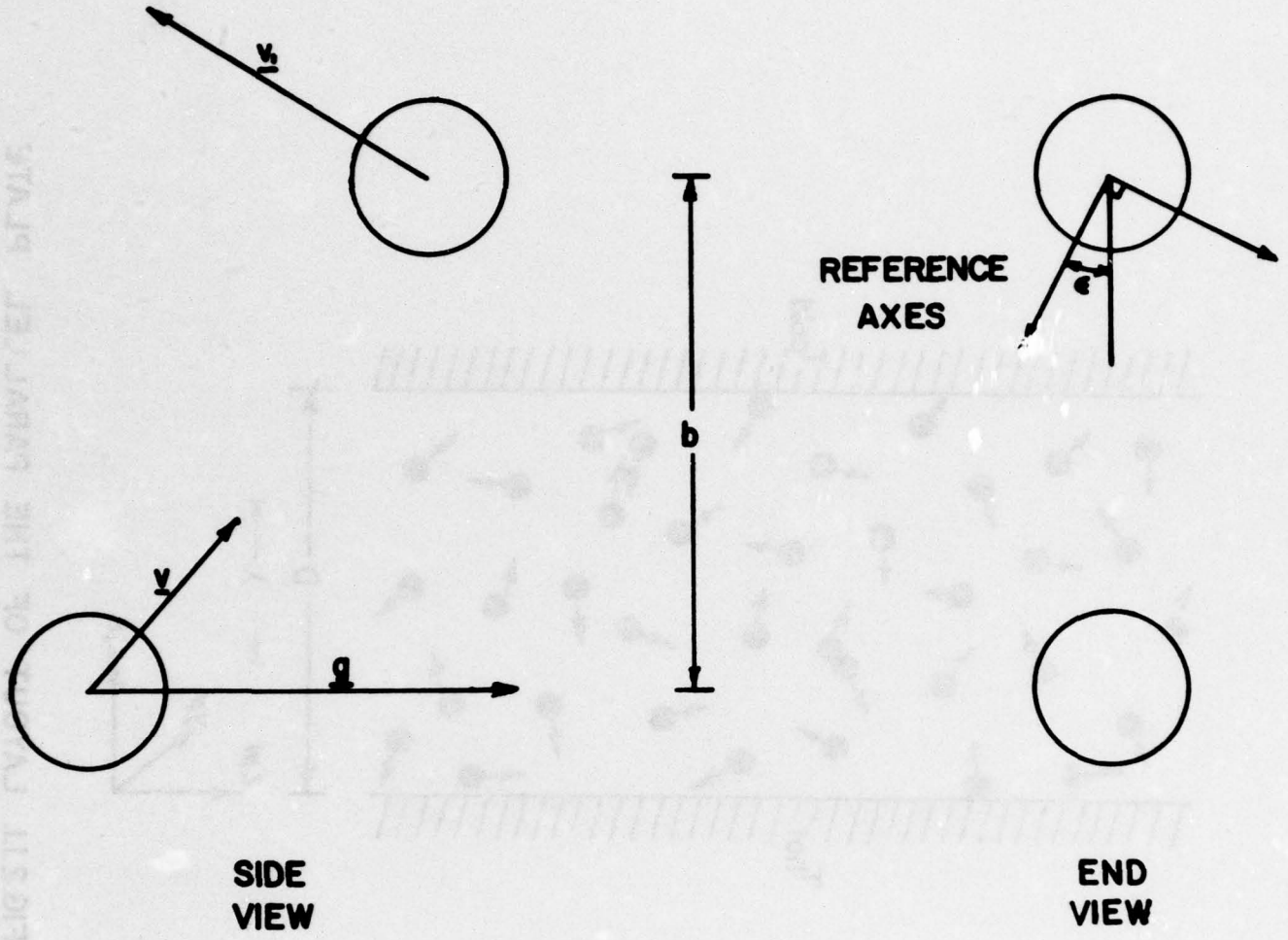


FIG. I.I. GEOMETRY OF A TWO-PARTICLE COLLISION

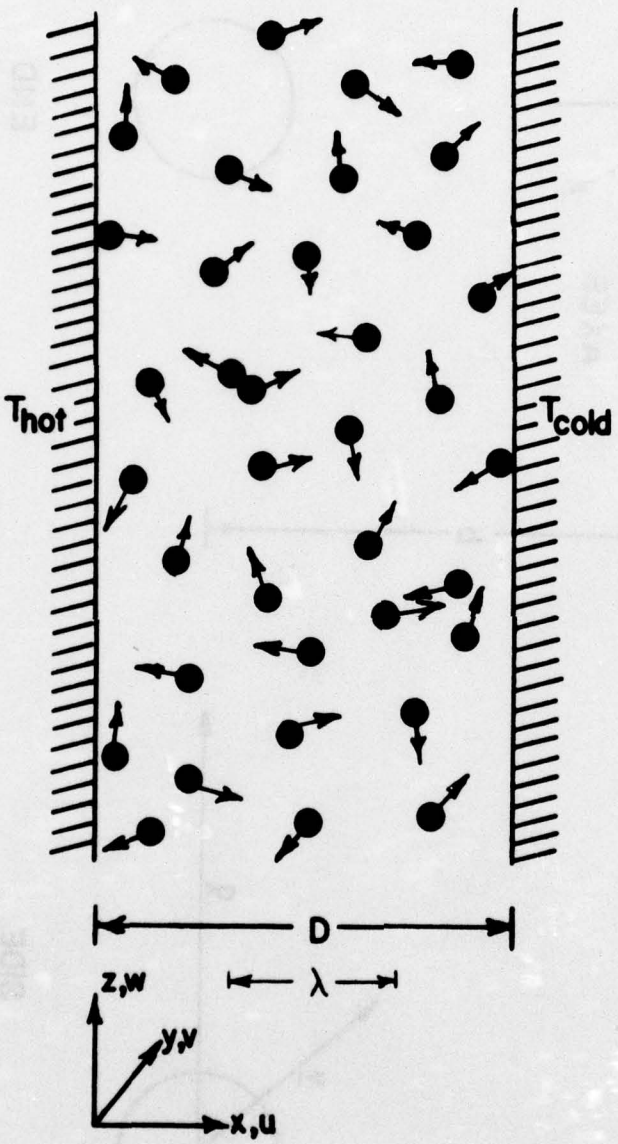


FIG.2.1.1. LAYOUT OF THE PARALLEL PLATE HEAT TRANSFER PROBLEM

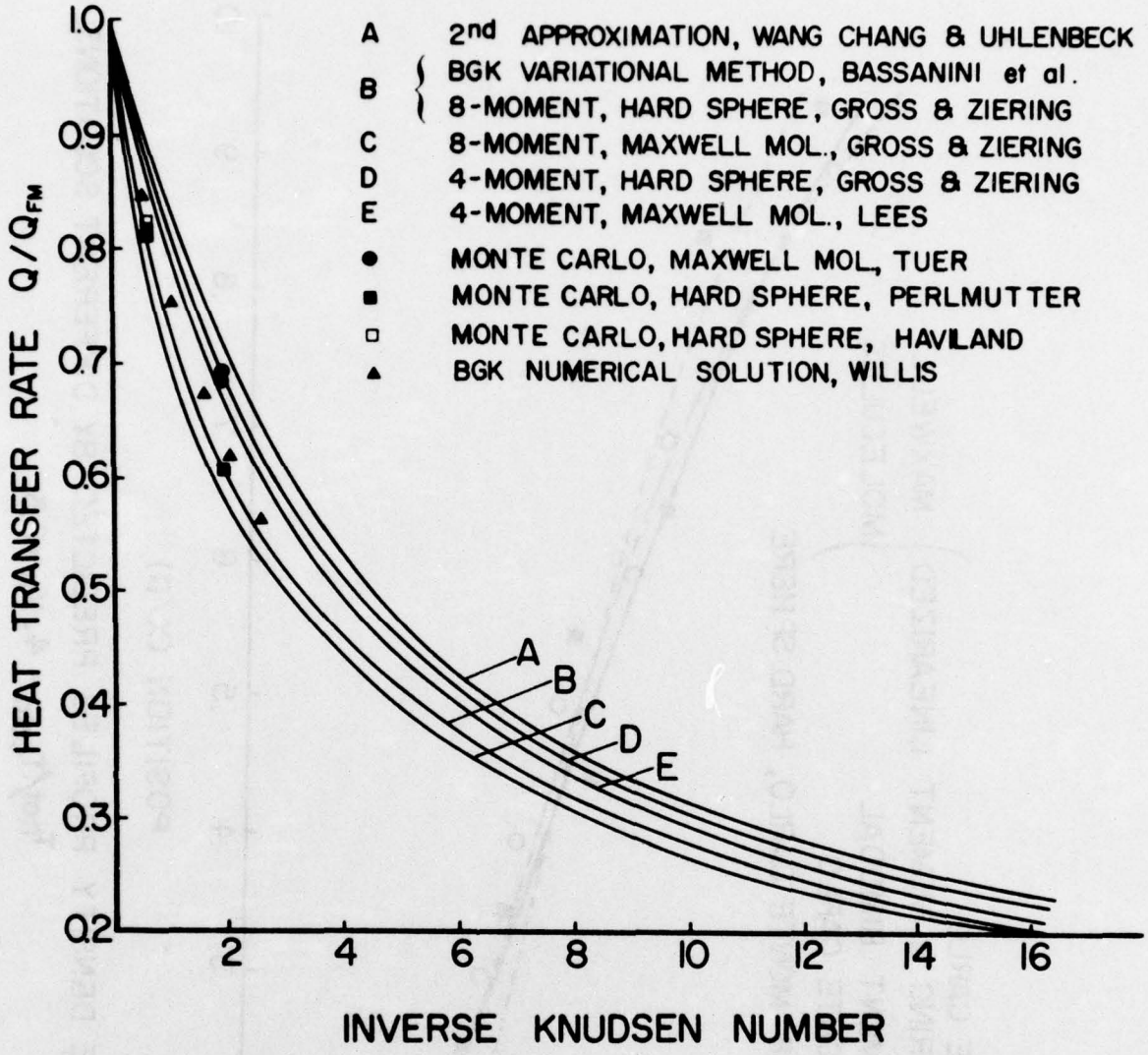


FIG.2.1.2. HEAT TRANSFER RATE AS A FUNCTION OF KNUDSEN NUMBER

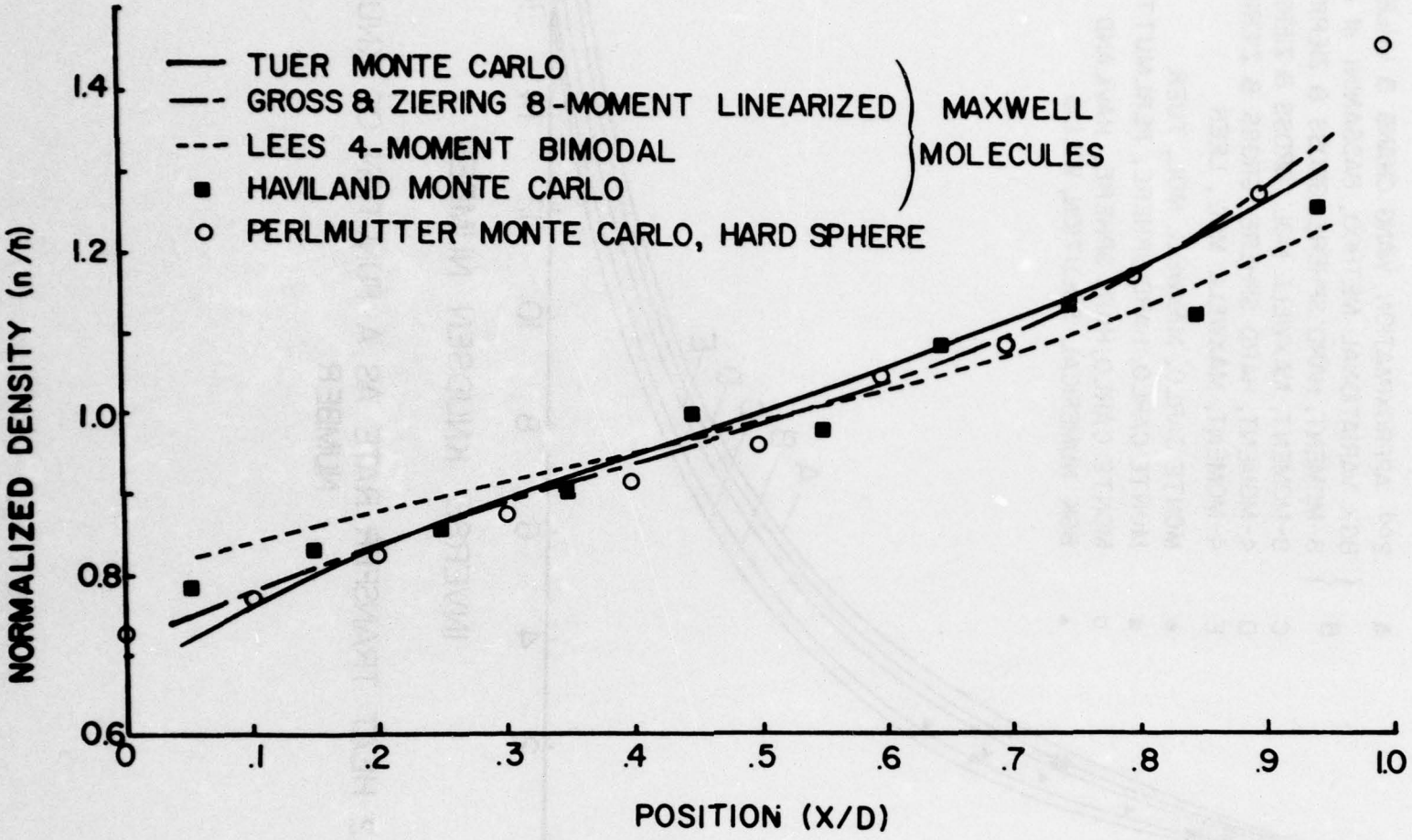
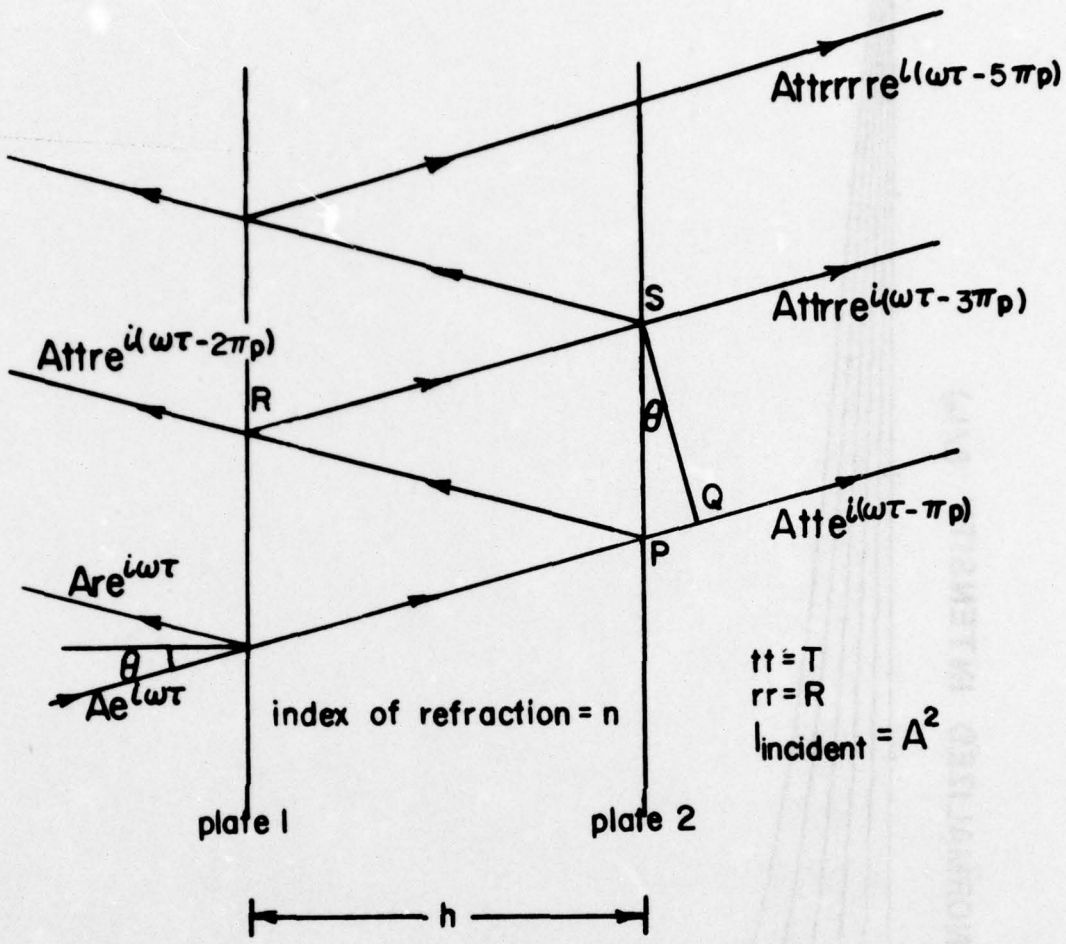


FIG.2.51. INTER-PLATE DENSITY PROFILES PREDICTED BY DIFFERENT SOLUTIONS
$T_{hot}/T_{cold} = 4$, $Kn = 0.5$



order: $p = \frac{2nh}{\lambda}\cos\theta$

intensity distribution:

$$I_t(\lambda,\theta) = \frac{I_0}{1 + \frac{4R}{(1-R)^2}\sin^2(\pi p)}$$

FIG. 3.2.1(a). IDEAL FABRY-PEROT INTERFEROMETER

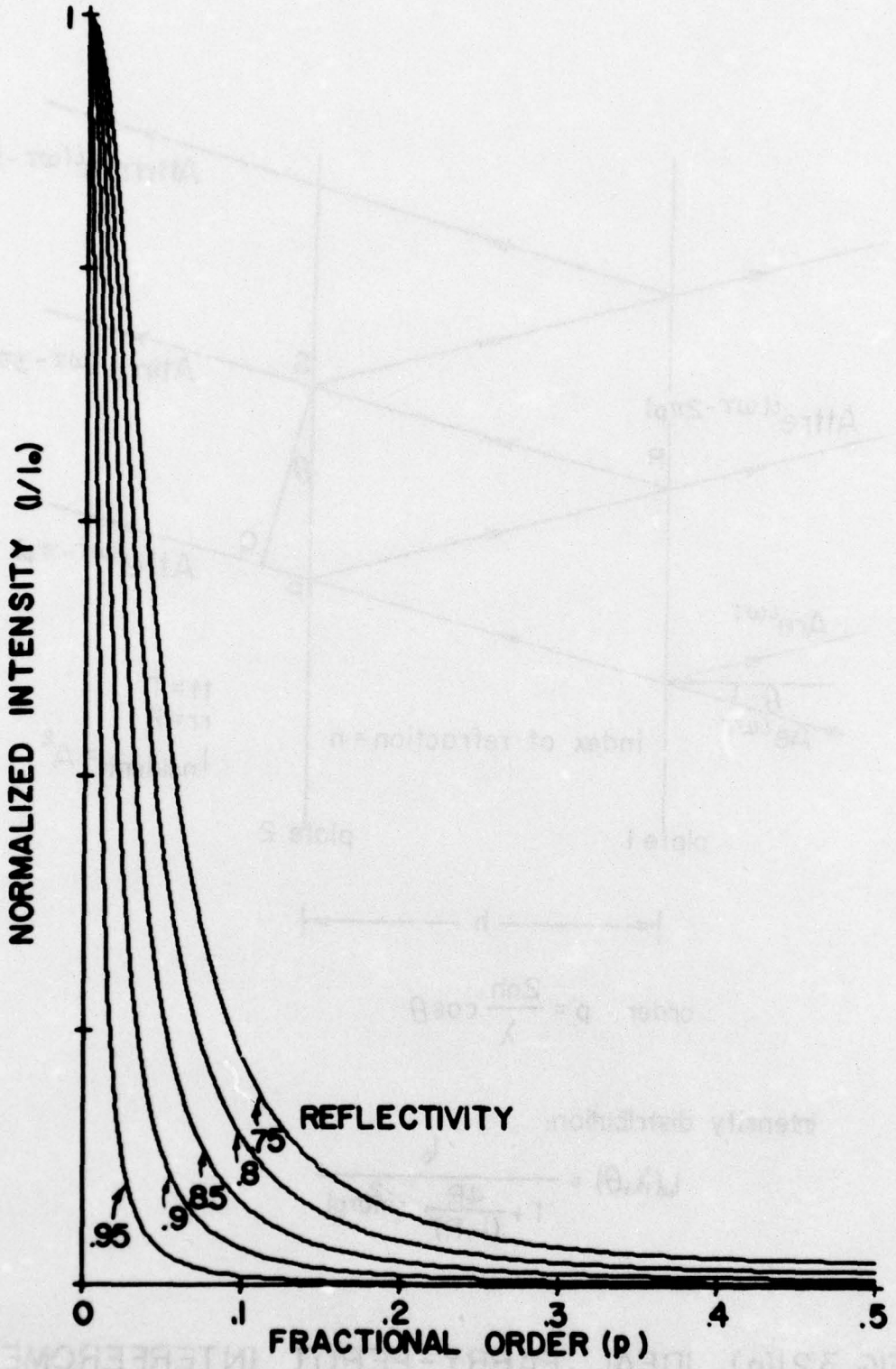


FIG.3.2.1(b). IDEAL INTERFEROMETER INTENSITY DISTRIBUTION

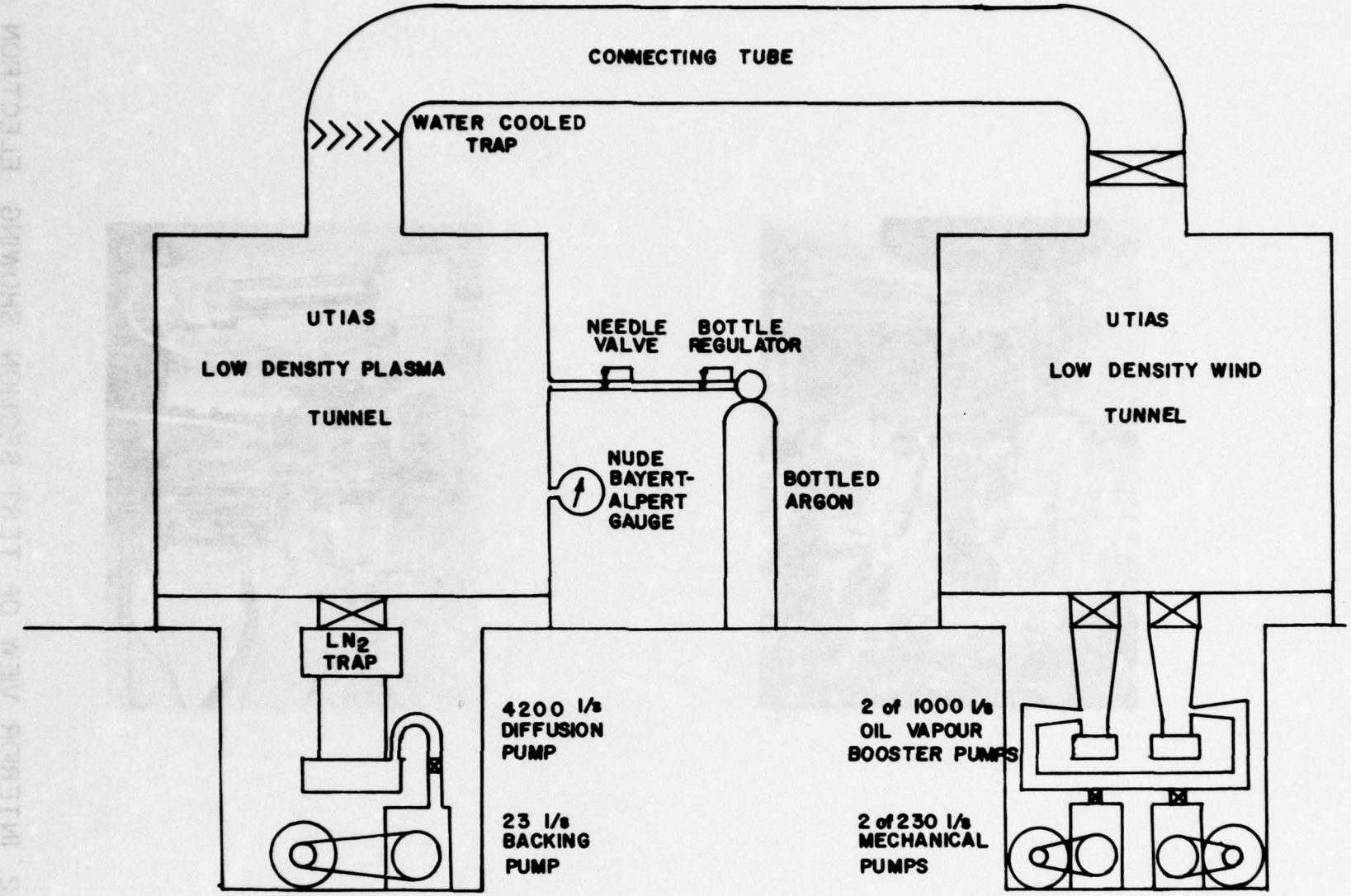
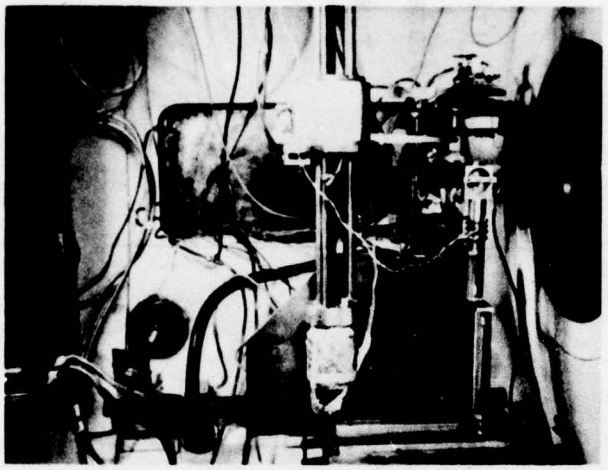


FIG. 4.1.1 SCHEMATIC OF THE VACUUM SYSTEM



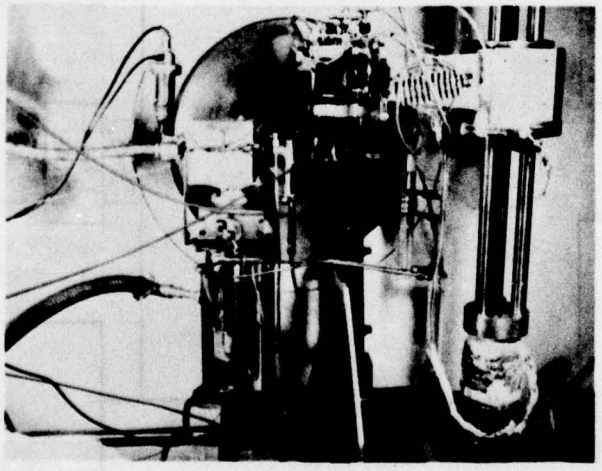


FIG. 4.1.2. INTERIOR VIEW OF TEST SECTION SHOWING ELECTRON GUN & PARALLEL PLATE ASSEMBLIES

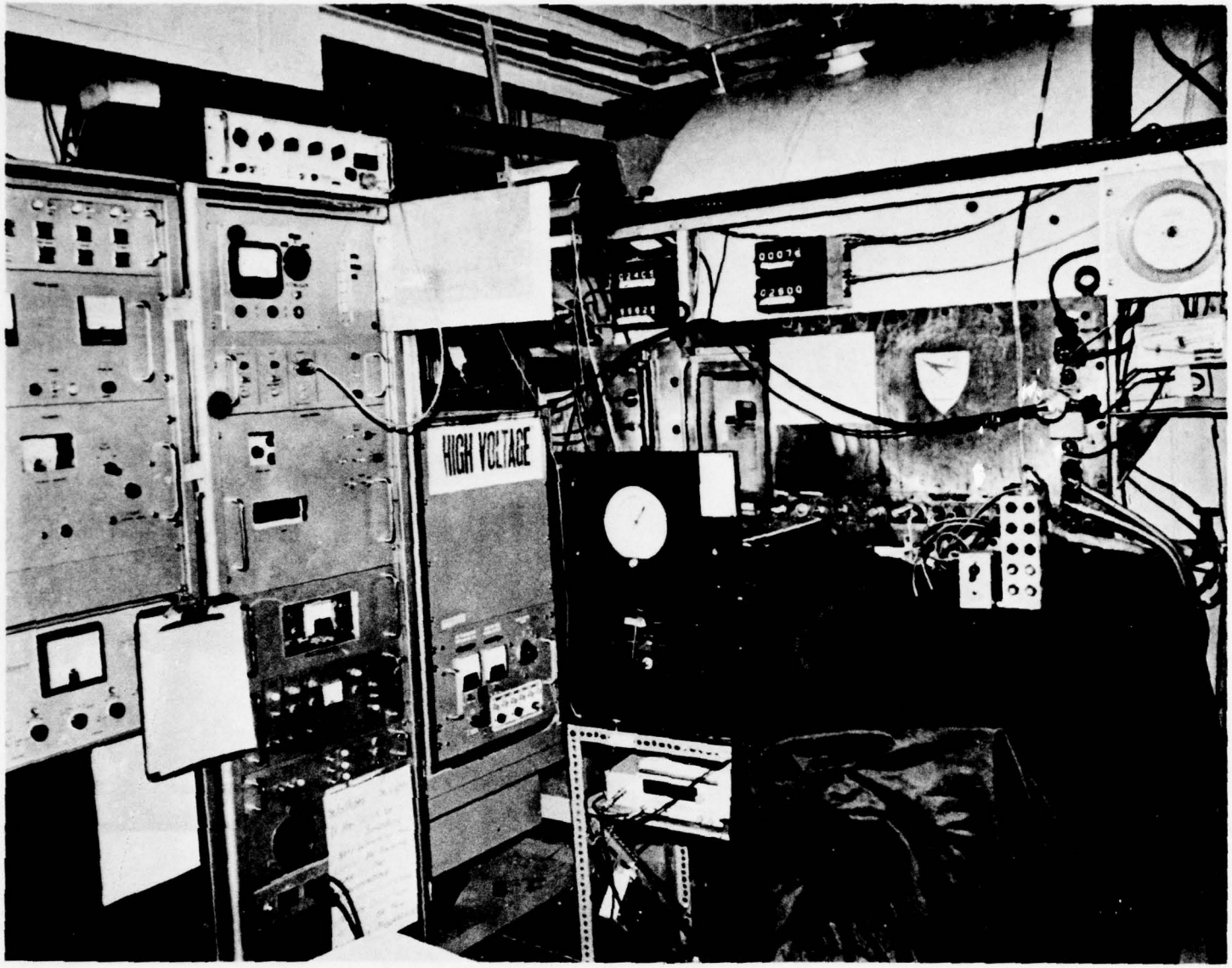
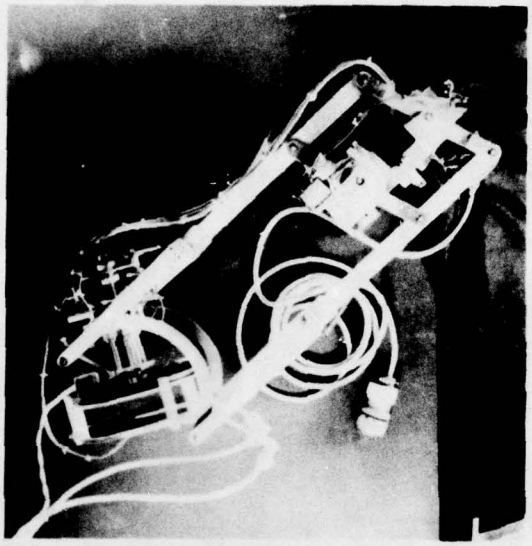


FIG. 4.1.3. GENERAL VIEW OF THE FACILITY SHOWING THE LOW DENSITY PLASMA TUNNEL & CONTROL PANELS



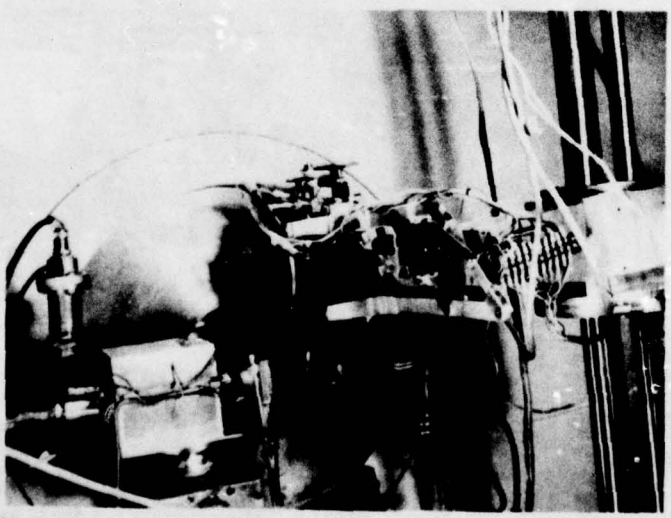


FIG. 4.2.1. THE PARALLEL PLATE RIG

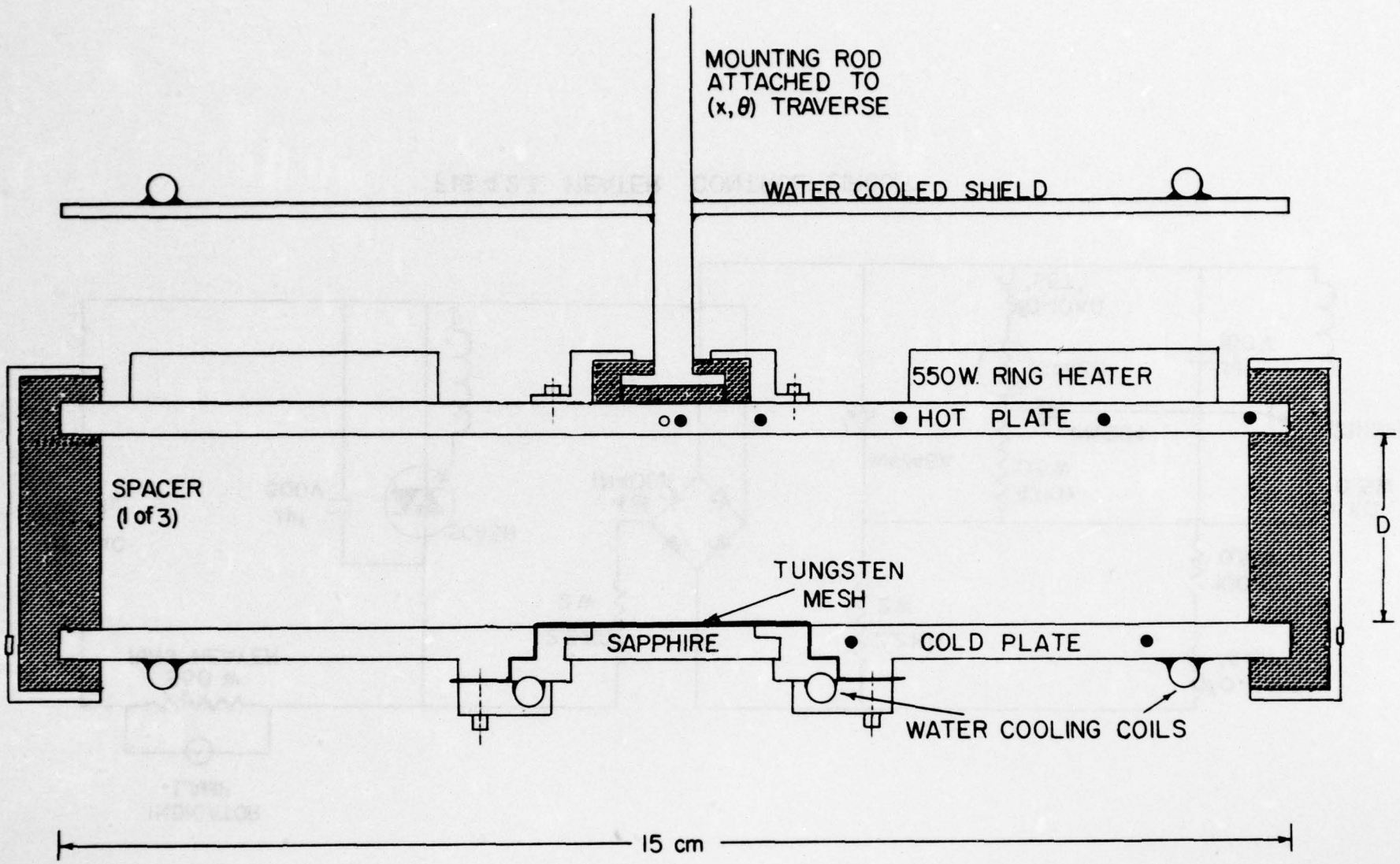


FIG. 4.2.2. SCHEMATIC OF THE PARALLEL PLATE ASSEMBLY

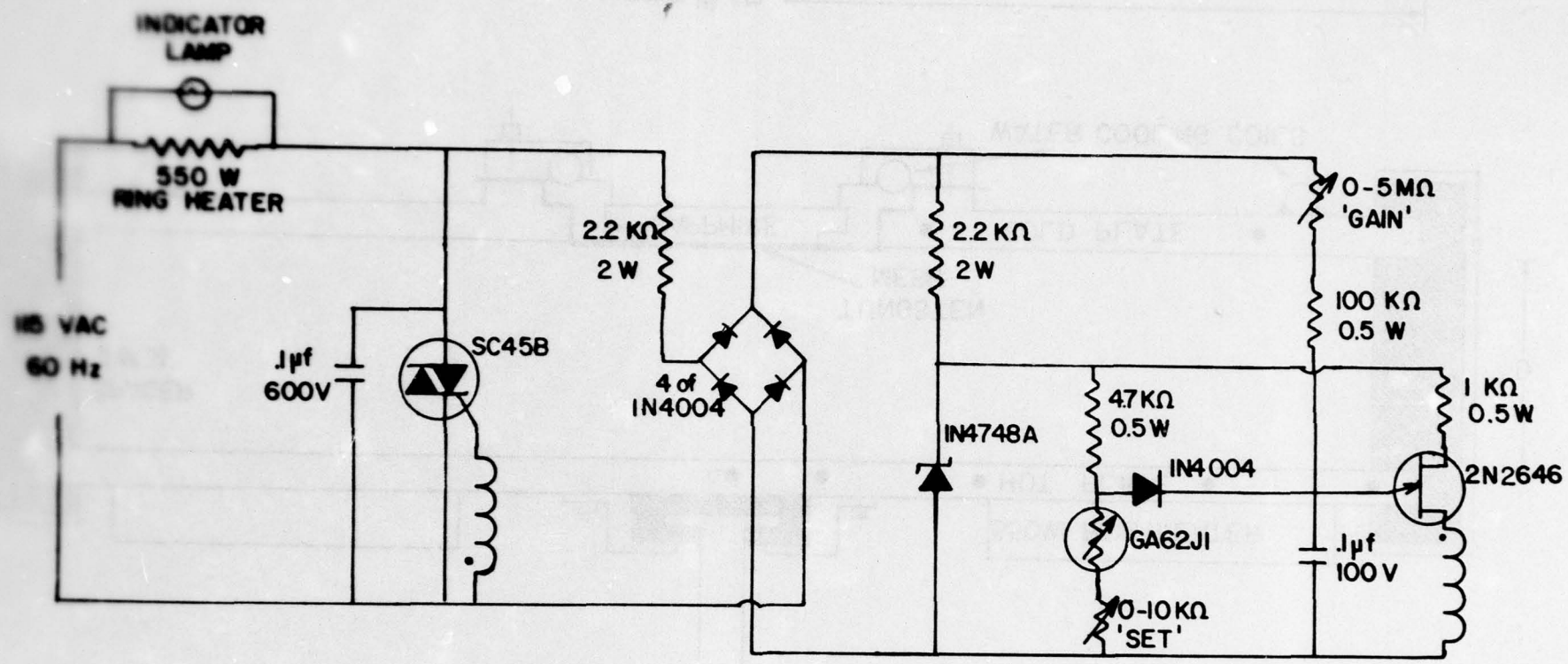
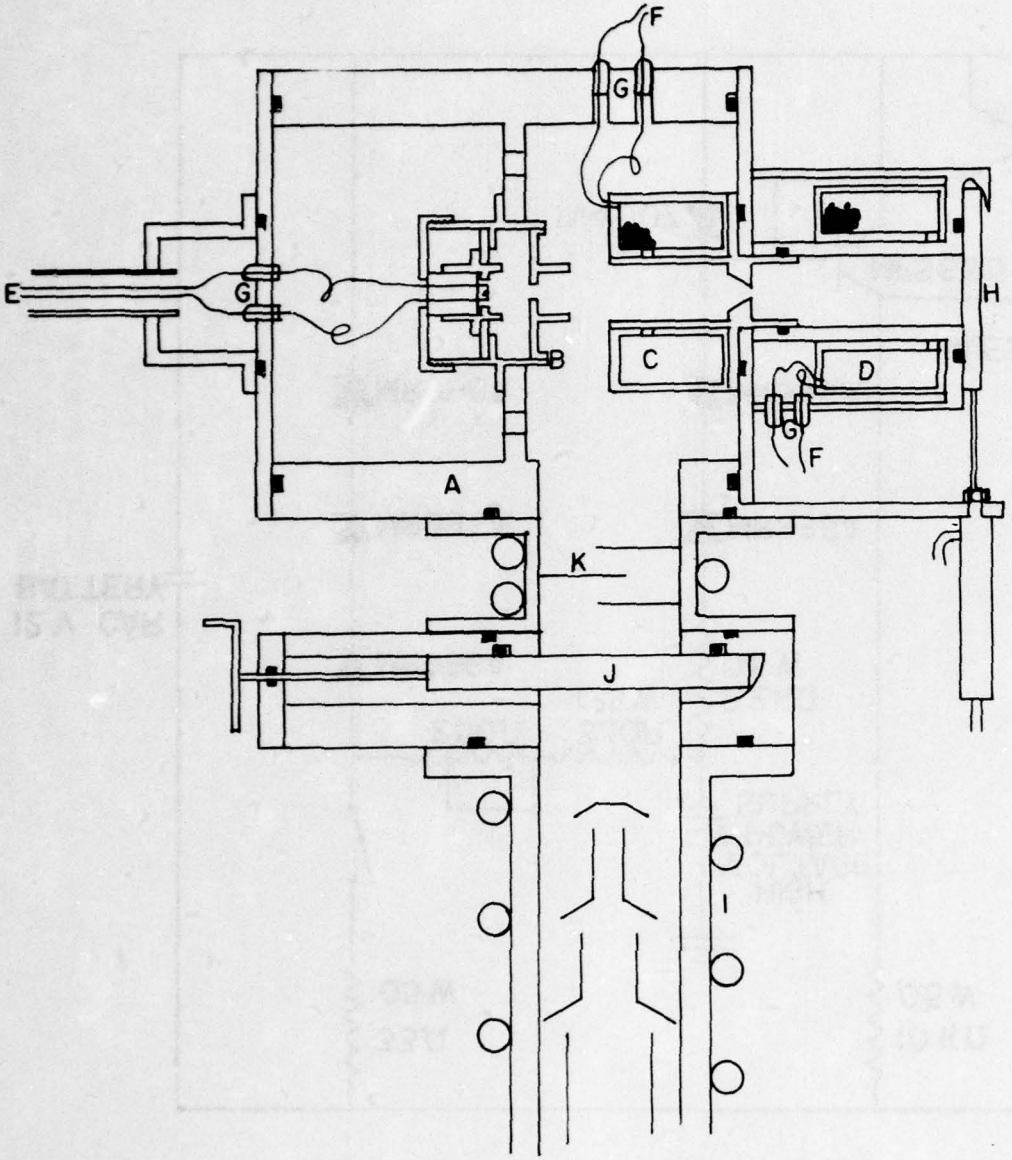


FIG. 4.2.3. HEATER CONTROL CIRCUIT





A: GUN BLOCK
B: EMISSION SECTION
C: INNER LENS
D: OUTER LENS
E: HIGH VOLTAGE LEADS
F: LENS LEADS
G: VACUUM FEEDTHROUGHS
H: PNEUMATICALLY ACTUATED DOOR
I: DIFFUSION PUMP
J: ISOLATION VALVE
K: WATER COOLED TRAP
L: RAZOR BLADE TRAP

FIG. 4.3.1. ELECTRON GUN & PUMPING SYSTEM SCHEMATIC

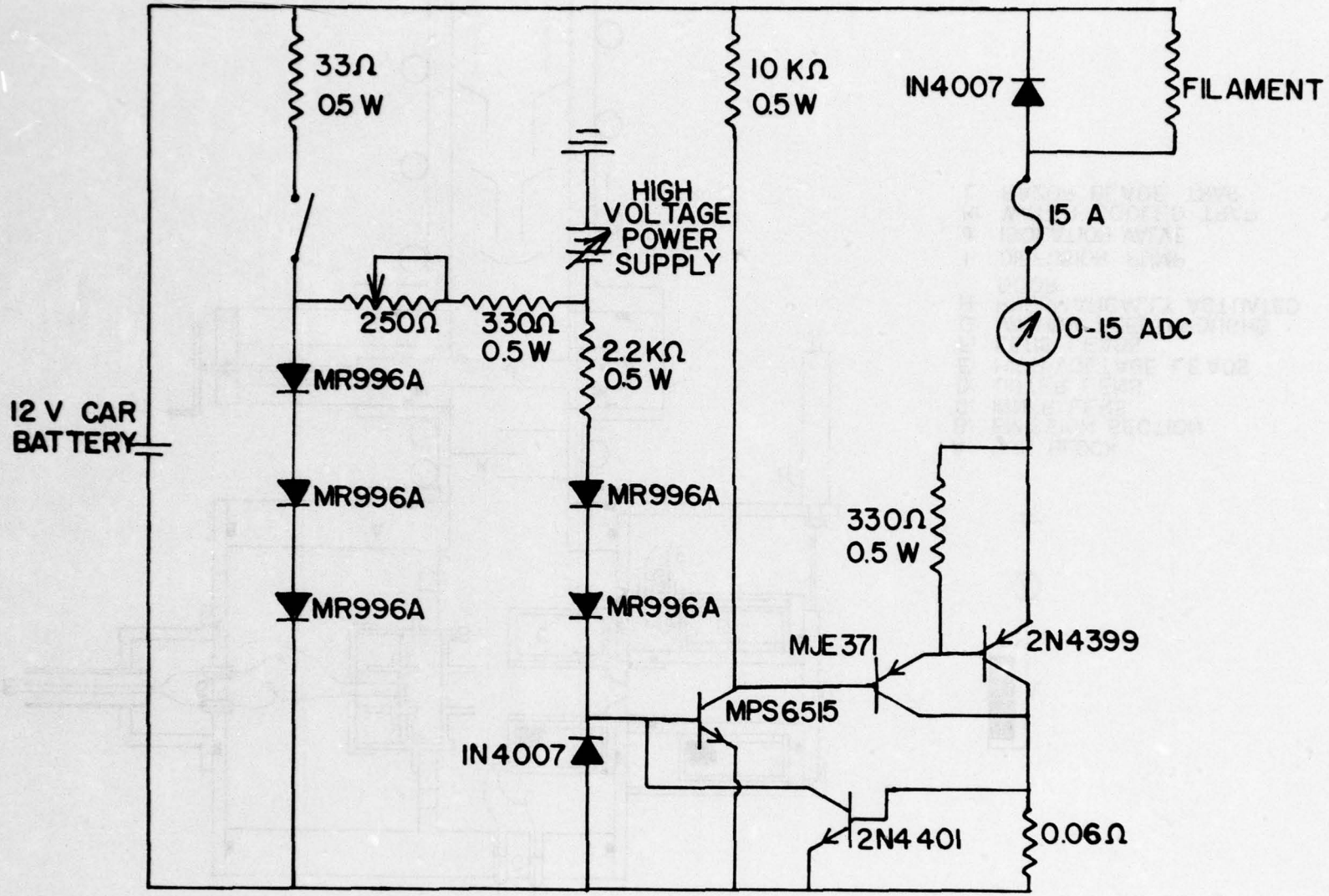


FIG. 4.3.2. ELECTRON GUN EMISSION CURRENT REGULATOR

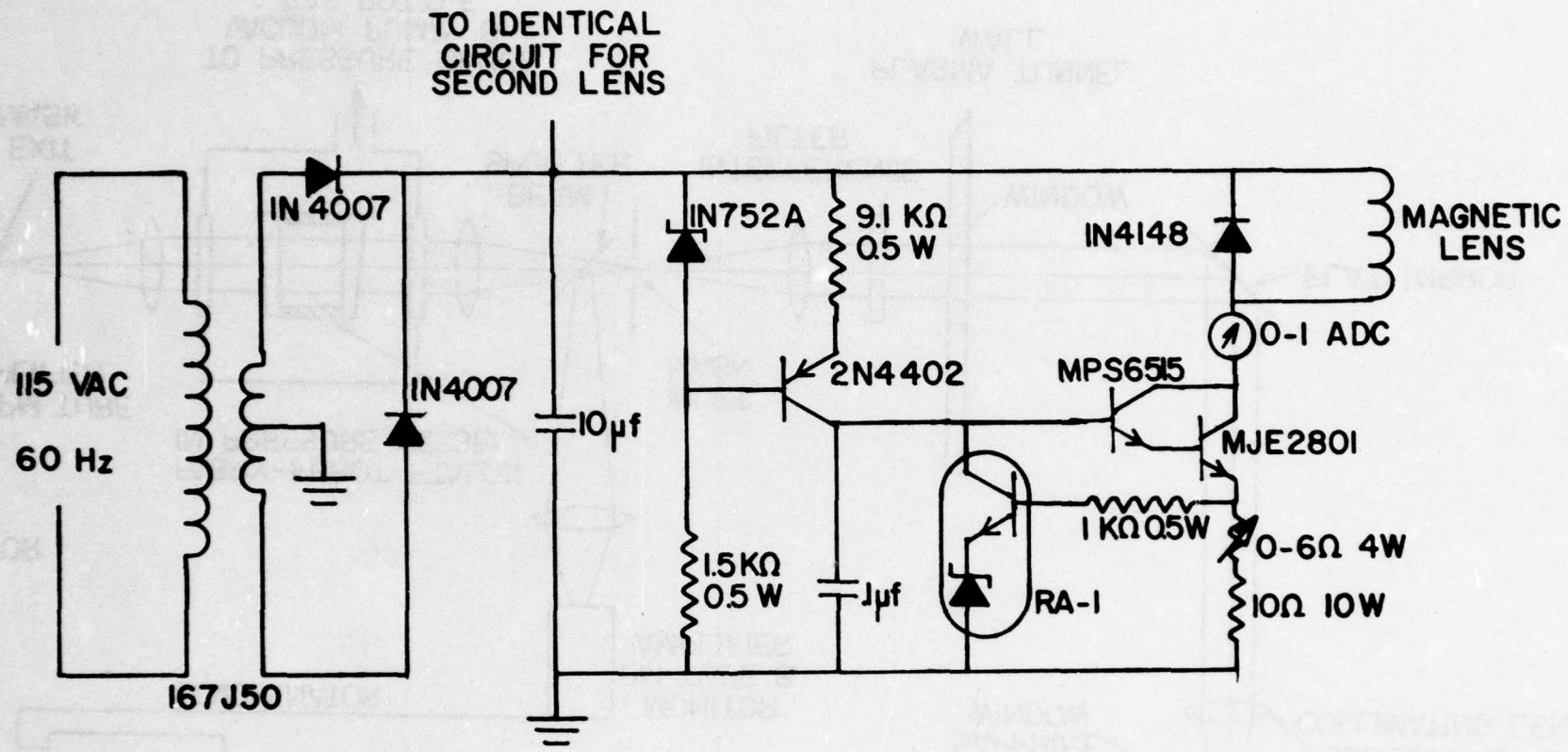


FIG. 4.33. MAGNETIC LENS POWER SUPPLY

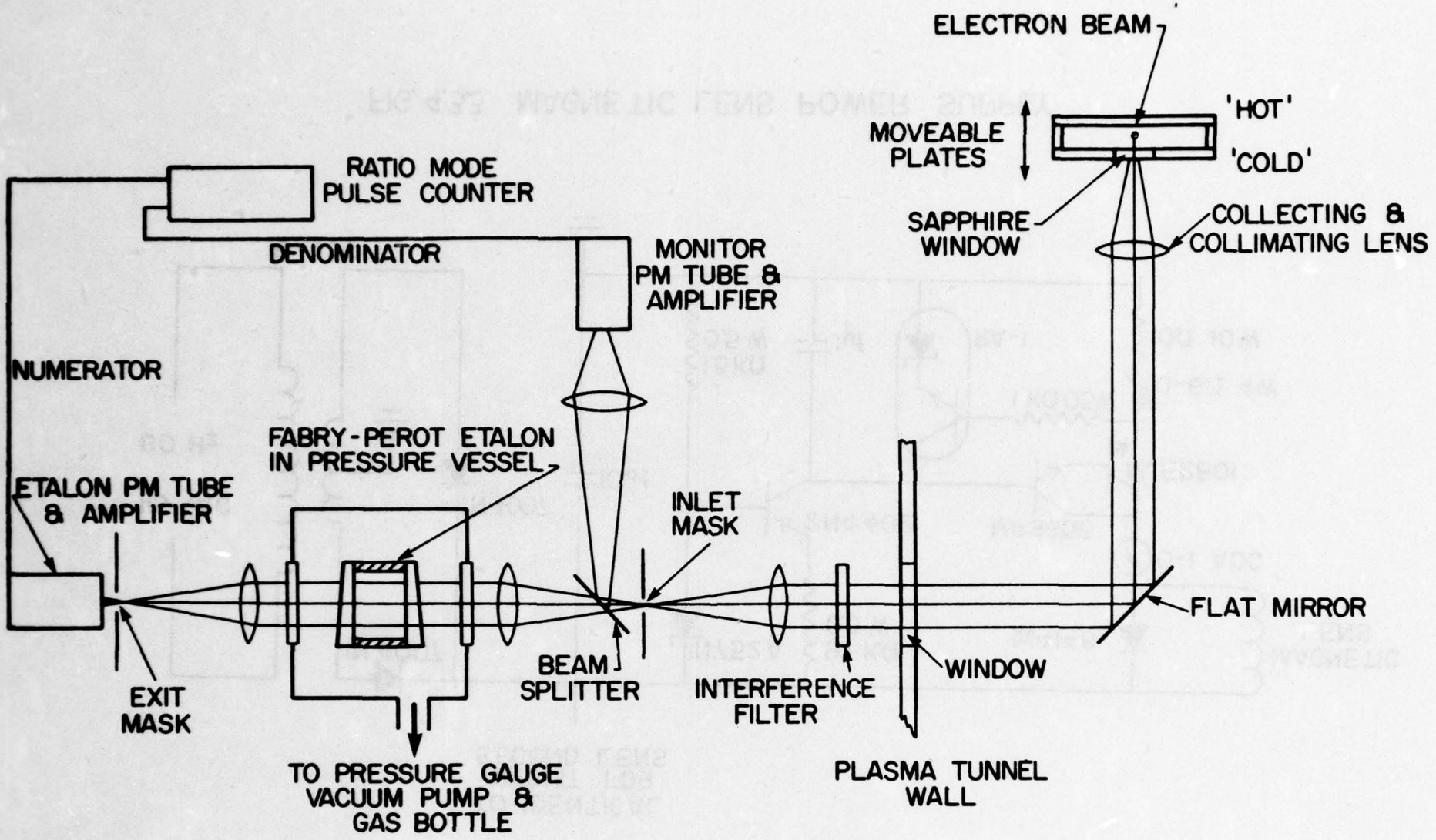


FIG.4.4.1 SCHEMATIC OF EXPERIMENTAL APPARATUS

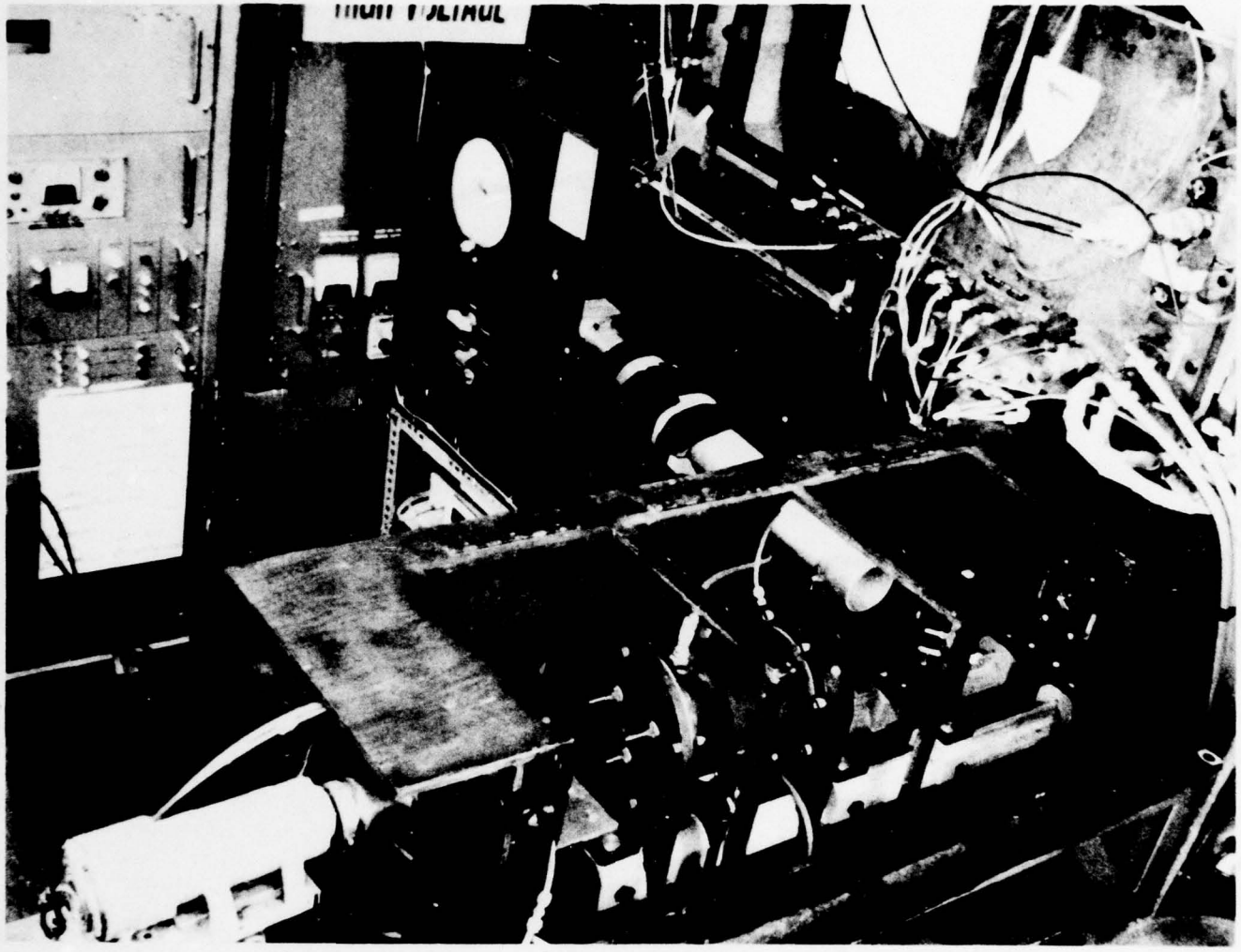


FIG. 4.4.2. THE OPTICAL SYSTEM

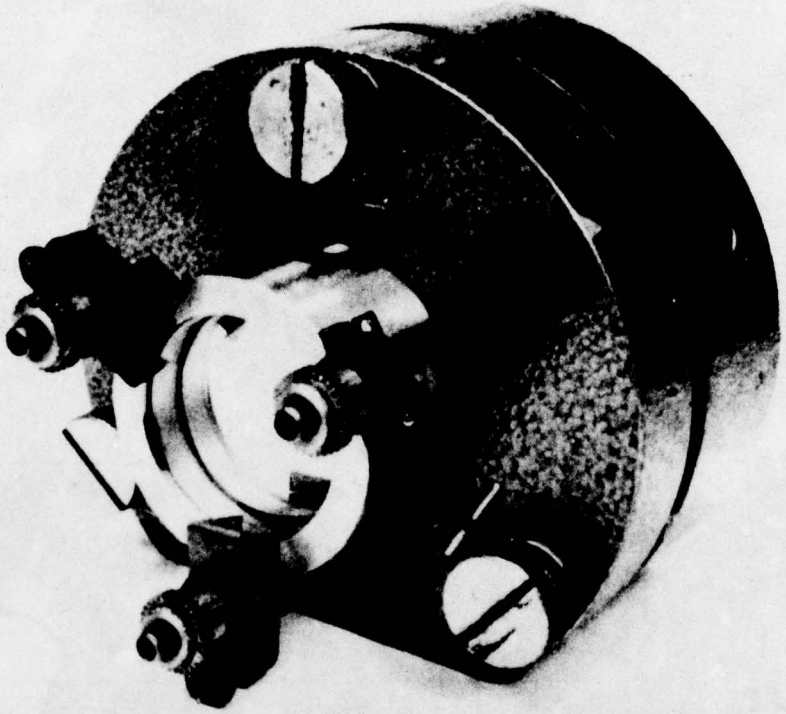


FIG. 4.4.3. THE FABRY-PEROT INTERFEROMETER

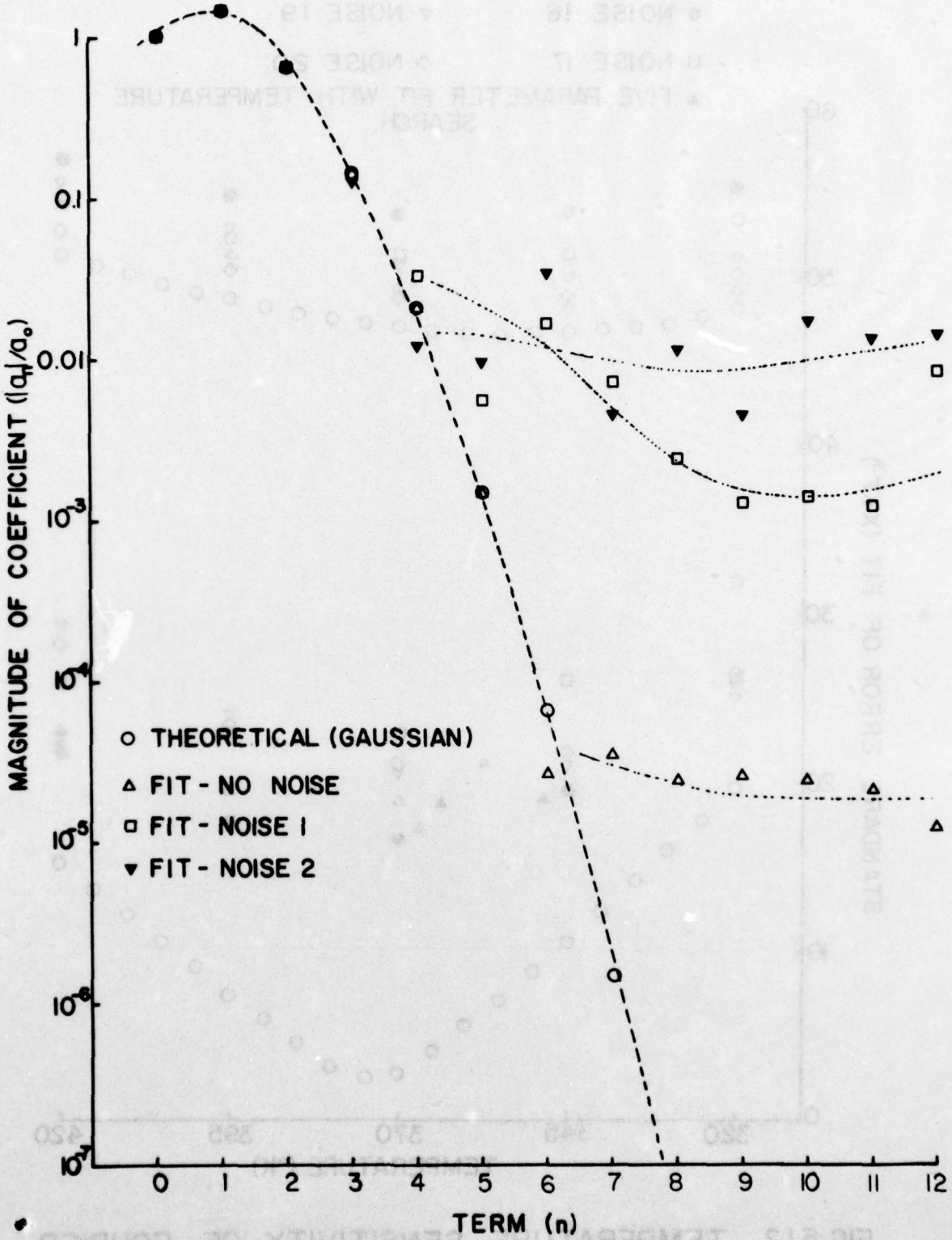


FIG. 5.11. RELATIVE MAGNITUDE OF FOURIER COEFFICIENTS

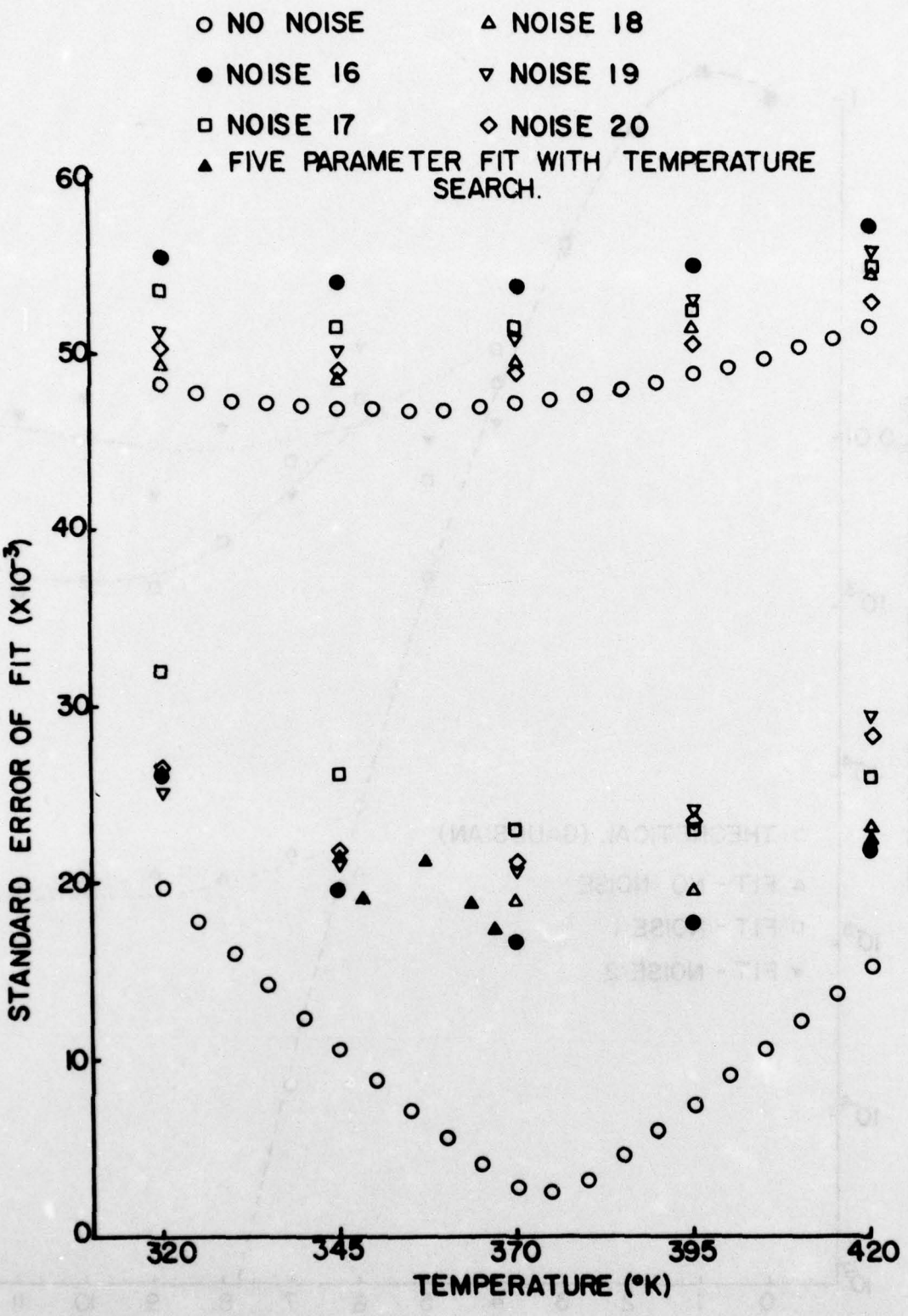


FIG.5.1.2. TEMPERATURE SENSITIVITY OF FOURIER SERIES FIT

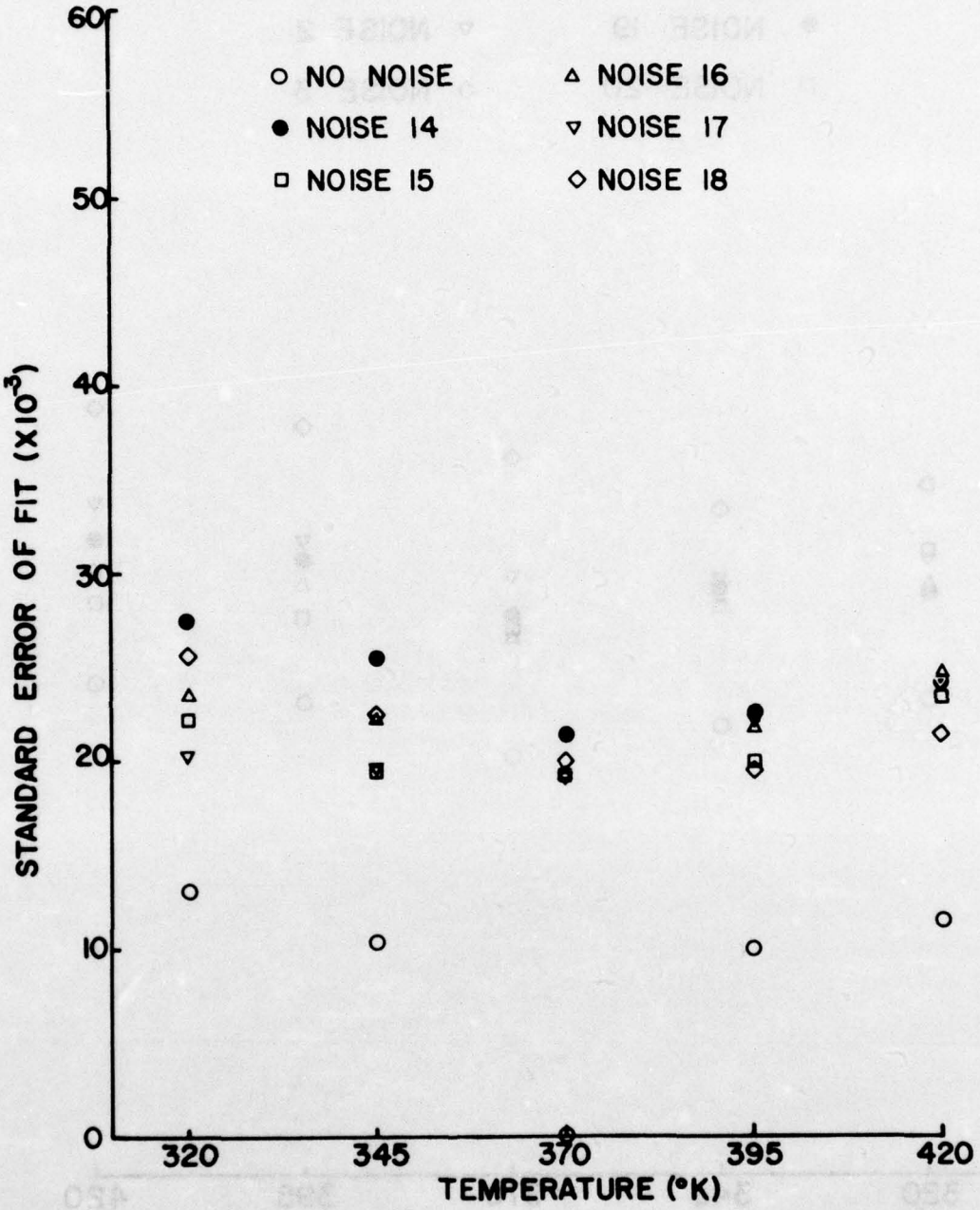


FIG. 5.1.3(a). FIT OF A MAXWELLIAN TO A MAXWELLIAN

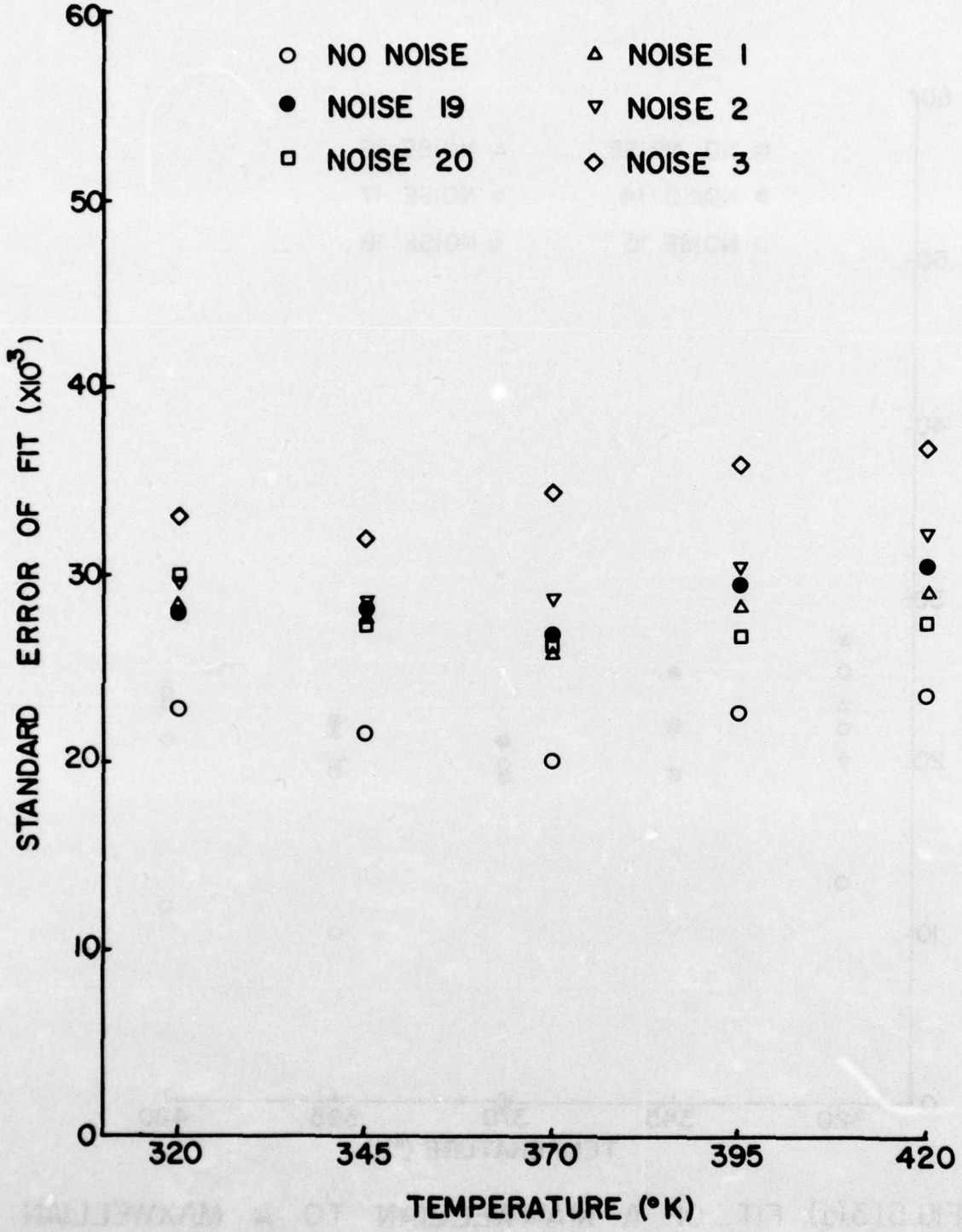


FIG.5.1.3(b). FIT OF A MAXWELLIAN TO A BIMODAL DISTRIBUTION, T_{RAT} =0.8

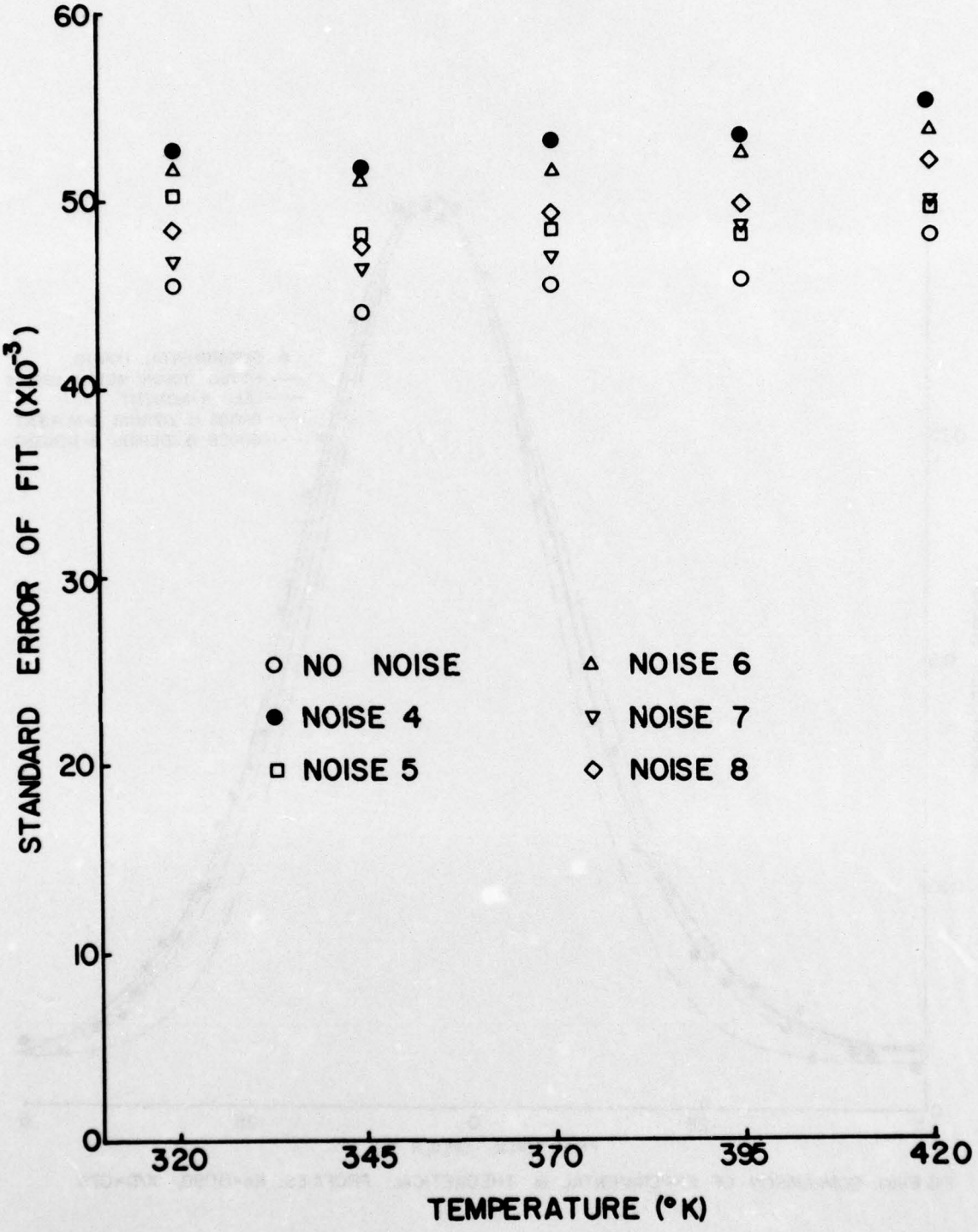


FIG.5.1.3(c). FIT OF A MAXWELLIAN TO A BIMODAL DISTRIBUTION, T_{RAT} =0.6

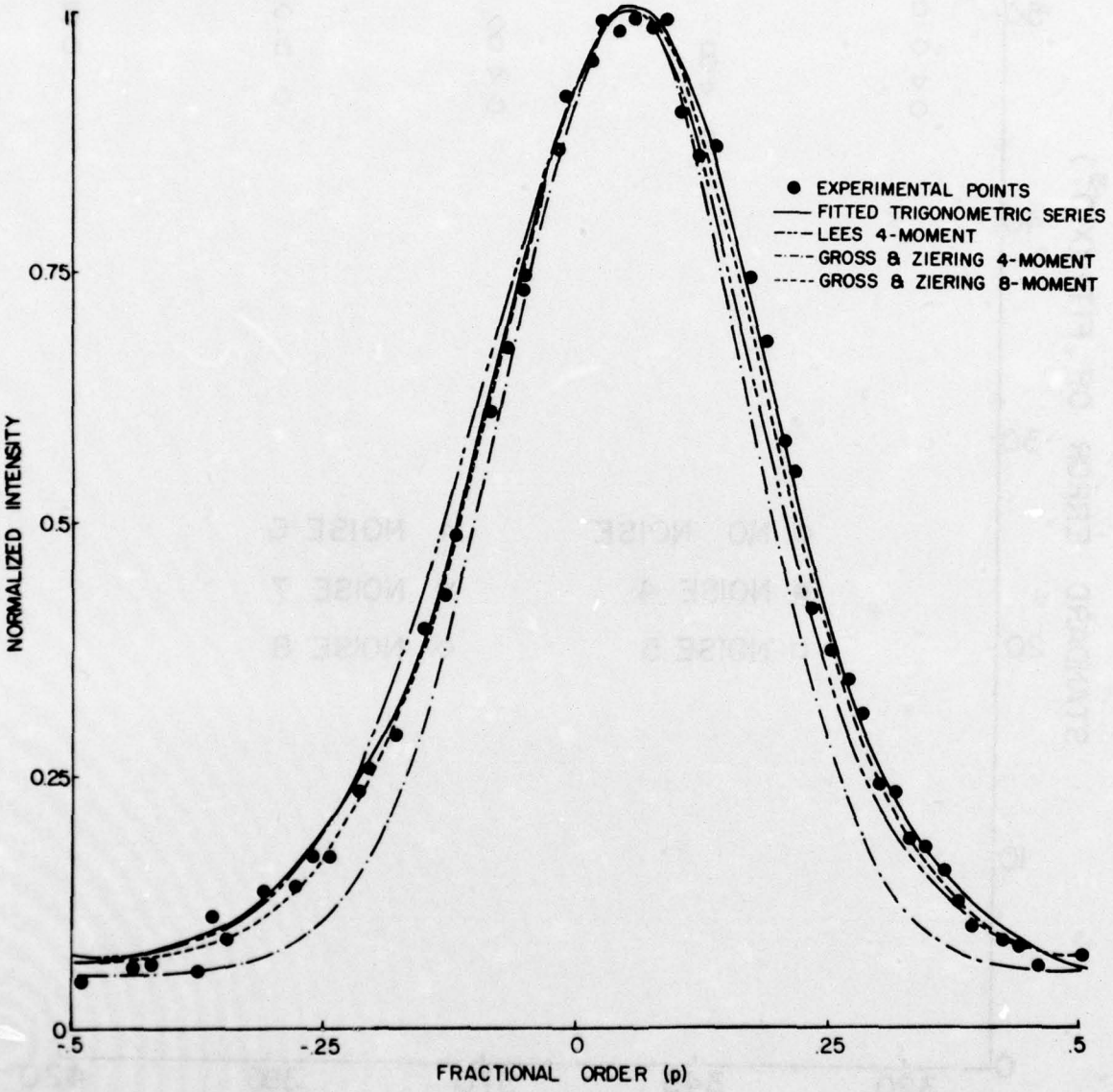


FIG. 6.11(a). COMPARISON OF EXPERIMENTAL & THEORETICAL PROFILES, Kn=0.098, X/D=0.75

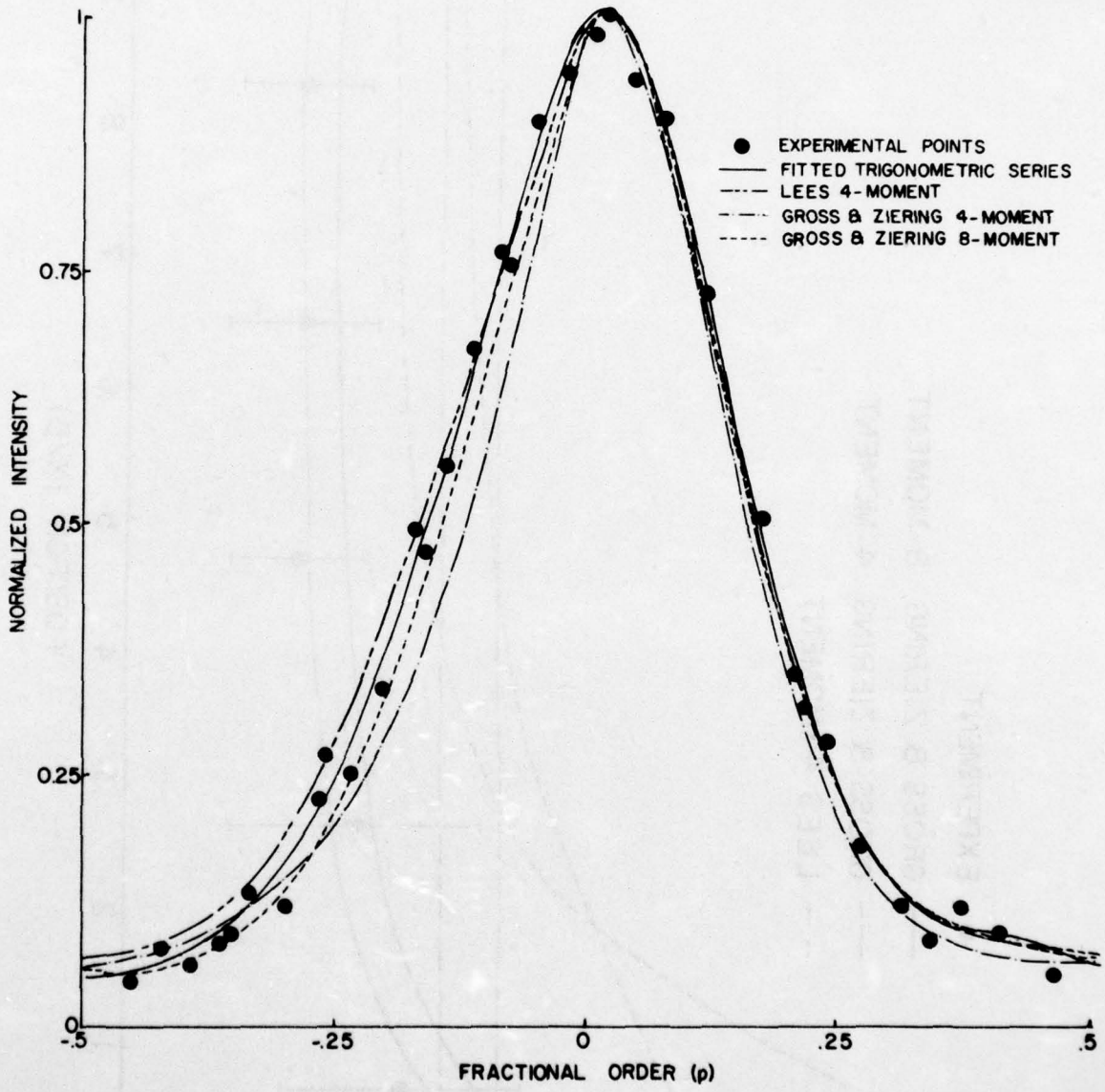
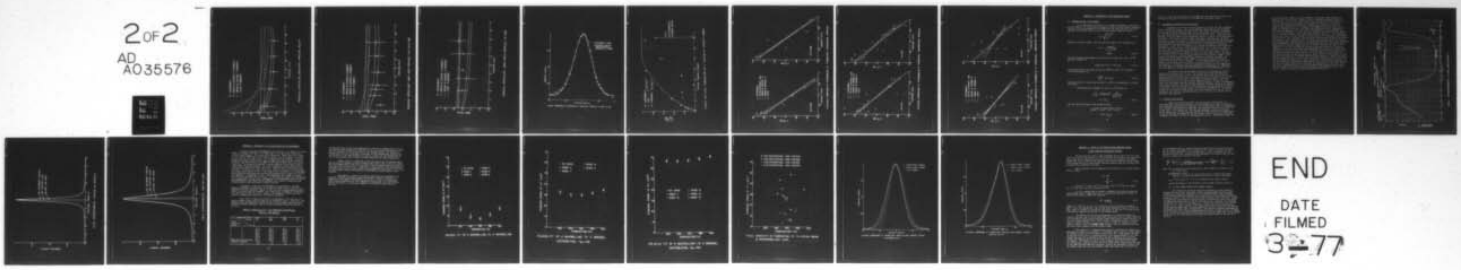


FIG. 6.1.1(b). COMPARISON OF EXPERIMENTAL & THEORETICAL PROFILES, Kn=0.83, X/D =0.7

AD-A035 576 TORONTO UNIV (ONTARIO) INST FOR AEROSPACE STUDIES F/G 20/13
AN EXPERIMENTAL INVESTIGATION OF THE DISTRIBUTION FUNCTION FOR --ETC(U)
DEC 76 D T TONG AF-AFOSR-2091-71
UNCLASSIFIED UTIAS-210 AFOSR-TR-77-0060 NL

2 OF 2
AD A035576



END
DATE FILMED
3-77

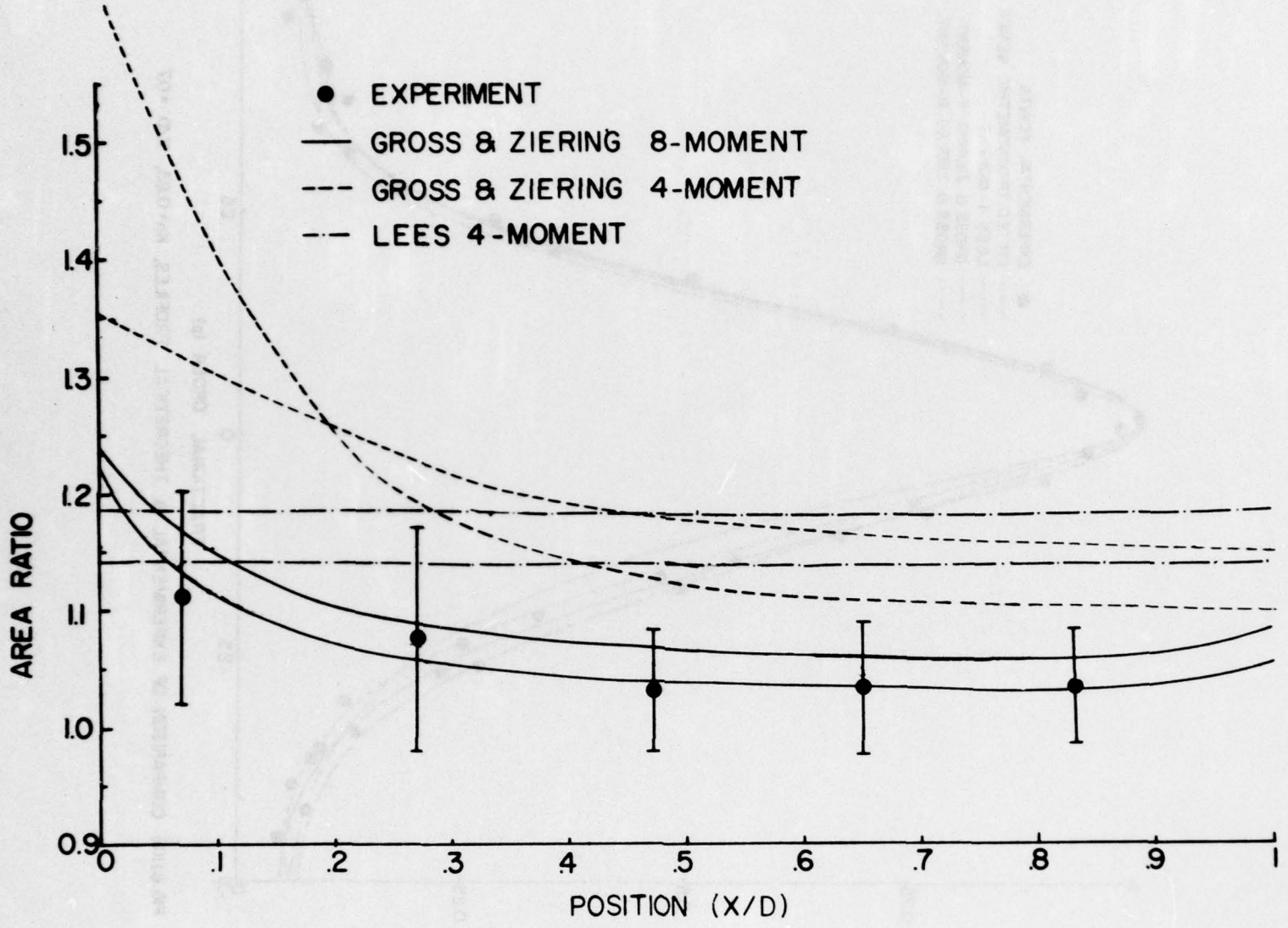


FIG.6.1.2 (a). INTER-PLATE AREA RATIO PROFILES, $Kn \leqslant 0.21$

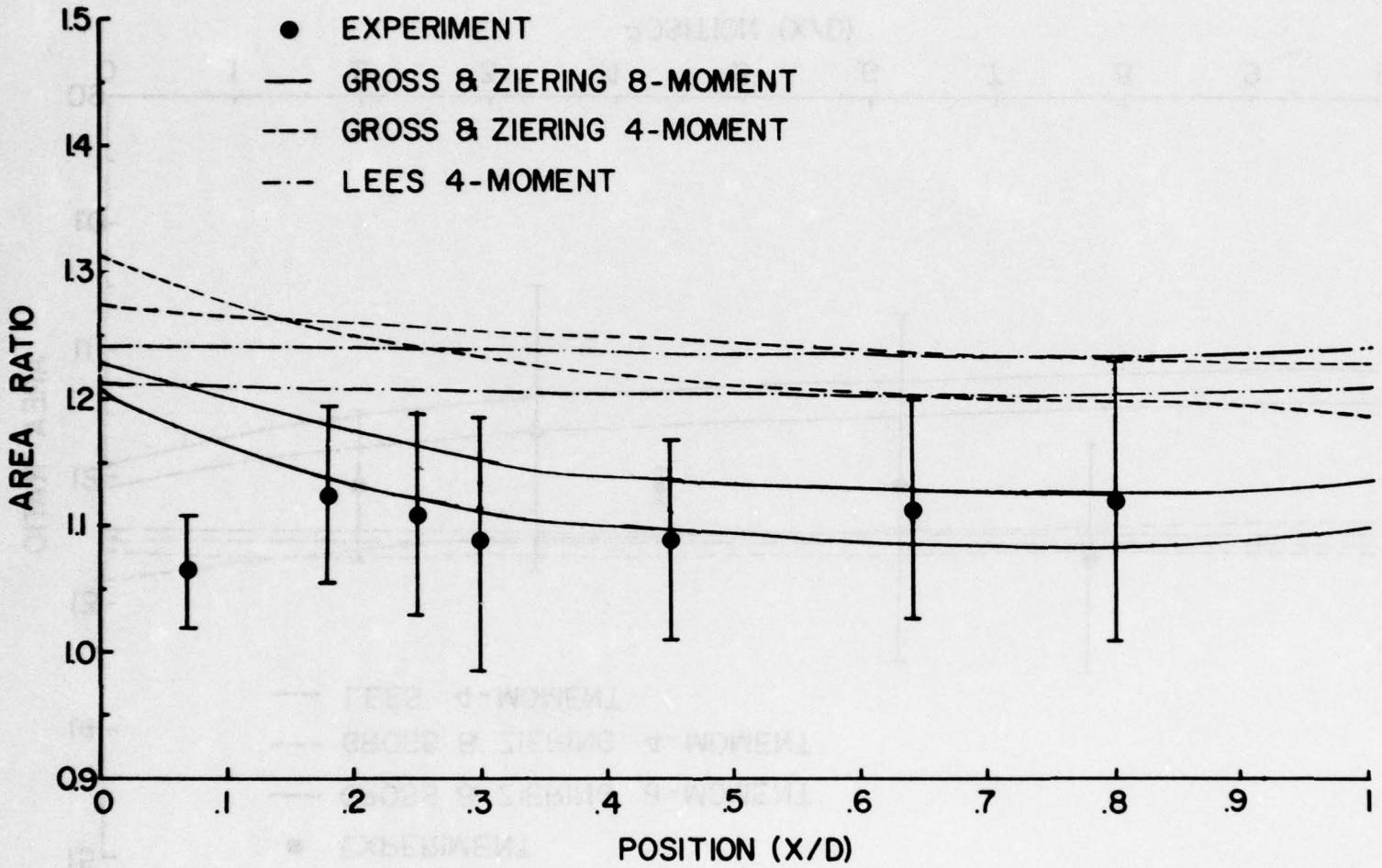


FIG.6.1.2(b). INTER-PLATE AREA RATIO PROFILES, $0.21 < Kn \leq 0.85$

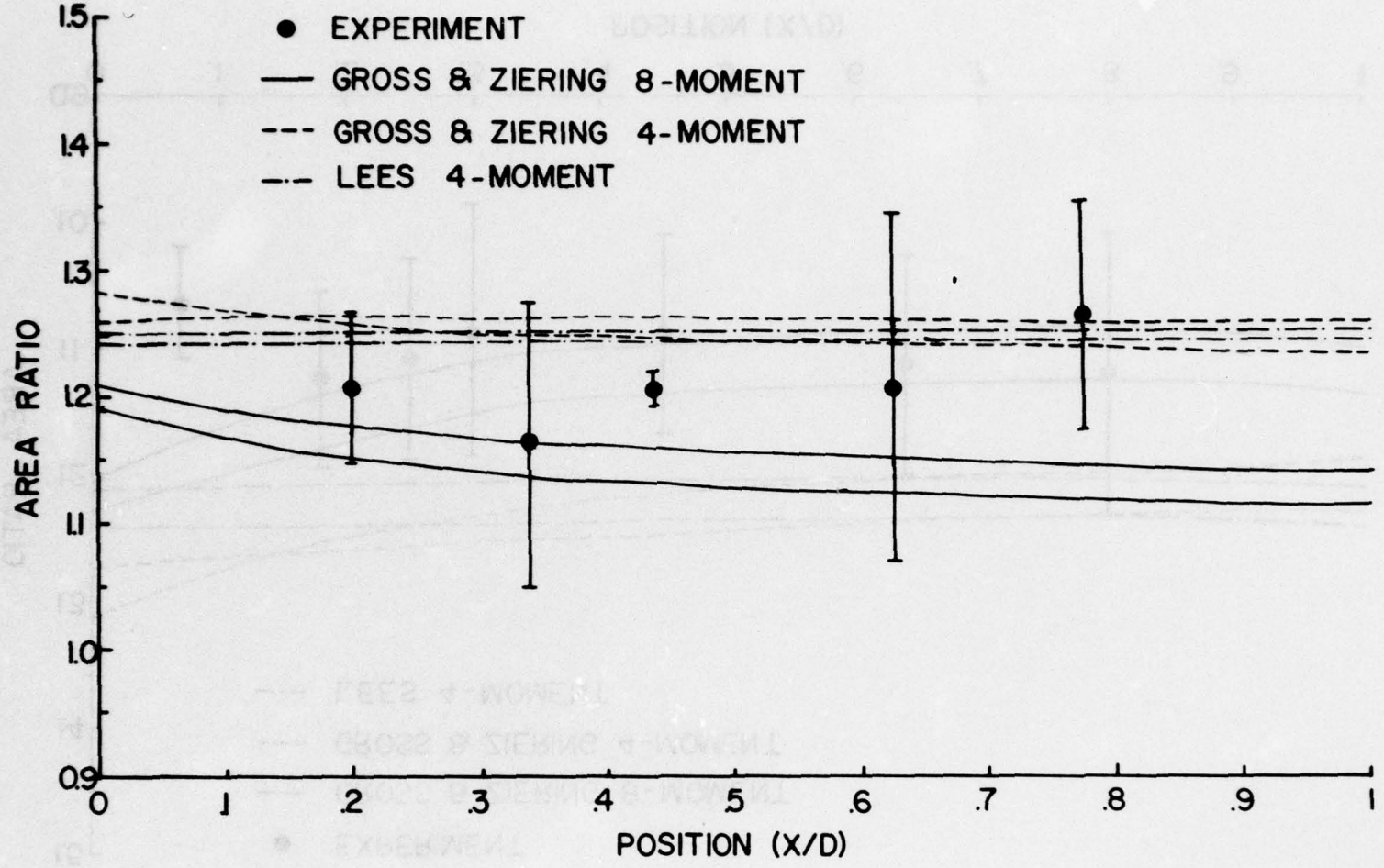


FIG.6.1.2(c). INTER-PLATE AREA RATIO PROFILES, Kn > 0.85

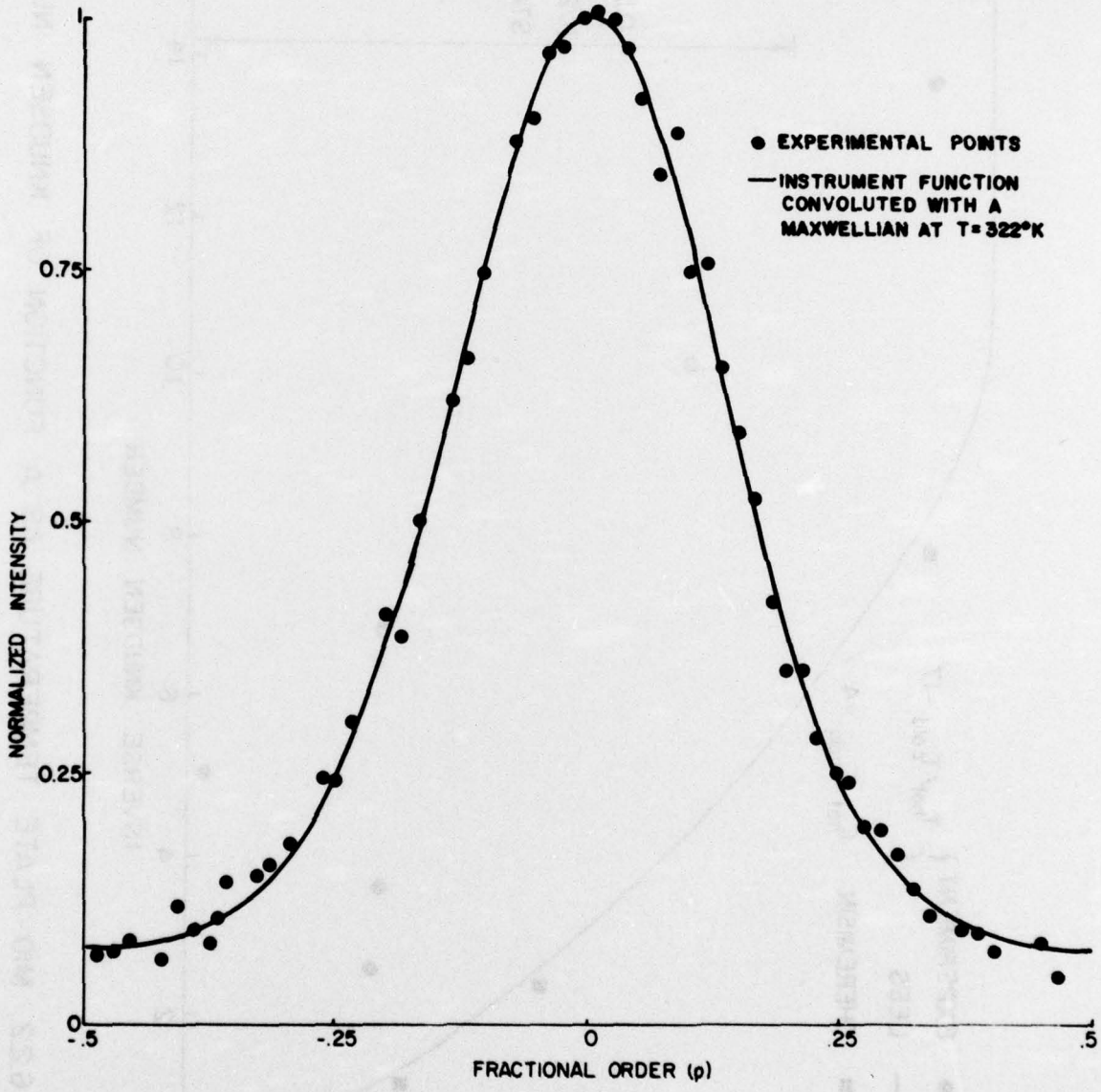


FIG. 6.2.1 COMPARISON OF EXPERIMENTAL & THEORETICAL PROFILES, Kn = 0.098, X/D = 0.75

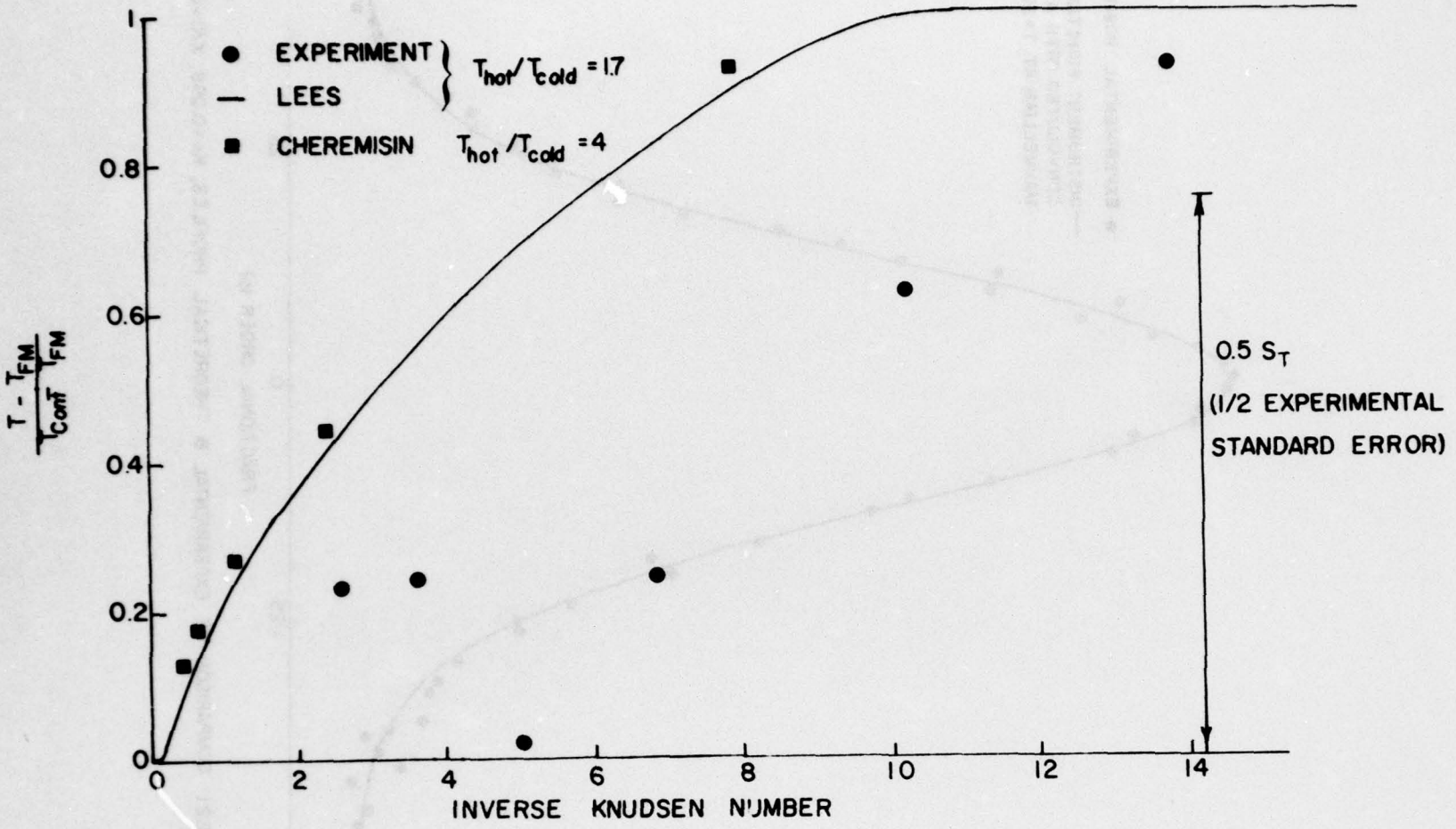


FIG.6.2.2. MID-PLATE TEMPERATURE AS A FUNCTION OF KNUDSEN NUMBER

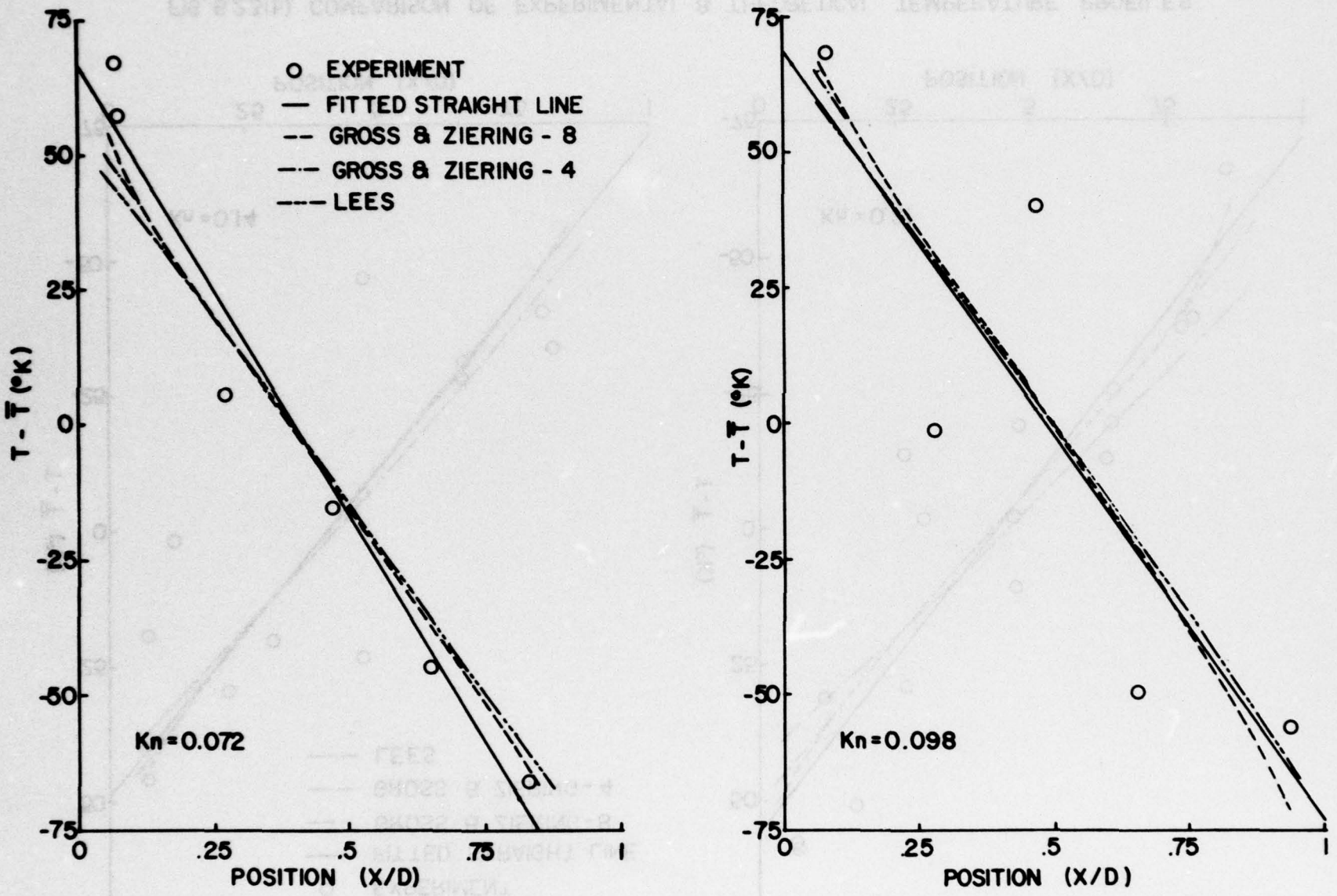


FIG. 6.2.3(a). COMPARISON OF EXPERIMENTAL & THEORETICAL TEMPERATURE PROFILES

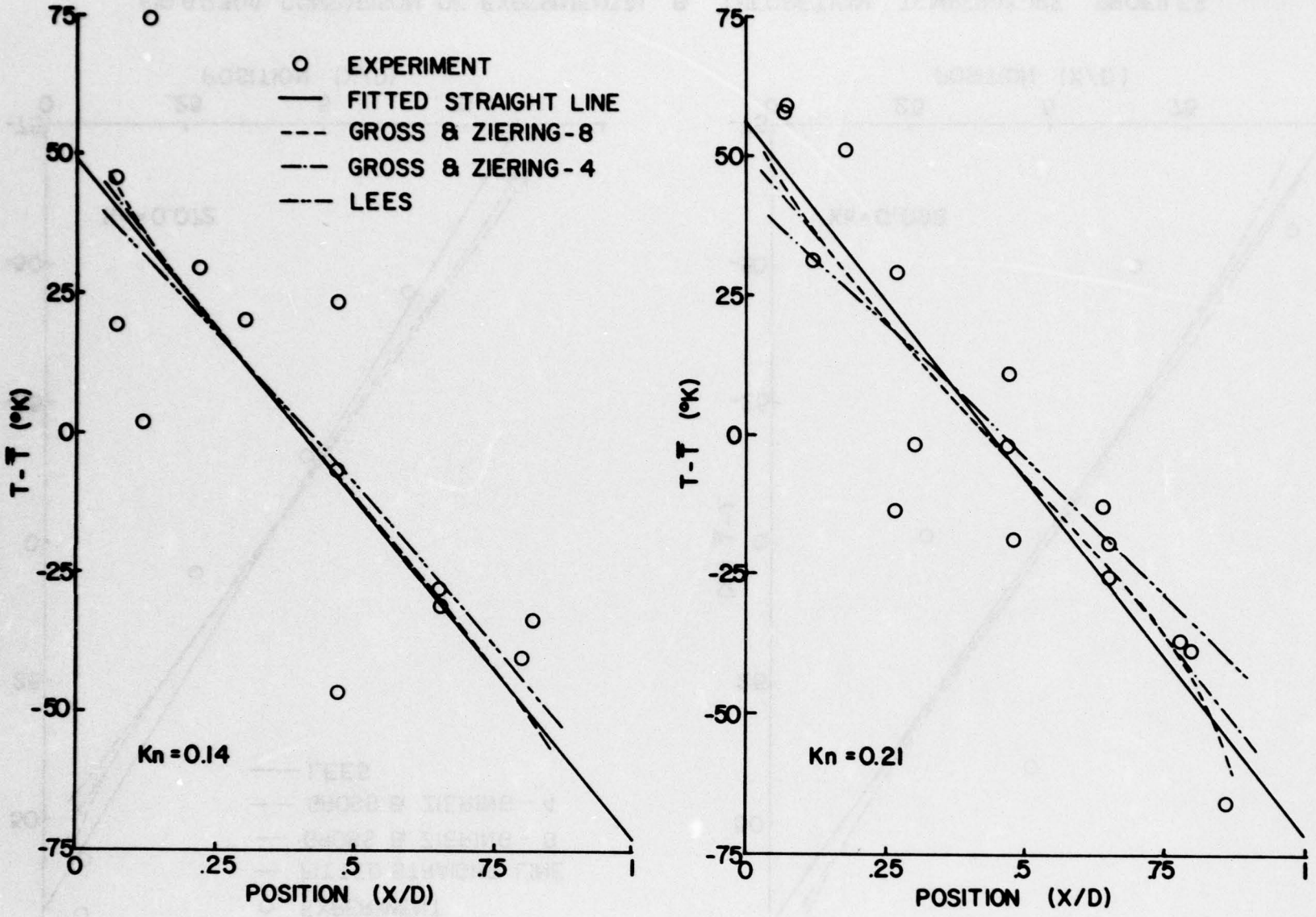


FIG. 6.2.3(b). COMPARISON OF EXPERIMENTAL & THEORETICAL TEMPERATURE PROFILES

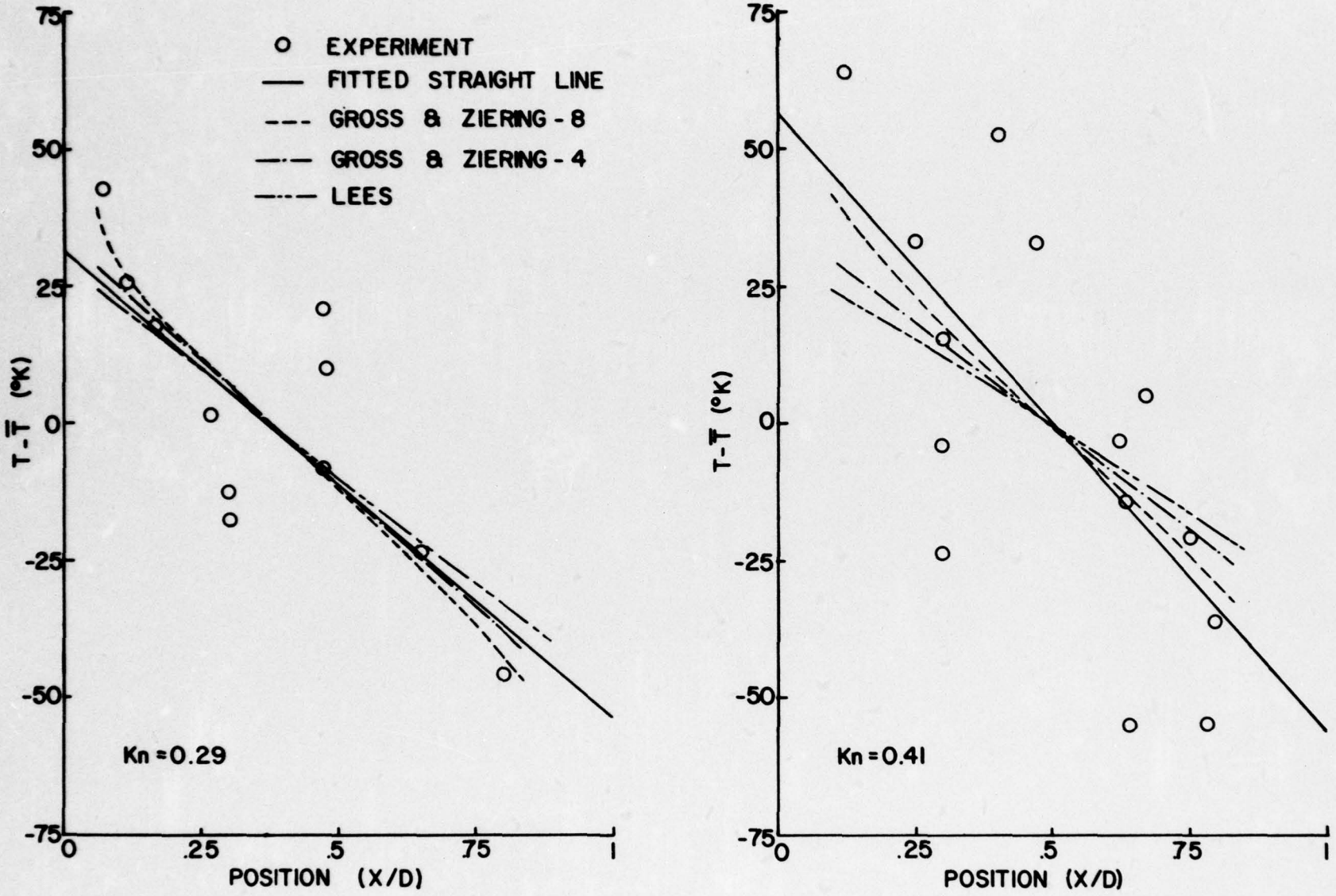


FIG. 6.23(c). COMPARISON OF EXPERIMENTAL & THEORETICAL TEMPERATURE PROFILES

APPENDIX A - CALIBRATION OF THE FABRY-PEROT SYSTEM

A.1 Nominal Finesse of the System

In evaluating the net finesse of a system of components, each having its own finesse, the conventional assumption is that each individual transmission function can be approximated by a Gaussian with the same half-width (and hence finesse), so that the finesses add as inverse squares using the formula:

$$F_{net} = \sqrt{\sum_i F_i^{-2}}^{-1} \qquad (A.1.1)$$

With the 3 cm etalon spacer, the free spectral range of the instrument was

$$\langle \Delta\lambda \rangle = \frac{4609.6^2}{2 \times 3 \times 10^8}$$

$$= .0354\text{Å} \qquad (A.1.2)$$

The total-width-at-half-height of the natural line shape was 1.025×10^{-4}Å, giving a 'finesse' of

$$.0354/1.025 \times 10^{-4} = 345\ (F_N) \qquad (A.1.3)$$

The reflectivity of the plates was 90% at 4609Å (see Fig. A.1) yielding a reflectivity finesse of:

$$\frac{\pi\sqrt{.9}}{.1} = 29.8\ (F_R) \qquad (A.1.4)$$

The first surface of each plate was flat to $\lambda/100$, corresponding to a finesse of 50 (F_I).

The pinhole had a diameter of .012", so its finesse was

$$\frac{\lambda}{h}\frac{f^2}{r^2} = \frac{4.609 \times 10^{-5}}{3}\ \frac{250^2}{(6/39.37)^2}$$

$$= 41.3\ (F_P) \qquad (A.1.5)$$

The net expected finesse of the system was thus:

$$\sqrt{345^{-2} + 29.8^{-2} + 50^{-2} + 41.3^{-2}}^{-1}$$

$$= 21.7\ (F_{net}) \qquad (A.1.1a$$

Figure A.2 shows the natural and Airy functions and the convolution of these with the pinhole and flatness functions to give the net instrument function.

A.2 Alignment and Calibration of the System

Alignment of the entire optical system was critical not only to maintain proper focusing and finesse, but also to minimize vignetting and the consequent loss of some of the already low light level. The system was aligned 'backwards' by removing the signal photomultiplier tube and shining a laser through the pinhole and along the optical axis with only the mirrors in place. These were then adjusted so that the beam passed through the location of the electron beam between the plates. The lenses were then added sequentially, starting with the final focusing one, and were aligned by positioning them so that the beam passed through the centre and the reflections from each surface of the lens passed directly back along the beam. The axial placement of the lens was determined initially by measurement. After the inlet mask was in place the positioning of the lenses was checked by placing a mirror on the 'parallel light' side of each and a lamp on the 'far' side of the pinhole corresponding to that lens, and fine tuning until the reflected image of the pinhole was in focus at the object plane. Because the interference filter was removed to allow the total light to enter the system for a visual check of electron beam position after each filament change, it was mounted in a guide which automatically realigned it normal to the beam. The interferometer was mounted in its chamber in such a way that both the plate parallelism and axis could be changed. It was initially aligned to give clear fringes, and then the axis was adjusted to locate the pattern centre on the final pinhole. The monitor system was aligned by placing a mercury lamp behind the inlet mask and adjusting the beam-splitter/lens/photomultiplier combination until the image was focused onto the photocathode of the photomultiplier tube.

Adjustment of the interferometer plates for parallelism was done by placing a mercury lamp in front of the recollimating lens and diffusing the light with an etched acrylic screen. The fringes were viewed by eye and the springs adjusted until there was no variation in the pattern when viewed through different portions of the plates. The actual operating parameters were then determined by a series of scans of known Doppler profiles. The hot and cold plates were moved away from the electron beam and profiles in static room temperature argon were taken. The data were then analyzed to obtain the value of effective reflectivity which best matched the convoluted instrument and Maxwellian profiles to the data. This process was repeated at intervals throughout the experimental program and the value so obtained was 0.76 with a standard error of .01, corresponding to an effective reflectivity finesse of 11.4 and a net finesse of 10.7, much lower than expected.

A.3 Source of Low Finesse

Both piezo-electrically (Ref. 32) and pressure scanned (Ref. 52) instruments have operated at finesses close to theoretical, so the low value for this instrument was definitely anomalous. The interferometer flats were guaranteed by a reputable manufacturer over the full clear aperture, and thus were ruled out as the cause. It is known (Ref. 56) that the adjustment springs can locally distort the plates, and this was thus assumed to be the source of the degradation. It was checked out by masking all but the central 6 mm dia. portion of the interferometer and taking a series of room-temperature traces. The physical layout of

the interferometer chamber required alignment of the plates after masking, so that only the central portion could be used for checking adjustment, with the resultant loss of accuracy. Despite this, the found effective reflectivity was 0.87, corresponding to instrument and net system finesses of 22.5 and 18.4, respectively, confirming the suspicion. Whether the distortion arose from design or manufacturing error is unknown, but masking lowered the signal level below an acceptable value and, since the total system finesse was repeatable at full plate illumination, the lower finesse configuration of the instrument was used for all experiments. Because the exact nature of the distortion was unknown, it was necessary to model it in some fashion for data reduction. Three different models were chosen; an Airy function of reflectivity 0.76, a Gaussian representing random defects, and a quadratic function representing non-parallelism of the plates. The latter two were scaled to give a net finesse of 11.4 when convoluted with an Airy function with reflectivity 0.9. All three instrument functions were convoluted with distributions predicted by the Lees four-moment and Gross and Ziering eight-moment models at Knudsen numbers below 0.5, and the resultant area-ratios were compared. It was observed that the two defect functions predicted 13% greater asymmetry for the Lees model than the eight-moment one, but the low finesse Airy function predicted only a 9% difference. Even this latter value was greater than the expected variation in the area ratio for noisy data, and consequently the instrument function was modelled by the low finesse Airy function, because it was the most conservative in its differentiation between theories. Maxwellian distribution functions at 300°K and 500°K were convoluted with the two defect functions, and the resultant profiles were analyzed using the low finesse Airy function. It was found that the 'experimental' temperatures were correct at 300°K, but that the analysis over-stated the spread between the two temperatures by 5%, which corresponds to a maximum difference in the experimental temperature gradient of only 4%, which still leaves the experimental and theoretical gradients of the same order. Figure A.3 shows the actual instrument function used.

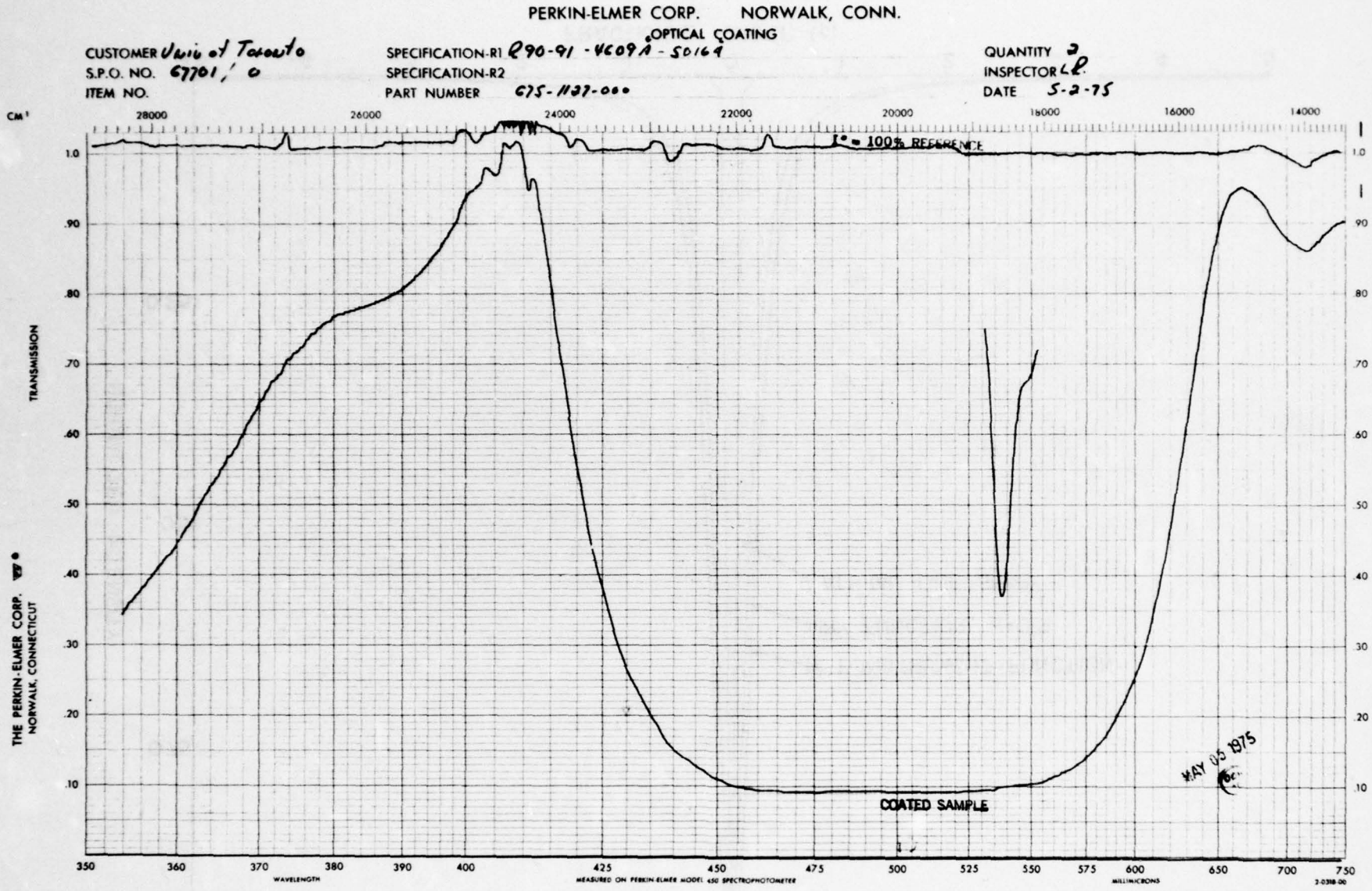


FIG. A.I. INTERFEROMETER PLATE REFLECTIVITY

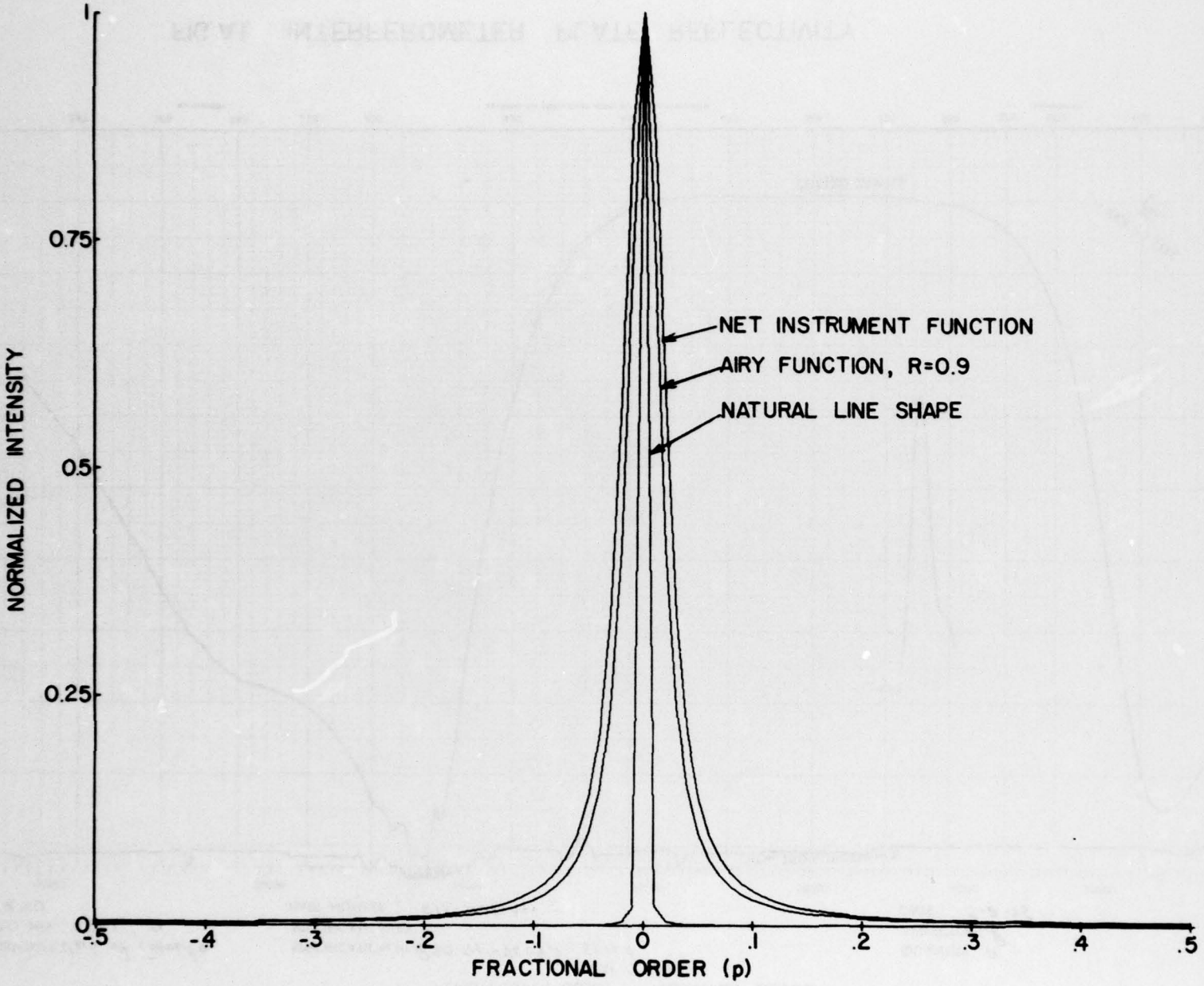


FIG.A.2. INTERFEROMETER FUNCTION AS SPECIFIED

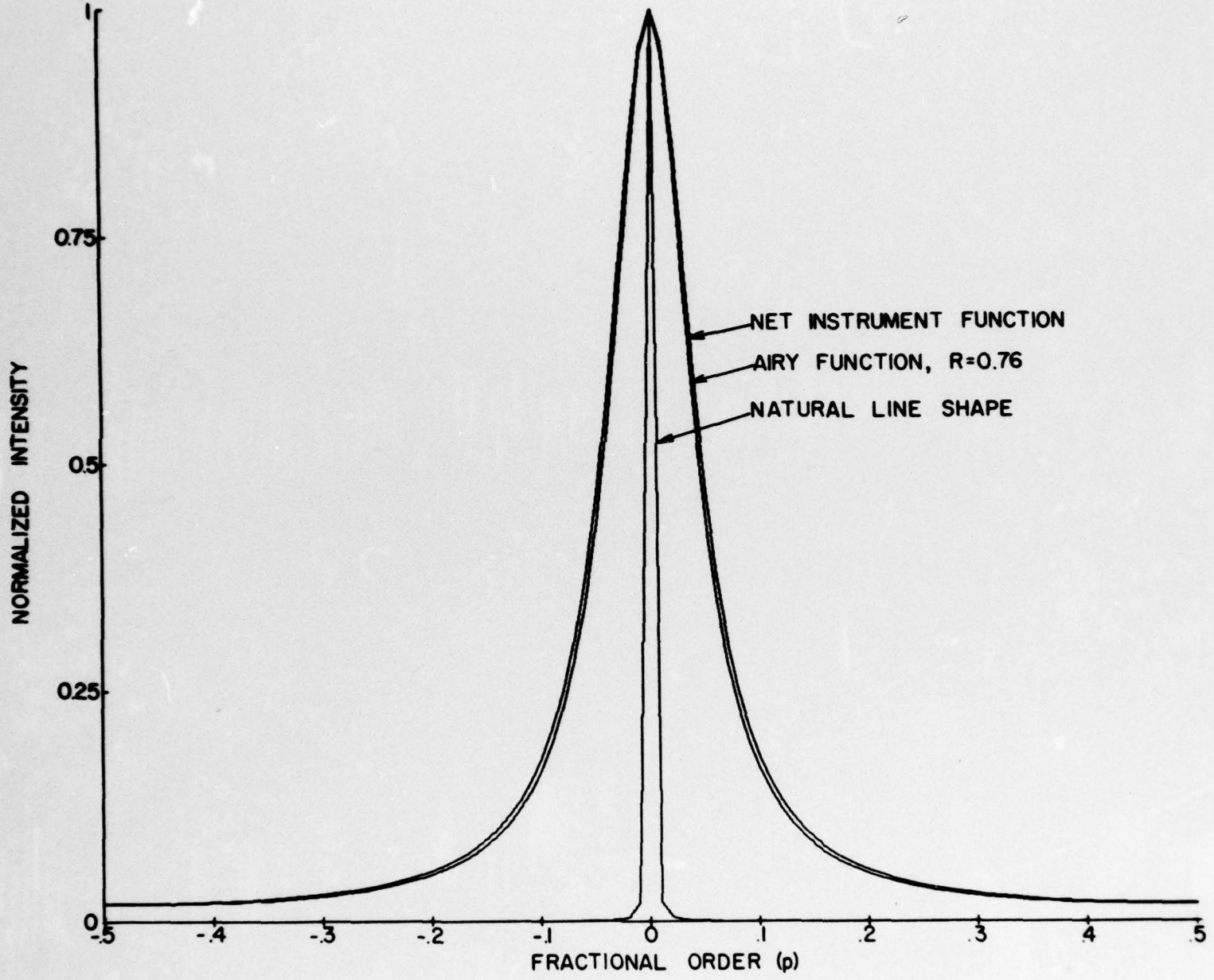


FIG.A.3. INTERFEROMETER FUNCTION USED

APPENDIX B - APPLICATION OF A HIGHER RESOLUTION INTERFEROMETER

Because of the high experimental error relative to the difference between models, an analysis was made of the improvements to be gained by raising the overall system quality. Two factors were considered: signal level and finesse. In recent years commercial interferometers having twice the diameter and higher finesse than the instrument used in this study have become available. They are piezo-electrically scanned devices and, although they require better vibration isolation than fixed etalons, are immune to the type of plate distortion encountered here. For purposes of analysis a system composed of $\lambda/150$ plates with a reflectivity of 94% was assumed. The total transmission factor would be 94% if scattering and absorption losses were 0.2%. Combining this interferometer with a pinhole of finesse 40 and the spectral line with its finesse of 345 would give an overall system figure of 28.7. The signal levels encountered in the experiment were represented by an observed intensity distribution with a peak count of 2500 superimposed on a background of 1500. This background was assumed to include both the shift and dark current factors. An optically fast system was represented by a signal peak of 10,000 counts superimposed on the background level of 1500, a signal/background ratio which may be optimistic for studies in argon with its non-zero wings in the distribution function profile.

An analysis of the best fit obtainable was performed for the high finesse-low background system, and the results are shown in Fig. B.1(a) to (c). Comparison with the equivalent figure for the low finesse-high background system (Fig. 5.1.3) shows that the standard error sensitivity to asymmetry is improved, as is the width of the error band. However, the sharpness of the curves with respect to temperature variation is not greatly increased.

Four series of data were produced corresponding to the high and low finesse systems coupled with the high and low background levels. These were then analyzed using the temperature search routine and the average temperature and standard deviation determined, with the results tabulated below; and plotted on Fig. B.2.

TABLE B.1 Statistical Tests for Temperature Determination With Different Systems

Background Level / Finesse / Noise Identification	High Low	Low High	High High	Low Low
0	366.8	378.9	378.9	366.7
1	367.4	379.0	377.8	365.1
2	359.1	376.4	369.8	359.1
3	348.1	373.9	358.0	353.0
4	363.1	377.9	352.6	364.5
5	409.7	390.8	378.3	387.7
Mean Value (Noisy data)	369.5	380.2	367.3	365.9
Standard Deviation	23.5	6.6	11.6	13.1
%	6.4	1.7	3.2	3.6

The expected error in the found temperature is seen to be slightly better for the high-finesse/high-background system than for the low-finesse/low-background one, but both values are still double that for the optimum system. The difference between the 6.4% error expectation found here for the experimental apparatus and the 5% value for the same parameter in Section 3 points out the sensitivity of the fit to specific sets of noise, even when they have the same distribution.

Similar tests were performed on the area ratios for the optimum system, and the expected standard deviation dropped from 6.5% to 4.8%. Figure B.3 shows the three moment model predictions convoluted with the high finesse system for the same cases shown in Fig. 6.2.1. Comparison of these profiles with those obtained using the lower finesse system reveals that although the total width of the curves is significantly reduced, the ability to differentiate between models is not enhanced.

Improvements in finesse and optical speed which are attainable with currently available instruments reduce the expected standard deviations in temperature and asymmetry measurements by factors of 3 and 1.3 respectively. These lowered deviations are still comparable in magnitude to the differences between the models, so statistical analysis of the results would still be required.

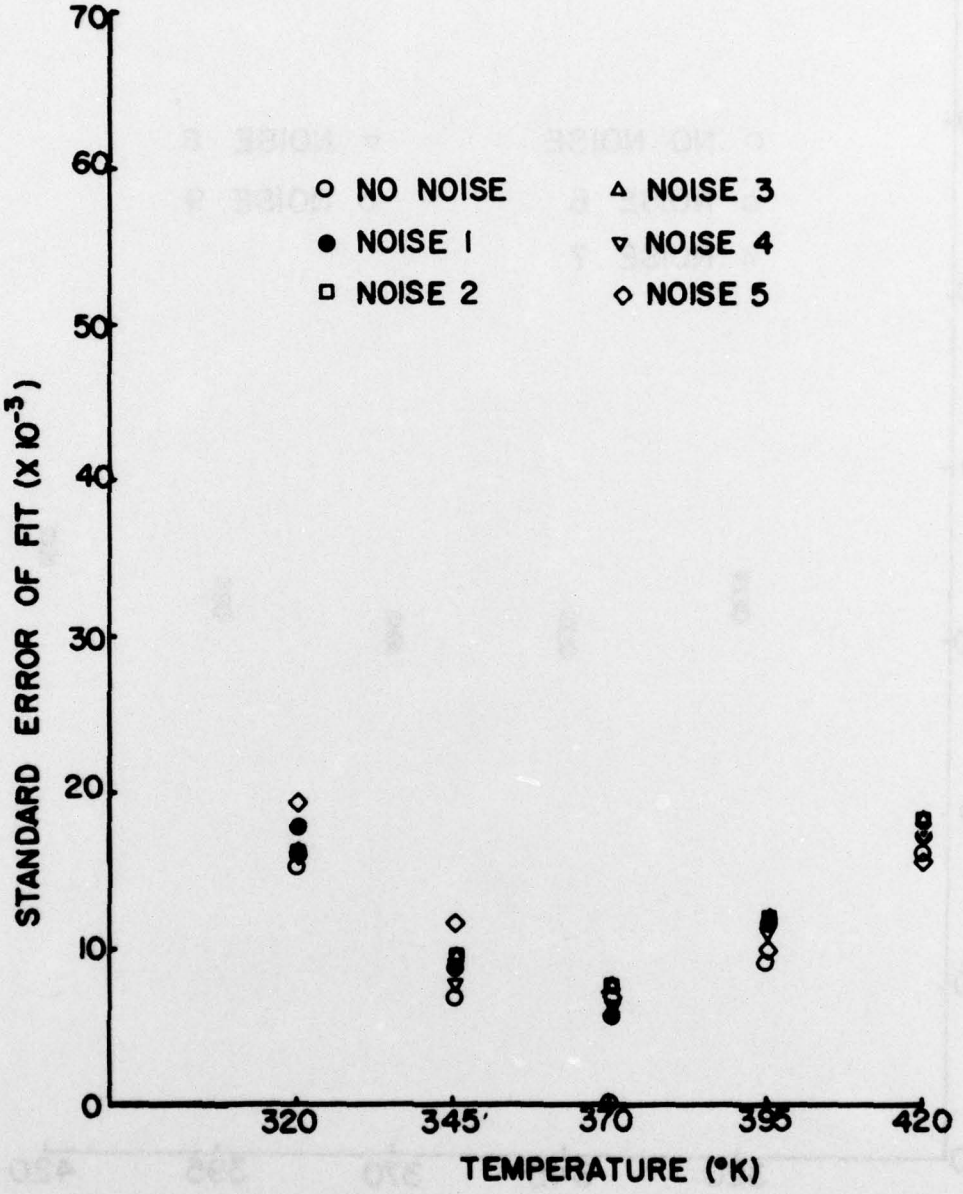


FIG. B.1(a). FIT OF A MAXWELLIAN TO A MAXWELLIAN

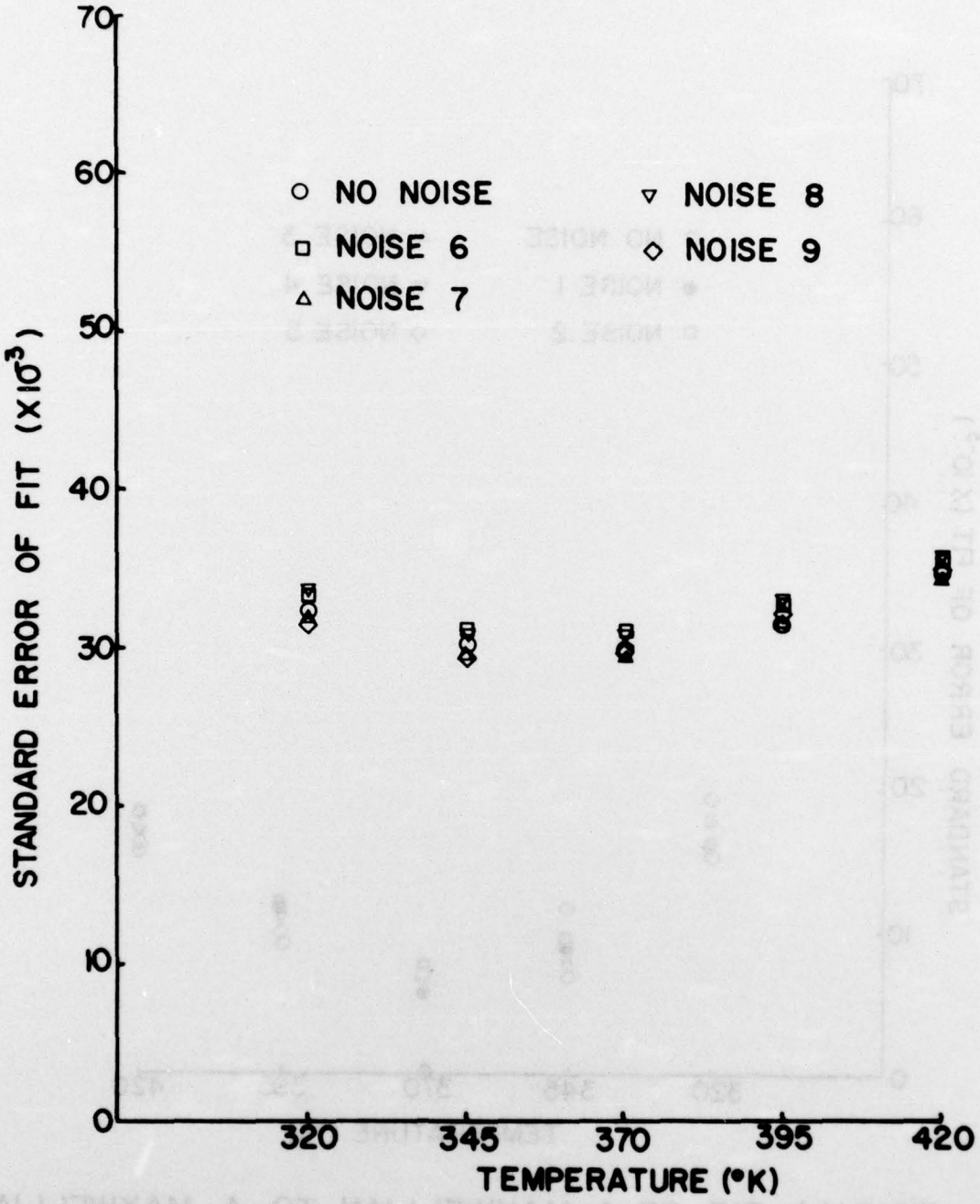


FIG. B.1(b). FIT OF A MAXWELLIAN TO A BIMODAL DISTRIBUTION, T_{RAT} =0.8

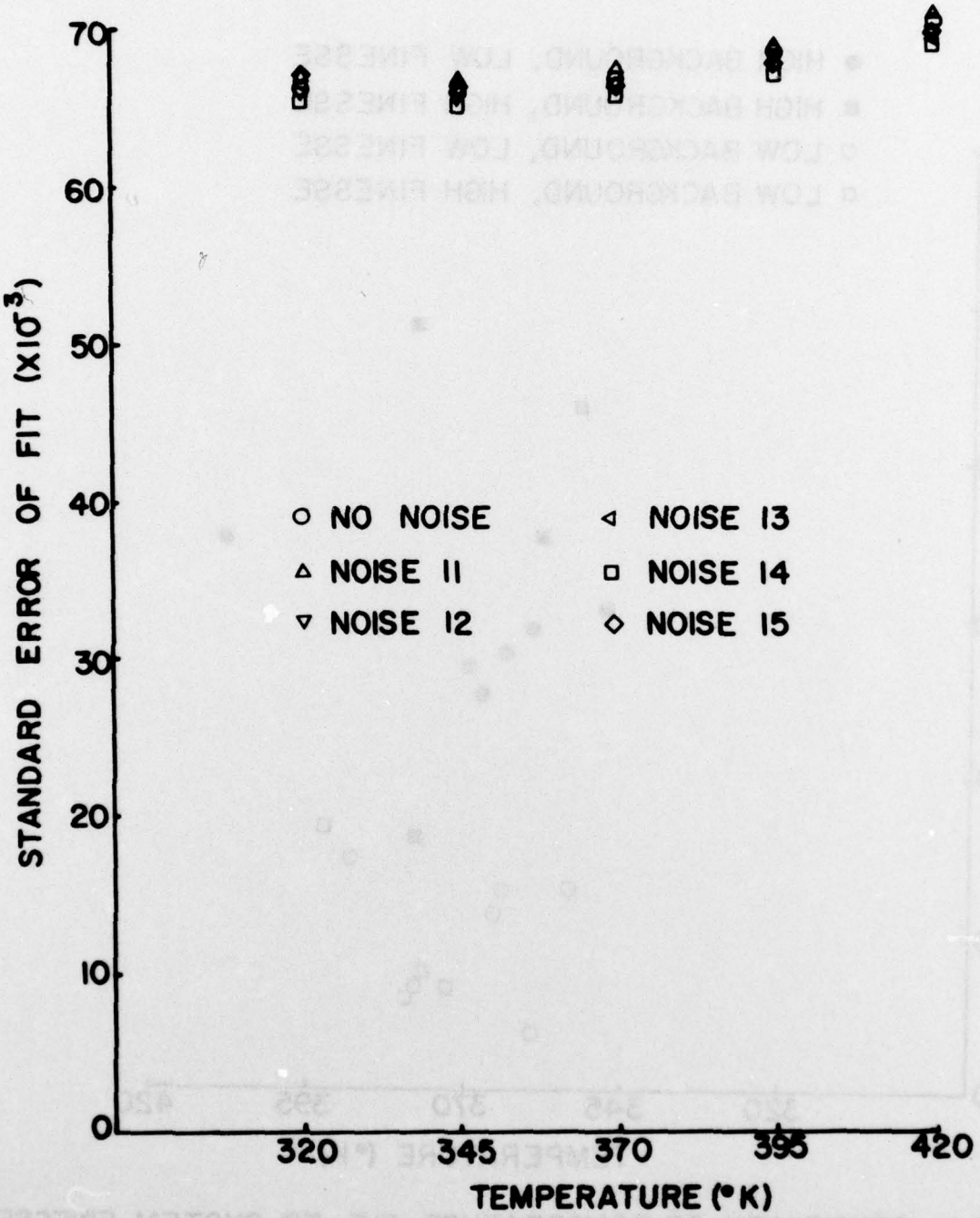


FIG. B.1 (c). FIT OF A MAXWELLIAN TO A BIMODAL DISTRIBUTION, T_{RAT} =0.6

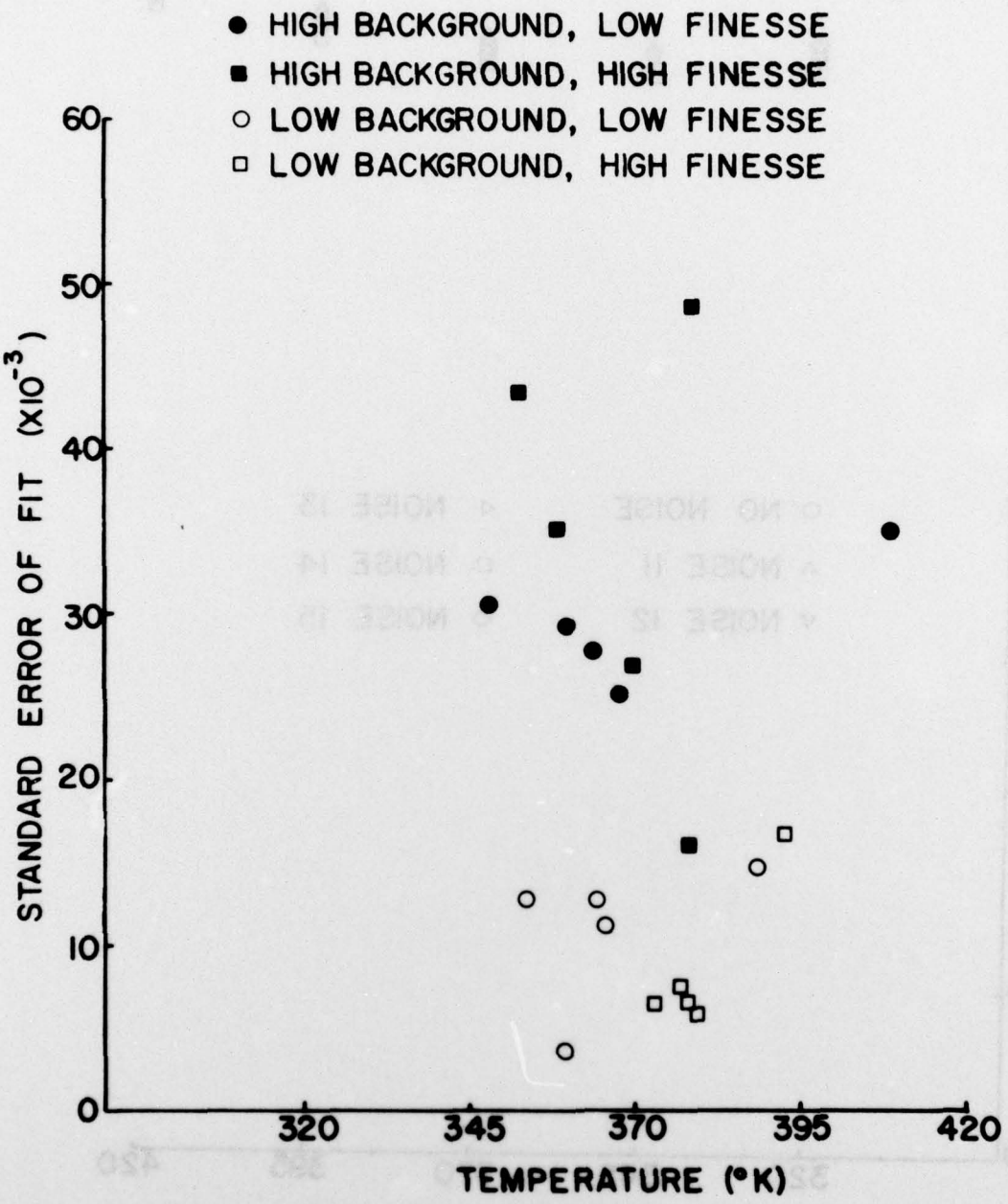


FIG. B.2. SENSITIVITY OF TEMPERATURE FIT TO SYSTEM FINESSE & BACKGROUND LIGHT LEVEL

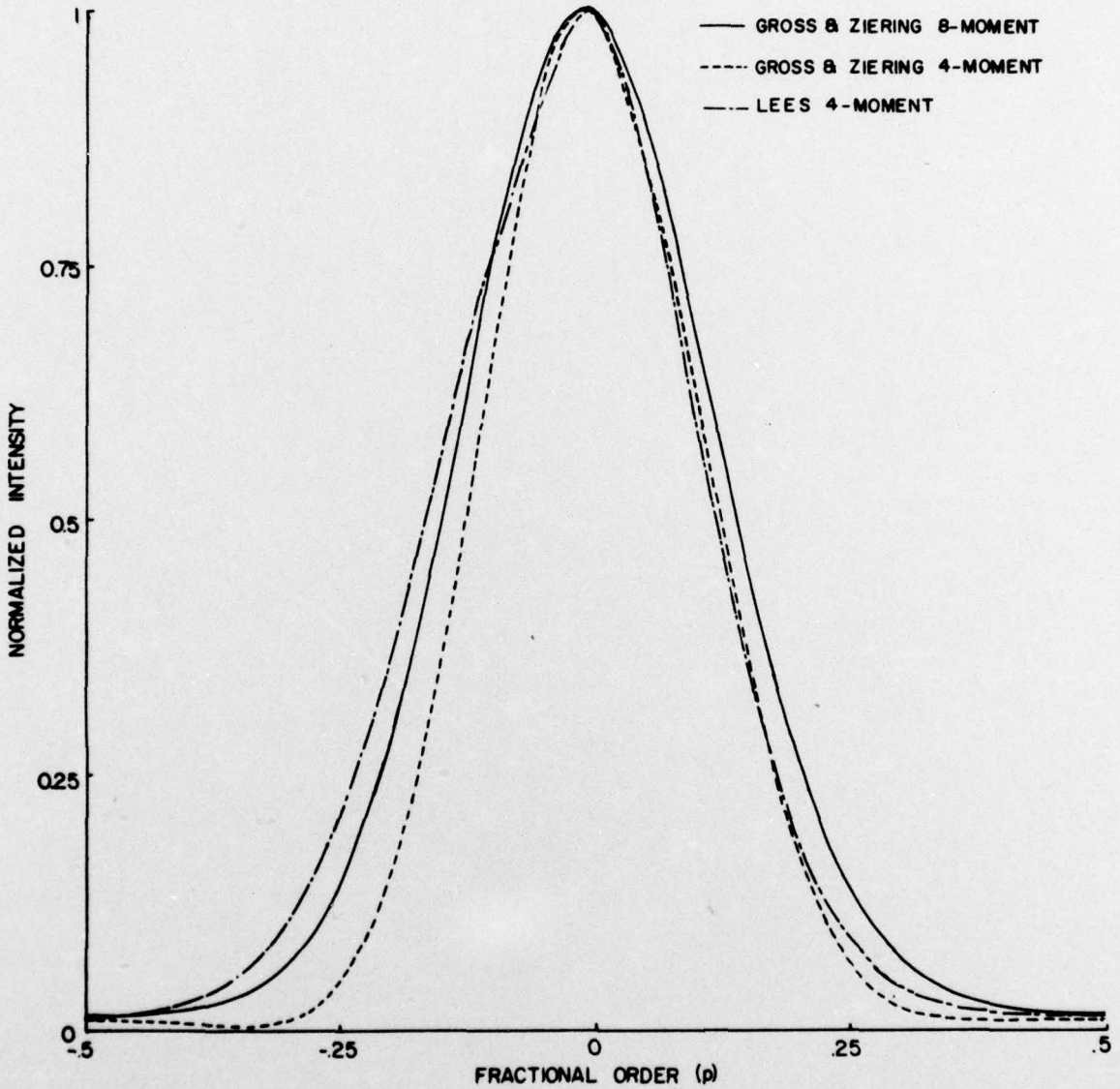


FIG. B.3(a). COMPARISON OF THEORETICAL PROFILES, "HIGH FINESSE" SYSTEM
Kn = 0.098, X/D = 0.75

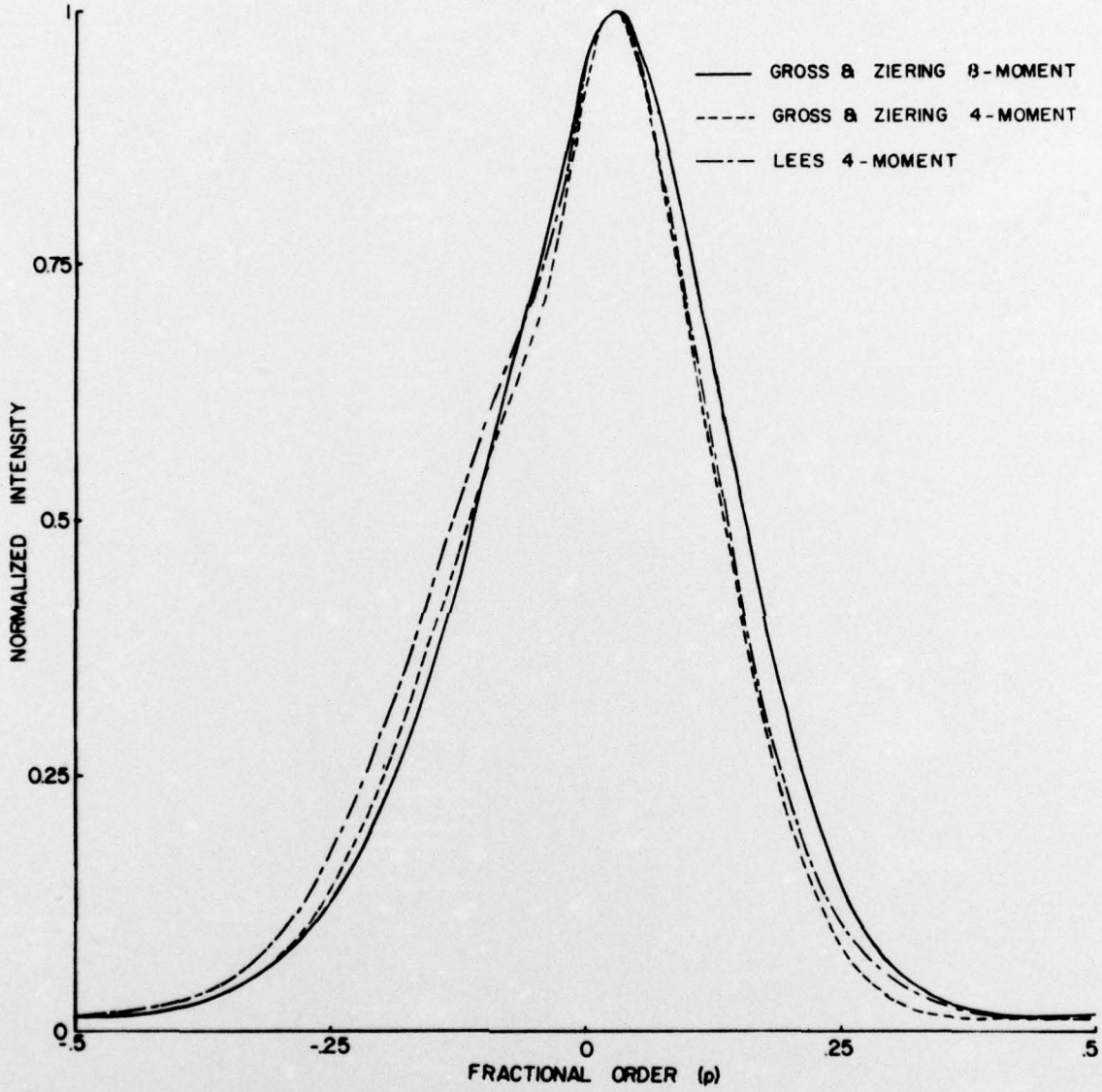


FIG. B.3(b). COMPARISON OF THEORETICAL PROFILES, "HIGH FINESSE" SYSTEM
Kn=0.83, X/D=0.7

APPENDIX C - EFFECT OF THE ELECTRON BEAM GENERATED PLASMA ON THE OBSERVED DISTRIBUTION FUNCTION

The spectral line used in this experiment was an ionic line, and since there was a finite time interval ($\sim 10^{-8}$ s) between the ionization and excitation of the atom and the subsequent photon emission, it is necessary to determine whether the electric field in the region of the electron beam was strong enough to accelerate the ions to appreciable velocities before they were observed, thus perturbing the distribution function.

The incremental velocity imparted to an argon ion in a uniform electric field is simply

$$\Delta \underline{v} = \underline{a}\Delta t$$

$$= \frac{e\underline{E}}{m_i} \Delta t \qquad (C.1)$$

Using $\Delta t^{-1} = 9.06 \times 10^7$ (s^{-1}) and $m_i = 6.6 \times 10^{-26}$ kg, one obtains $\Delta \underline{v} = 0.027\ \underline{E}$ m/s, where $\underline{E}$ is expressed in V/m.

If it is assumed that no plasma is created by the electron beam, the accelerating field is simply that due to a cylindrical conductor of radius R, where at any radius r within the conductor:

$$|E| = \frac{I}{2\pi r \epsilon_o v_e} \qquad (C.2)$$

Using $I = 5 \times 10^{-3}$ A, $R = .5 \times 10^{-3}$ m and $v_e = 4.59 \times 10^7$ m/s, one obtains $\underline{E}(R) = 3.9 \times 10^3$ V/m and $\underline{\bar{E}}(r)$, the average field within the beam, is 1.9×10^3 V/m. These correspond to incremental velocities for the ions of 105 and 53 m/s, respectively, significant portions of the thermal speed.

Fortunately, the electron beam generates a localized plasma as it traverses the gas, and it can be shown that the electron and ion number densities in the plasma are much greater than the primary beam electron number density. In our case, using published (Refs. 58,62) values of ionization rates for electron beams in argon we obtain $n_{e_{plasma}}/n_{e_{beam}} \approx 325$, so that the dominant electric fields are those required to balance the different rates at which the electrons and ions diffuse outwards from the plasma column.

The behaviour of a beam-generated plasma is difficult to analyze, but approximate solutions are available. One analysis which considers a beam between two parallel plates is that of Dunn and Self (Ref. 62). They assumed free-fall of the ions to the walls, a condition which is not exactly matched in our case because the ions are in transition flow, and hence undergo a few collisions between the beam and plates, but the basic forms of the beam-generated plasma are similar. The theory was based on the assumption that the electron beam was continuously creating electron-ion pairs which drained outward from the beam at the same rate that they were produced. Because the secondary electrons were more mobile than the ions, the potential within the beam would rise above the

wall potential as the ion number density increased above the electron density, and the equilibrium height of this potential rise would be the value at which the two charged species' currents became equal. It was postulated that the electron-ion pairs were created uniformly throughout the primary beam, and then Poisson's equation was solved in the form

$$\frac{d^2V}{dx^2} = \frac{en_{eo}}{\epsilon_o}\left[\int_o^x \frac{G(\xi)d\xi}{n_{eo}\sqrt{(2e/m_i)[V(\xi) - V(x)]}} - \exp\left(\frac{eV_e(x)}{kT_e}\right) - \frac{n_b}{n_{eo}}\right] \qquad (C.3)$$

where $G(\xi)$ is the rate of ion production per unit volume at a distance ξ from the beam centre,

$\sqrt{(2e/m_i)[V(\xi) - V(x)]}$ is the velocity at point x from the beam centre that an ion created at point ξ attains due to field acceleration,

n_{eo} is the on-axis ($x = \xi = 0$) secondary electron number density,

$n_{eo}\exp(eV_e(x)/kT_e)$ is the secondary electron number density at point x,

n_b is the primary beam electron number density.

The equation was solved by numerical integration for the potential profile V(x), and it was found that a nearly uniform plasma filling the space occupied by the beam was separated by a low potential sheath from a somewhat lower density plasma that extended to the walls, where a second higher potential sheath was formed. The electric fields within the beam itself were small, so that no significant acceleration of the ions would be expected, but within the sheath surrounding the beam, fields of O(10) V/cm could arise, resulting in incremental velocities near 50 m/s for the argon ions. Because the high field region of the sheath is only a small fraction of the total beam volume, only a small portion of the observed light comes from this region, and hence the effect on the observed distribution function would be negligible. This has been confirmed experimentally by Harnett (Ref. 34), who has measured Doppler profiles in argon at 9.5°K, a temperature at which the perturbation velocities would be of the same order as the thermal speed, and it was found that both the width and detailed shape of the line were correct.